MONITORING THE DIFFUSION AND DEGRADATION CHARACTERISTICS OF CRYSTALS VIA RAMAN SPECTROSCOPY

A Thesis Submitted to
the Graduate School of Engineering and Sciences of
İzmir Institute of Technology
in Partial Fulfillment of the Requirements for the Degree of

MASTER OF SCIENCE

in Physics

by
Barış AKBALI

July 2018
İZMİR

We approve the thesis of **Barış AKBALI**

Examining Committee Members:

Assoc. Prof. Dr. Hasan Şahin
Department of Photonics, İzmir Institute of Technology

Assoc. Prof. Dr. Sinan Balcı
Department of Photonics, İzmir Institute of Technology

Assoc. Prof. Dr. Engin DURGUN
Department of Materials Science and Nanotechnology, Bilkent University

02 July 2018

Assoc. Prof. Dr. Hasan ŞAHİN
Supervisor, Department of Photonics
İzmir Institute of Technology

Prof. Dr. R. Tuğrul SENGER
Head of the Department of
Physics

Prof. Dr. Aysun SOFUOĞLU
Dean of the Graduate School of
Engineering and Sciences

ACKNOWLEDGMENTS

First of all, I would like to thank my supervisor Assoc. Prof. Dr. Hasan Şahin for his patient instruction, generous help and support in my studies and this thesis work.

I would like to acknowledge and thank the committee members of my thesis Assoc. Prof. Dr. Sinan Balcı and Assoc. Prof. Dr. Engin Durgun for their participation.

I would also like to thank Prof. Dr. Volga Bulmuş, Prof. Dr. Mustafa M. Demir, Assoc. Prof. Dr. Cem Çelebi, Alper Yanılmaz, Gökhan Topçu, Tuğrul Güner, Aysel Tomak and Aytaç Gül for AFM, PL, XRD, UV-VIS absorption spectrum measurements and graphene growth/transfer procedure, and perovskite synthesis.

I would like to give my dearest thank my colleagues Elif Ünsal, Mehmet Özcan, Fadıl İyikanat, Ali Kandemir, Efsun Tekneci, Zeynep Kahraman, Berna Akgenç and my best friends Alper Yanılmaz, Dilce Özkendir, Ece Meriç for their unique friendship and special motivation at difficult times.

Most importantly, I would like to thank my family for everything they have done for me.

Finally, a special mention goes to my late advisor, Assoc. Prof. Dr. Yusuf Selamet who always believed in me. Without his support, I would never have been able to complete this study. To him I dedicated this thesis.

This research was supported by TUBITAK with 117F095 project number.

ABSTRACT

MONITORING THE DIFFUSION AND DEGRADATION CHARACTERISTICS OF CRYSTALS VIA RAMAN SPECTROSCOPY

Lamellar structures, having strong in-plane and weak (van der Waals) out-of-plane bonding, exhibit extraordinary properties when thinned down to their monolayer limit. Following the isolation of single layer graphene in 2004, there has been a rapid increase in the number of studies focusing on other novel two dimensional (2D) materials such as hexagonal Boron Nitride (BN), transition metal dichalcogenides (TMDs), post transition metal chalcogenides (PTMCs), silicene and black-phosphorus. Doping of 2D and bulk crystals is a well-known strategy that may lead to novel functionalities and significantly alters materials' electronic, optical, and magnetic properties. In this regard, understanding of diffusion characteristic of dopant in a crystal via computational simulation is vital to enlighten physical insights of the experiment. In addition, investigation of degradation mechanisms of crystals at atomic-level is also still open question. In this sense, the density functional theory (DFT) is one of the most powerful and commonly used methods for such theoretical investigations. Moreover, measuring vibrational spectra of a material via Raman spectroscopy is powerful method to understand atomic vibrations that give information about physical properties of a material. In this regards, we investigate diffusion characteristics and degradation mechanism of several crystal (such as, perovskites and MoS_2) by means of first-principles calculations based on density functional theory (DFT). In addition, Raman measurements are also carried out to investigate vibrational properties of the crystals. It is shown that few-layer MoS_2 can be used for selective nitrogenation of graphene. In addition, red shift in photoluminescence peak of water interacted $CsPbBr_3$ nanowires arise from detachment of surface ligand from surface of nanowire by presense of water molecules. Lastly, time-dependent photoluminescence measurement of Mn-doped $CsPbCl_3$ shows that change in emission color under UV illumination is due to segregation of Mn atoms towards crystal surface. This thesis provides some important results for deeper understanding of degradation and diffusion mechanisms of dopants in 2D materials and perovskites.

ÖZET

KRİSTAL YAPILARIN DİFÜZYON VE BOZULMA KARAKTERİSTİKLERİNİN RAMAN SPEKTROSKOPİSİ YOLU İLE GÖZLEMLENMESİ

Düzlem içi ve zayıf (van der Waals) düzlem dışı bir bağlanma yapısına sahip olan katmanlı yapılar, tek katmanlı sınırlarına kadar incelendiğinde olağanüstü özellikler sergiler. 2004 yılında tek tabakalı grafen izolasyonunu takiben altıgen Bor Nitrür (BN), geçiş metali dikalkojenler (GMD), geçiş sonrası metal kalkojen (PGMK) ve düzlem içi anizotropik tek tabakalı yapılar gibi diğer iki boyutlu (2D) malzemelere odaklanan çalışmaların sayısında hızlı bir artış oldu. İki boyutlu ve yığın kristalleri katkılama, 2D malzemelerin uygulanabilir hale getirmeye yarayan bilinen bir stratejidir ve bu malzemelerin elektronik, optik ve manyetik özelliklerini önemli ölçüde değiştirebilir. Bu bağlamda, bir kristalde hesaplamalı simülasyon ve deneysel ölçüm yoluyla dopantın difüzyon karakteristiğinin anlaşılması, deneyin fiziksel içyüzünü aydınlatmak için önem taşımaktadır. Ayrıca, atomik seviyedeki kristallerin bozunma mekanizmalarının incelenmesi hala açık bir sorudur. Bu anlamda, yoğunluk fonksiyonel teorisi (DFT), bu tür kuramsal araştırmalar için en güçlü ve yaygın olarak kullanılan yöntemlerden biridir. Buna ek olarak, bir malzemenin titreşim spektrumlarını Raman spektroskopisi ile ölçmek, bir malzemenin fiziksel özellikleri hakkında bilgi veren atomik titreşimleri anlamak için güçlü bir yöntemdir. Bu bağlamda, auxetik tek katmanlı pentagonal yapılar, esnek tek katmanlı delikli grafen kristalleri, ultra-esnek tek katmanlı PGMK lar, ve düzlem içi anisotropik çeşitli kristallerin difüzyon karakteristiği ve bozunma mekanizmasını (perovskites ve MoS_2 gibi) ilk prensiplere dayanan yoğunluk fonksiyoneli teorisi tabanlı hesaplamalar yoluyla araştırıyoruz. Raman ölçümleri de kristallerin titreşim özelliklerini araştırmak için gerçekleştiriliyor. Grafenin seçici nitrojenlenmesi için birkaç katman MoS_2'nin kullanılabileceği gösterilmiştir. Buna ek olarak, suyun fotolüminesans pikindeki kırmızıya kayma $CsPbBr_3$ nanotelleri, su moleküllerinin varlığıyla nanotel yüzeyinden yüzey ligandının ayrılmasından kaynaklanır. Son olarak, Mn-katkılı $CsPbCl_3$'nın zamana bağlı fotolüminesans ölçümü, UV aydınlatması altında emisyon rengindeki değişikliğin Mn atomlarının kristal yüzeyine doğru ayrılmasından kaynaklandığını göstermektedir. Bu tez çalışmasında elde edilen sonuçlar perovskite ve iki boyutlu malzemelerin bozunma ve difüzyon karakteristiklerinin derinlemesine anlaşılmasına olanak sağlayacak önemli temel bilgileri sağlamaktadır.

... to my family and Assoc. Prof. Dr. Yusuf SELAMET ...

TABLE OF CONTENTS

LIST OF FIGURES

CHAPTER 1

INTRODUCTION

The phenomenon of inelastic scattering of light by matter was first introduced experimentally by Chandrasekhara Venkata Raman, an Indian physics professor,and his collaborator K.S. Krishnan in 1928.(Rybin *et al.*, 2016) Raman spectroscopy is an effective characterization technique based on the analysis of the inelastically scattered photons from the material medium. Raman spectroscopy has been widely used in experiments to investigate fundamental physical properties of crystals or molecules due to requiring minimum sample preparation and providing non-destructive analysis.(Hendra and Stratton, 1969; Ferrari *et al.*, 2006; Li *et al.*, 2012; Kneipp *et al.*, 1997)

Lamellar structures, having strong in-plane and weak (van der Waals) out-of-plane bonding, exhibit extraordinary properties when thinned down to their monolayer limit. Showing different properties than bulk form is the consequence of quantum effects and strong electron confinement in out-of-plane direction. Realization of graphene is the pioneer of family of two-dimensional (2D) materials. Since its successful synthesis,(Novoselov *et al.*, 2005) graphene has become the most intensively studied form among the various carbon allotropes. Due to the strong sp^2 hybridization of carbon atoms and its single-atom thickness, graphene has extraordinary properties such as advanced mechanical strength,(Ovid'Ko, 2013) high carrier mobility (Neto *et al.*, 2009) and heat conduction (Balandin *et al.*, 2008) properties. Lin *et al.* successfully fabricated 2-inch wafer-scale graphene field effect transistor (FET) with a cutoff frequency in the radio frequency range, as high as 100 GHz.(Lin *et al.*, 2010) In addition, ultrahigh electron mobility (200000 $cm^2V^{-1}s^{-1}$) achieved in suspended graphene.(Bolotin *et al.*, 2008) These properties make graphene as a rising star in the wide range of applications in nanodevices.(Vicarelli *et al.*, 2012)

Following the graphene, layered transition-metal dichalcogenides (TMDs) are introduced by early transition metals and chalcogenides with stoichiometry formula MX_2 (M=Ti, Zr, Hf, V, Nb, Ta, Mo, W, Re; X=S, Se, Te). They have crystal structure in the form of X-M-X where transition metal atom (M) is sandwiched between two monolayers of chalcogen (X). The interest in 2D TMDs such as MoS_2 has grown rapidly due to their superior properties such as unique quantum luminescence efficiency (Mak *et al.*, 2010), high channel mobility($\sim$ 200 cm^2 V^{-1} s^{-1}) (Radisavljevic *et al.*, 2011) and large current

ON/OFF (60 mV dec^{-1}) (Yoon *et al.*, 2011; Kong *et al.*, 2013; Zhang *et al.*, 2014; Fang *et al.*, 2012; Ali *et al.*, 2014; Keum *et al.*, 2015; Ramakrishna Matte *et al.*, 2010; Georgiou *et al.*, 2013; Splendiani *et al.*, 2010). In addition, it was shown that MoS_2 exhibits excellent hydrogen evolution reaction (HER) catalyst.(Lukowski *et al.*, 2013; Li *et al.*, 2011) Lee *et al.* reported that thickness of the MoS_2 can be determined by examining frequency difference between the two prominent Raman active vibrational modes', E^1_{2g} and A_{1g}.(Lee *et al.*, 2010) Furthermore, MoS_2 exhibits indirect to direct gap transition when it is thinned down from bulk to monolayer.(Wang *et al.*, 2012) Due to its exceptional electronic and optical properties, MoS_2 has been promising materials for nanoscale electronic device applications.

It was reported that different source/drain contacts determine the intrinsic transport properties of few-layer MoS_2 flakes.(Das *et al.*, 2012) Among exfoliation techniques, (Eda *et al.*, 2011; Xiao *et al.*, 2010) liquid exfoliation is one of the promising method to obtain single-layer MoS_2.(Coleman *et al.*, 2011; Lee *et al.*, 2011) Both its broad production methods and unique physical and chemical properties (Mak *et al.*, 2010) make MoS_2 a promising material for various applications in electronics,(Wu *et al.*, 2014; Li *et al.*, 2012) catalysis,(Miremadi and Morrison, 1987) chemical sensors,(Zhang *et al.*, 2004) lubrication,(Rapoport *et al.*, 1997) as well as protective layer to corrosion.(Vandana *et al.*, 2016) Bulk MoS_2 as a coating material has been investigated both theoretically and experimentally for decades because of its stable friction coefficient. (Donnet *et al.*, 1996; Martin *et al.*, 1993; Wahl *et al.*, 1998) The anti-wear properties of MoS_2 have been examined theoretically (Sen *et al.*, 2014) and experimentally (Park *et al.*, 2013) as an oxidation protective nanocoating material as well. In addition to MoS_2, other 2D materials such as WS_2,(Sen *et al.*, 2014) graphene,(Raman *et al.*, 2012; Topsakal *et al.*, 2012; Schriver *et al.*, 2013; Kirkland *et al.*, 2012; Chen *et al.*, 2011) and *h*-BN (Vandana *et al.*, 2016; Liu *et al.*, 2013; Li *et al.*, 2014; Shen *et al.*, 2016; Li *et al.*, 2014) have been widely investigated both theoretically and experimentally as a protective layer against corrosion.

Incorporation of nitrogen (N) atoms into the crystal structure by N_2 plasma treatment is a practical method for modifying the physical and chemical properties of materials.(Talbi *et al.*, 2006; Patel *et al.*, 2009) Regarding the graphene having semimetallic electronic structure, N is considered to be an excellent dopant which is able to form strong covalent bonds by donating extra electrons into the graphene lattice.(Akada *et al.*, 2014; Rybin *et al.*, 2016) It has been reported that incorporation of N in graphene may provide n- or p-type doping depending on the bonding character of the N atom.(Lu *et al.*, 2013; Wu *et al.*, 2012) Such nitrogenated graphene has been used in different applications such

as lithium batteries, (Reddy *et al.*, 2010; Wang *et al.*, 2011) bio-applications,(Wang *et al.*, 2010) field effect transistors, (Zhang *et al.*, 2011) supercapacitors (Jeong *et al.*, 2011) and oxygen reduction reaction in fuel cells.(Bao *et al.*, 2014; Wang *et al.*, 2012; Park *et al.*, 2014; Qu *et al.*, 2010; Jafri *et al.*, 2010) Similarly, nitrogenation can also alter the electrical properties and chemical activity of MoS_2 crystal.(Qin *et al.*, 2014; Liu *et al.*, 2016) McDonnell *et al.* showed that MoS_2 can exhibit both p- and n-type at different positions on the same sample, which is attributed to variations in the local stoichiometry of MoS_2 due to surface defects.(McDonnell *et al.*, 2014) In addition, Su *et al.* showed that the increment of the number of N atoms causes an increase in the electron concentration, therefore the Fermi level can be shifted toward the conduction band minimum.(Su and Lin, 2016)

Halide perovskites, having the structure of ABX_3 (where A is organic: $CH_3NH_3^+$ (MA), $HC(NH_2)_2^+$ (FA) or inorganic: Cs^+ cation, B is metal cation: Pb^{2+}, Sb^{2+}, Sn^{2+}, and X is halide anion: Cl^-, I^-, Br^-), have been known since 1950s.(MØLLER, 1958) With the discovery of $MAPbI_3$ as photosensitizer in dye-sensitized solar cells (DSSCs) at 2009s,(Kojima *et al.*, 2009) these materials have started to receive more attention.(Stoumpos and Kanatzidis, 2015) Since then, in a short period of time, perovskite solar cells have become able to improve the conversion efficiency from 3.81% to almost 20%.(Jeon *et al.*, 2015; Kojima *et al.*, 2009; Liu and Kelly, 2014; Zhou *et al.*, 2014) Apart from the success of these materials in photovoltaic applications,(Im *et al.*, 2011) it has been demonstrated recently that these materials can be applied also to light-emitting diodes (LEDs),(Byun *et al.*, 2016; Cho *et al.*, 2015; Li *et al.*, 2017) lasers,(Yakunin *et al.*, 2015; Zhu *et al.*, 2015) photodetectors,(Ramasamy *et al.*, 2016) etc. due to their unique optical properties; high quantum yield (90%), wavelength tunability, and color purity.(Kovalenko *et al.*, 2017; Protesescu *et al.*, 2015; Stoumpos and Kanatzidis, 2016; Bai *et al.*, 2016; Li *et al.*, 2017)

Even though all-inorganic perovskites are better in terms of intrinsic stability than the organometallic halide ones, stability is still a challenge especially against moisture and polar solvents such as water, ethanol, acetone, etc.(Kovalenko *et al.*, 2017; Iso and Isobe, 2018; Huang *et al.*, 2017; Li *et al.*, 2017) Such high chemical instability mainly stems from high ionic character of the compounds. However, practical applications require deeper understanding of degradation mechanisms for synthesis of highly stable halide perovskites under ambient conditions. To date, various approaches have been developed such as mixing with mesoporous silica,(Wang *et al.*, 2016) core-shell structure,(Qiao *et al.*, 2017; Li *et al.*, 2018; Bhaumik *et al.*, 2016) different surface treatments (other than usual

ones; Oleic acid (OA), and Oleylamine (OAm)) (Luo *et al.*, 2016; Huang *et al.*, 2016) or encapsulation with polymers(Wei *et al.*, 2017; Raja *et al.*, 2016; Wang *et al.*, 2016) to obtain perovskite nanocrystals with high stability.

Recently, among halide perovskites, all-inorganic $CsPbX_3$ nanocrystals have started to draw much attention because of their high photoluminescence quantum yields and controllable morphologies.(Xue *et al.*, 2017; Swarnkar *et al.*, 2015; Zhang *et al.*, 2016; Sun *et al.*, 2016) Chen *et al.* reported efficient synthesis technique to prepare $CsPbX_3$ nanocrystals with tunable composition, luminescence characteristics, and morphologies. (Chen *et al.*, 2017)

Degradation mechanisms at atomic-level and possible stabilization techniques are still open questions in the growing field of perovskite nanocrystals. A very recent study of Yuan *et al.* reported that both light and humidity may degrade $CsPbI_3$ quantum dots.(Yuan *et al.*, 2018) Recent perspective study on lead halide perovskite solar cells (PSCs) enlightens the defect tolerance and stability of the material.(Huang *et al.*, 2017) Lejitas and co-workers reviewed strategies to overcome the issues of structural, thermal, and atmospheric degradation of $CsPbX_3$ nanocrystals.(Leijtens *et al.*, 2017) In addition to experimental studies, tremendous efforts have been also performed on PSCs by carrying out density functional theory (DFT) calculations.(Iyikanat *et al.*, 2017; Yin *et al.*, 2015; Geng *et al.*, 2014; Kawai *et al.*, 2015; Haruyama *et al.*, 2015) Kang *et al.* theoretically predicted that regarding its electronic properties $CsPbBr_3$ is a defect-tolerant semiconductor.(Kang and Wang, 2017) In addition, theoretical studies on defects in perovskites have been widely studied.(Haruyama *et al.*, 2017; Azpiroz *et al.*, 2015; Kim *et al.*, 2014; Yin *et al.*, 2014) Although the organic-inorganic hybrid lead halide perovskites have been studied theoretically and experimentally, the pure inorganic alternative, $CsPbBr_3$ phase, has been recently found to possess most of the good properties of the hybrid lead halide counterpart.(Bekenstein *et al.*, 2015; Protesescu *et al.*, 2015)

As a member of colloidal semiconductor nanocrystal (NC) family, cesium lead halide perovskites in the form of $CsPbX_3$ (X: Cl^-, Br^-, I^-) offer outstanding optical properties such as high photoluminescence quantum yield (PLQY) and defect-tolerance, and wavelength tunability.(Zhang *et al.*, 2015; Protesescu *et al.*, 2015; Akkerman *et al.*, 2015; Huang *et al.*, 2017; Kang and Wang, 2017; Li *et al.*, 2017; Swarnkar *et al.*, 2015) Moreover, these materials are solution-processable, and therefore, morphology of perovskite NCs can be easily controlled(Pan *et al.*, 2016) (i.e. nanocubes,(Protesescu *et al.*, 2015; Lignos *et al.*, 2016) nanowire,(Zhang *et al.*, 2015; Imran *et al.*, 2016; Amgar *et al.*, 2017) nanoplatelets (Akkerman *et al.*, 2016; Shamsi *et al.*, 2016; Lv *et al.*, 2016)) or composi-

tion of NCs can be tailored.(Protesescu *et al.*, 2015; Akkerman *et al.*, 2015; Huang *et al.*, 2017; Li *et al.*, 2017) In this sense, either by adjusting the NCs size through morphology control or via anion-exchange reactions by adjusting the composition,(Akkerman *et al.*, 2015; Nedelcu *et al.*, 2015) one can cover the full visible spectrum or can tune their optical properties.(Brennan *et al.*, 2017; Bekenstein *et al.*, 2015; Li *et al.*, 2017; Kovalenko *et al.*, 2017; He *et al.*, 2017) Cesium lead perovskites are potential candidates in a variety of optoelectronic and photonic applications such as solar cells,(Kulbak *et al.*, 2015; Beal *et al.*, 2016) photodetectors,(Ramasamy *et al.*, 2016; Song *et al.*, 2016) display,(Wang *et al.*, 2016; Güner *et al.*, 2018) light-emitting diodes,(Song *et al.*, 2015; Li *et al.*, 2016, 2017) and lasers.(Eaton *et al.*, 2016; Xu *et al.*, 2016; Yakunin *et al.*, 2015)

Doping is a well-known strategy that may lead to novel functionalities and significant improvement in device efficiency.(Meinardi *et al.*, 2017; Norris *et al.*, 2001; Pradhan and Sarma, 2011; Pradhan *et al.*, 2005; Rice *et al.*, 2016; Fainblat *et al.*, 2016; Santra and Kamat, 2012; Erickson *et al.*, 2014; Erwin *et al.*, 2005; Bryan and Gamelin, 2005; Norris *et al.*, 2008; Pradhan *et al.*, 2017). To date, various ions that are used as dopant for cesium halide perovskite NCs have been reported.(Pan *et al.*, 2017; Liu *et al.*, 2017; Zhou *et al.*, 2017; Hu *et al.*, 2018; Guria *et al.*, 2017; Van der Stam *et al.*, 2017) Among those, doping of cesium lead perovskites with Mn ions started to attract a significant attention recently since the presence of Mn ions can add novel optical and magnetic features to NCs.(Guria *et al.*, 2017; Nag *et al.*, 2008; Mir *et al.*, 2017; Wang *et al.*, 2017; Lin *et al.*, 2017) For instance, Mn ions open an extra emission channel at $\approx$ 590nm due to transfer of exciton energy from host to *d*-states of Mn.(Liu *et al.*, 2016; Rossi *et al.*, 2017; Parobek *et al.*, 2016) In other words, dopant-induced emission is the result of radiative transition of electrons between host and the intra-gap states of dopant impurities.(Norris *et al.*, 2008) During this transition, energy is transferred from electron-hole pair created via excessive energy of absorbed photon to the dopant levels, and as a result, dopant-induced emission occurs due to the electron-hole recombination taking place in the midgap states of dopant impurities.(Pradhan *et al.*, 2017; Pradhan and Sarma, 2011) However, doping may create charge and size imbalance at the host lattice of these NCs that causes change in both the crystal structure, and the emission characteristics.(Norris *et al.*, 2008; Karan *et al.*, 2011; Acharya *et al.*, 2013; Kamat, 2011)

In this thesis, diffusion and degradation characteristics of perovskites and MoS_2 are investigated with Raman spectroscopy and DFT calculations. Although, graphene as a corrosion protection barrier has been studied,(Prasai *et al.*, 2012) MoS_2 as a nitrogen protection barrier on graphene is still missing. In this regard, lateral and vertical diffusion

characteristics of N atom on MoS_2 are examined. It is shown that few-layer MoS_2 can be used for selective nitrogenation of graphene. In addition, red shift in photoluminescence peak of water interacted $CsPbBr_3$ nanowires arise from detachment of surface ligand from surface of nanowire by presense of water molecules. Lastly, time-dependent photoluminescence measurement of Mn-doped $CsPbCl_3$ shows that change in emission color under UV illumination is due to segregation of Mn atoms towards crystal surface. Moreover, we also investigate vertical diffusion of Mn atom in perovskite crystal. In addition to diffusion characteristics of crystal, degradation of perovskite material is also studied.

CHAPTER 2

METHODOLOGY

2.1. Experimental Techniques

2.1.1. Raman Spectroscopy

Optical characterization techniques utilize the measurement of light coming from a material medium. Optical characterizations can be classified into two main parts, namely; emission spectroscopies and absorption spectroscopies. In the case of absorption spectroscopy, any absorbed photon, broad band of light beam coming from a source, contributes to a reduction in the intensity of the traveling beam at the corresponding frequency. In the case of emission spectroscopy, photon absorbed by the entities (atoms, molecules, etc) and jump to the excited state in energy space. Then atoms or molecules go back to its ground state and emits photon. Raman and luminescence spectroscopies are counted among emission spectroscopy techniques.

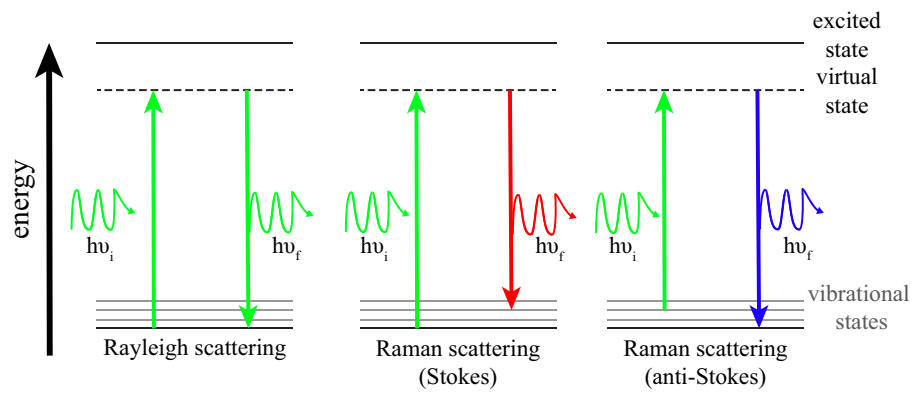

Figure 2.1. Quantum energy transitions for Rayleigh and Raman scattering.

Raman measurement is a technique based on the analysis of the photons that inelastically scattered, from a materials medium, produced by interaction of the light with

crystal vibrations. During Raman spectroscopy measurements, usually the shift in energy between the incoming and inelastically scattered light is displayed.

2.1.1.1. Theory of Raman

When a beam of light interacts with material medium, different processes may occur depending on the thickness and density of the medium atoms. If the material is thick and dense enough, the incident light interact with the medium atoms. The interacted photons are scattered in a direction different or the same as the incident beam. The scattering of light phenomenas may be considered into two main types namely; elastic and inelastic scatterings.

Inelastic and Elastic Scatterings : During a scattering process, usually a photon is absorbed by a medium entity (atom, molecules, etc.) which is then excited to higher energy level. Such excited entitle will lose its energy by either emitting a photon or by some other thermal relaxation mechanism such as collision etc. In the case of photon emission, most probably emitted photon will have the same energy as the incident photon. This process is called *elastic scattering*. Elastic scattering is also called as 'Rayleigh scattering'. If the emitted photons have higher or lower energy than that of incident photons, the scattering is called *inelastic scattering*.

Raman scattering, is first observed in 1928 by C.V. Raman,(Raman, 1928) is based on the inelastic scattering. Inelastic scattering process is also divided into two in themselves. If inelastically scattered photon has higher (lower) energy than that of incident one, the scattering is called Stokes (anti-Stokes) scattering. Therefore, Stokes (anti-Stokes) scattered photons appear at lower (higher) energy levels than that of the incident light energy (Rayleigh line) by the amount of energy equal to the energy difference between the initial and final energy states of the scattering medium entity. At room temperature, Stokes scattered lines have higher intensity than that of anti-Stokes lines. Since, most of the scattering medium atoms are in their ground states and anti-Stokes lines require medium atoms being already in excited states. Therefore, during Raman measurement, usually, Stokes shifted Raman lines are preferred to display. Thus, when the temperature increases, intensity of Stokes (anti-Stokes) lines decrease (increase).

The Raman scattering can be understood by employing classical scattering theory. In the classical point of view, the incident light coming to the material medium induces polarization. The polarized entity will have the own resonant frequency usually different

from the incident photon frequency. Electric field **E** of an incident light can be given as

$$E = \mathbf{E_0} cos(2\pi\nu_0) \tag{2.1}$$

where $\mathbf{E}_0$ is the complex amplitude and ν_0 is the frequency. The polarization induced is defined by

$$\mathbf{P} = \alpha\mathbf{E} \tag{2.2}$$

where α is the polarizability of the material. Any material above absolute zero will have thermally excited atomic vibrations causing the polarizability to fluctuate. Thus, α can be explanded into a Taylor series dependent on the plane wave Q, whic are the normal modes of the atomic vibrations permitted in a crystalline semiconductor. Expanded form of α can be written as

$$\alpha = \alpha_0 + (\frac{\partial\alpha}{\partial Q})_0\mathbf{Q} + ... \tag{2.3}$$

where the subscript 0 denotes the values and derivatives at the equilibrium position of the system. **Q** takes the known form of a plane wave and is defined as

$$\mathbf{Q} = Q_0 + cos(2\pi\nu_{vib}t) \tag{2.4}$$

where ν_{vib} is the frequency of the normal mode vibration in the semiconductor. Substituting Eqs. (2.1.1.2), (2.3), and (2.4) into into Eq. (2.2), gives a result of the form

$$\mathbf{P} = \mathbf{P_0} + \mathbf{P_{ind}} \tag{2.5}$$

where $\mathbf{P}_0$ is equal to

$$\mathbf{P} = \alpha_\mathbf{0}\mathbf{E_0}\mathbf{cos}(\mathbf{2}\pi\nu_\mathbf{i}\mathbf{t}) \tag{2.6}$$

and is a polarizing vibration with the same frequency and phase as the incident radiation. The second term, $\mathbf{P}_{ind}$ is defined by

$$\mathbf{P_{ind}} = \frac{\mathbf{E_0}}{\mathbf{2}}(\frac{\partial\alpha}{\partial\mathbf{Q}})_\mathbf{0}\mathbf{Q}\{\mathbf{cos}[\mathbf{2}\pi(\nu_\mathbf{i} + \nu_\mathbf{vib})\mathbf{t}] + \mathbf{cos}[\mathbf{2}\pi(\nu_\mathbf{i} - \nu_\mathbf{vib})\mathbf{t}]\} \tag{2.7}$$

As can be seen in Eq. (2.7), the polarization contains two sinusoidal waves with slightly shifted frequencies from the incident wave dependent on the allowed vibrations in the crystal structure. The term containing a decrease in frequency (ν_i-ν_{vib}) is considered Stokes lines, and the term containing an increase in frequency (ν_i+ν_{vib}) is considered

anti-Stokes lines. Eq. (2.5) explains both the polarization of the material and subsequent Rayleigh and Raman scattering of light from the entity. In addition first order Raman scattering, higher terms of the Taylor series of the polarization vector give rise to corresponding higher order Raman scattering lines.

The intensity (I) of the Raman scattered light is given as proportional to the exciting light power on the power of the laser used to excite (l), the square of the polarizability of the electrons in molecule (n), and the fourth power of the frequency of the incident radiation (ω);

$$I = Kln^2\omega^4 \tag{2.8}$$

where l is the incident light power, ω is the (angular) frequency and K is a constant.(Smith and Dent, 2013)

2.1.1.2. Our Setup

In Raman spectroscopy, all scattered photons are collected but usually, Rayleigh scattered photons are filtered with appropriate band-pass or band-edge filters. Another technique to filter Rayleigh scattering is that one can use appropriate scattering angle of a grating spectrometer to avoid the Rayleigh line being detected by a proper detector. Raman side bands, seen as shifted lines from the Rayleigh line, thus can easily be detected by an appropriate detector after going through a spectral separation as in a grating spectrometer or it can be obtained from the Fourier Transformed Interferogram in the case of interferometric spectrographs. Then, the spectrum is recorded as the intensity of scattered light as a function of photon energy or frequency. Usually, one only need the spectrum recorded at the relative frequencies with respect to Rayleigh line which corresponds to the internal excitations of a scattering medium. This is obtained by simply subtracting the observed spectrum frequencies from the Rayleigh frequency. Thus, usual Raman spectra are recorded as 'Raman shifts'.

In this thesis, Raman measurements were carried out by using Horiba Xplora Plus Raman system. The system includes Synergicity grating spectrometer with a selectable choice of a set of four gratings of 600 grooves(gr)/mm, 1200 gr/mm, 1800 gr/mm, and 2400 gr/mm which are holographic, sensitive from the near IR to near UV region. 532 nm and 785 nm lasers are used for sample excitation. A motorized rotating mirror on the pathway of the lasers selects one of them. Light coming from a laser is first filtered

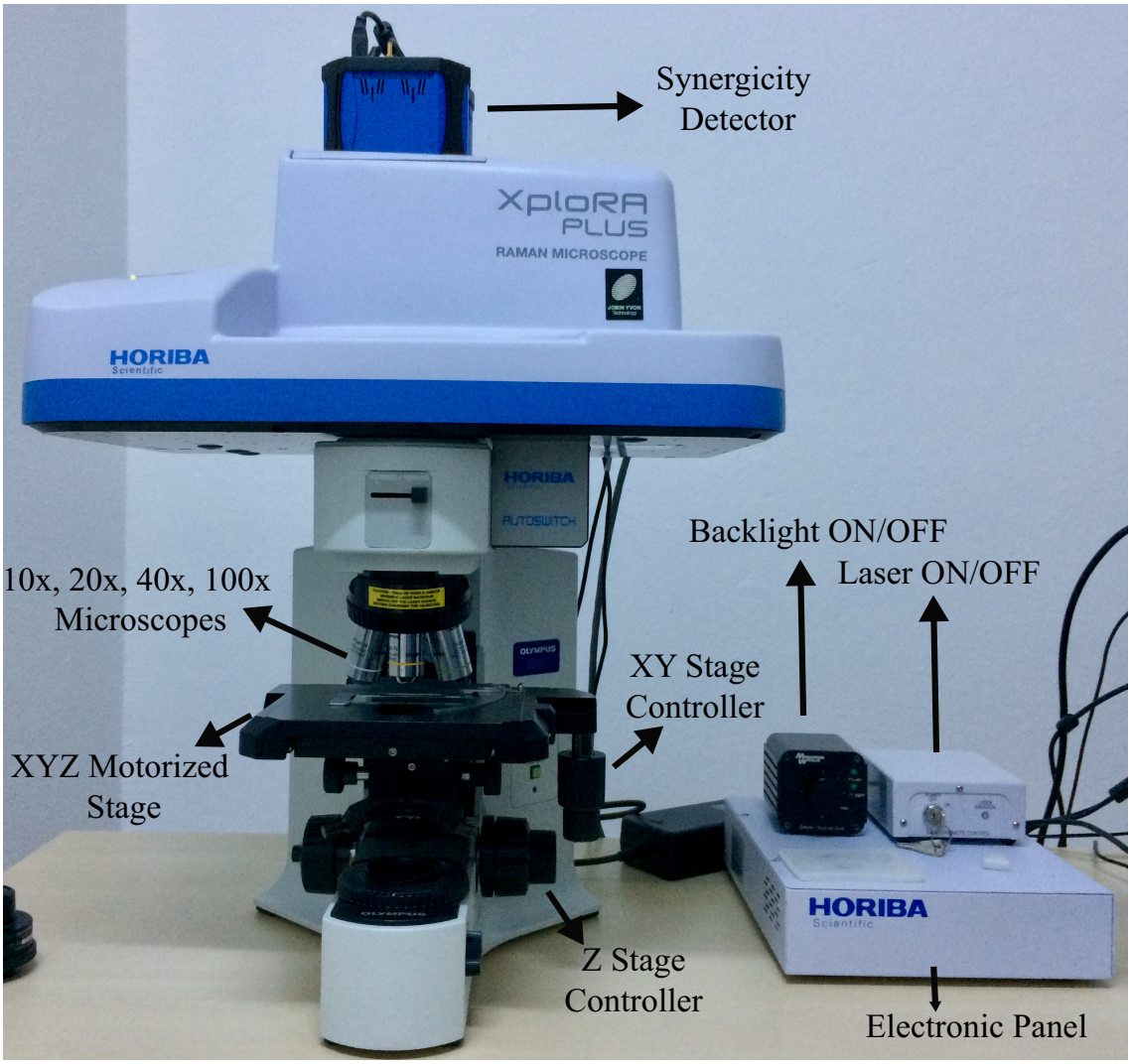

Figure 2.2. Horiba Xplora Plus Raman system components in the Nanoelectronic Lab.

from the plasma lines and directed to a beam-splitter after passing through a set of neutral density (ND) filters. The beam splitter (BS) diverts some part of the light on to an Olympus BX51 optical microscope from top to bottom. Passing down through a proper objective (10×, 20×, 50×, or 100×) laser light is focused onto the sample surface. (The minimum spot size on a flat sample surface is about 1 micron for 100× objective). The scattered light from the sample which is mounted on an XYZ stage with a full computer and hand control in all directions, is collected in the back-scattering geometry by the same microscope objective. Then, scattered light follows the same optical path back up to the beam splitter where a portion of it is transmitted through the BS and will be directed to the entryway of the monochromator via mirrors. Between the BS and the entrance slit of

the monochromator, there exist a rotating set of three Rayleigh rejection notch filters with wavelengths of 785 and 532 nm to be selected by the computer to block the particular excitation wavelength. After reaching the monochromator, the light is detected on an array CCD detector (Synergicity CCD detector). The data signal collected by the CCD is then sent to the controlling computer for analysis.

2.1.2. Photoluminescence

Luminescence spectroscopy is a powerful tool utilized for the optical characterization of semiconductors, especially those applicable for optoelectronic devices. It is a nondestructive technique that can yield information on fundamental properties of semiconductors. Among luminescence spectroscopies photoluminescence (PL) spectroscopy is the most common method, which describes light emission stimulated by exposing the material to light - by necessity with a higher energy than the energy of the luminescence light. Electroluminescence, the technique which excite the electrons by applying an external electric current, is another type of luminescence method. Other luminescence methods are Cathodoluminescence, describes excitation by energy-rich electrons, chemoluminescence procures the necessary energy by chemical reactions and thermoluminescence describes production of radiation from sample by heating. A brief introduction of PL spectroscopy is presented in this section.

Photoluminescence measurement is a non-destructive optical characterization technique for the determining electronic bandgap or detection of defect type of materials. Photoluminescence involves the irradiation of the crystal to be characterized with photons of energy greater than the band-gap energy of that material. Typically, the excitation photon energy is in the range of 0.3-6 eV, depending on the bandgap of the material. In the case of a crystal scintillator, excitation of the crystal creates electron-hole pairs. During the recombination of electron-hole pairs relaxation energy transforms partly into non-radiative and radiative emissions.

Photoluminescence process can be divided into three main phases:

1-Excitation : Electrons absorb energy from external sources, such as lasers, arc-discharge lamps, and tungsten-halogen bulbs, and be promoted to higher energy levels. In this process electron-hole pairs are created.

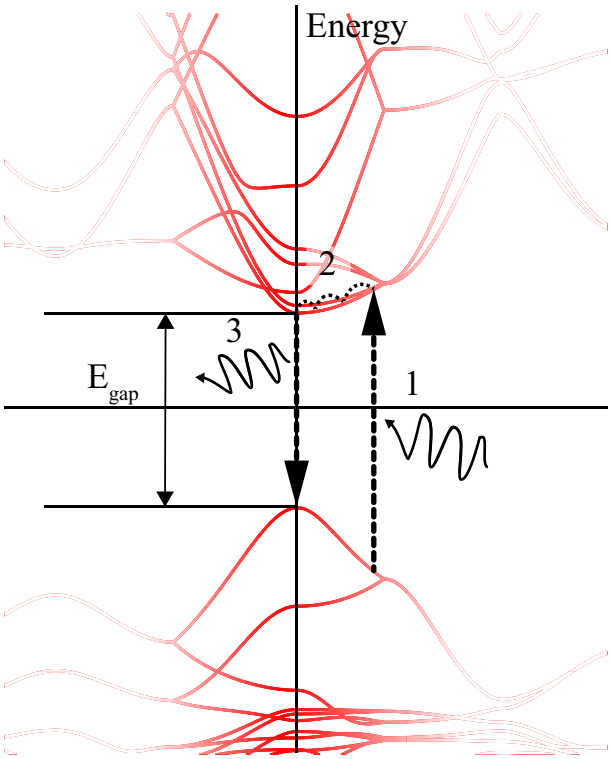

Figure 2.3. Photoluminescence schematic. (I) An electron absorbs a photon and is promoted from the valence band to the conduction band. (II) Electron cools down to the bottom of the conduction band. (III) The electron recombines with the hole resulting in the emission of light with energy $h\nu$.

2-Thermalization : Excited electron-hole pairs relax toward quasi-thermal equilibrium distributions.

3-Recombination : The energy can subsequently be released, in the form of a lower energy photon, when the electron falls back to its ground state. This process can occur radiatively or non-radiatively.

2.1.3. Synthesis

Due synthesis techniques improved very rapidly in recent years, a material with a desired thickness, length and shape can be easily produced. Production methods can be classified into two class that are top-down and bottom-up approaches. Chemical vapor deposition, epitaxial growth procedures, and variety of deposition systems (i.e. magnetron

sputtering, atomic layer deposition, pulse laser deposition) are into bottom-up approaches. On the other hand, exfoliation techniques such as mechanical and chemical exfoliation techniques are classified in top-down approach.

After isolation of single layer graphene by using mechanical exfoliation technique,(Novoselov *et al.*, 2005) exfoliation or growth of lamellar structures have gained remarkable interest. Mostly known 2D materials growth techniques are liquid phase exfoliation, mechanical cleavage, epitaxial growth and chemical vapor deposition (CVD). Coleman et al. reported detailed synthesis of variety of layered materials by using liquid phase exfoliation technique.(Coleman *et al.*, 2011) In addition, epitaxial growth is also very common synthesis method to obtain high quality single layer graphene.(Sutter *et al.*, 2008; Berger *et al.*, 2006) However, due to high cost of production and lack of transferring graphane on different substrates are limited the epitaxial method. Therefore, CVD is the most preferred growth technique to obtain graphene, TMD, or any lamellar materials.(Zhang *et al.*, 2013; Cong *et al.*, 2014; Wang *et al.*, 2013; Reina *et al.*, 2008)

2.1.3.1. Graphene

Graphene samples were grown on 25 μm thick Cu foil by Low Pressure Chemical Vapor Deposition (LPCVD) technique. Before the graphene growth, Cu samples were annealed for 80 min at 990°C in a quartz tube that was evacuated to a pressure of 10^{-5} Torr to increase the grain size on Cu foil. The process was started at room temperature and throughout the process H_2 was utilized to reduce the native oxide layer on the Cu foil. The graphene growth reaction was carried out for 20 min at 850°C while introducing ethylene (C_2H_4), H_2 and Ar at a total pressure of about 1 Torr. All the samples were grown with C_2H_4, H_2 and Ar flow rates of 10, 30 and 150 sccm, respectively. The grown graphene films were transferred onto SiO_2/Si substrate by photoresist (PR) dropcasting. Thick droplets of S1813 photoresist was drop-casted on graphene holding Cu surfaces overnight in the oven at 70°C to gently harden the PR. Then the samples were immersed into $FeCl_3$ solution for etching Cu foils. After the removal of the Cu foil, graphene with PR layer was transferred onto DI water for 30 min to remove the $FeCl_3$ residues. Next, the sample was annealed at 70°C for 30 sec and 120°C for 2 min to re-flow the PR on graphene. This helped PR to liquefy and release the graphene layers on target substrate. Removing PR with acetone yielded large area graphene on the substrate.

2.1.3.2. Molybdenum Disulfide

MoS_2 samples were prepared by liquid exfoliation method. Few-layer MoS_2 were prepared by mixing in 2-3 ml solutions of the MoS_2 powder dissolved in ethanol/water (0.5 mg/ml-2 mg/ml). The MoS_2 suspensions were sonicated for 120 min at a power of 225 W in a water-cooled bath. After the sonication, the final dispersions were centrifuged at 12000 rpm for 30 min and the top 3/4 of the supernatant was collected. Obtained MoS_2 samples, dissolved in ethanol/water, were dropped onto some part of graphene/SiO_2 substrate.

2.1.3.3. Perovskites

Synthesis of Cs-oleate: Cs-oleate solution was synthesized with slight modifications by following the Amgar et al.(Amgar *et al.*, 2017) Cs_2CO_3 (0.2 g), OA (625μL) and ODE (7.5 mL) were loaded to 3 necked flask, and dried under vacuum (150 mbar) at 120°C for 1h. Subsequently, mixture was heated to 150°C under N_2, and reaction was maintained until all Cs_2CO_3 consumed by OA. Afterwards, yellowish Cs-oleate solution was gradually cooled down (it has to be pre-heated to 100°C before using).

Synthesis of $CsPbBr_3$: $CsPbBr_3$ crystals were prepared in four steps with slight modifications based on procedure.(Amgar *et al.*, 2017) An aliquot of 0.125 mL OA, 0.125 mL OLA and 1.25 ml ODE were loaded to glass vial. Subsequently, 0.1 mL of pre-heated Cs-oleate solution was added to mixture, and addition of 0.2 mL of $PbBr_2$ precursor solution (0.4 M, heated for 1 h at 80°C until full dissolution) followed it. After 10 s, 5 mL of acetone were rapidly added to trigger the crystallization of the $CsPbBr_3$. Stirring was maintained for 30 minutes and green precipitates were collected by using centrifuge (6000 rpm, 10 m). Precipitates were re-dispersed in Hexane.

Preparation of Water Contact $CsPbBr_3$ Surface: First, 150 μL $CsPbBr_3$/Hexane dispersion was cast on an oxidized silica substrate (approximately 1 cm^2). $CsPbBr_3$ structures were formed immediately after the quick evaporation of hexane. Second, an aliquot of distilled water was put over the $CsPbBr_3$ coated silica substrate and waited till the water completely evaporates. Characterizations were carried out in ambient conditions. For further aging of the crystals, water driven transitions were conducted by adding desired amount of water. Water contact time was recorded as the total time of exposure.

Synthesis of Undoped Cs_4PbBr_6: Following the synthesis method,(Zhu *et al.*,

2017) 0.4 mmol CsBr and 0.4 mmol $PbBr_2$ were dissolved in 10 mL DMF, and then ligands, 1.0 mL OA and 0.5 mL OAm were added to the solution under vigorous stirring. An aliquot of 0.5 mL from the prepared Cs^+ and Pb^{+2} ions source was injected into 5 mL toluene under vigorous stirring. Solution turned into explicit green color immediately, and after 3-4 min, it was centrifuged under 6000 rpm for 5 min. Precipitates were re-dispersed in hexane.

Synthesis of Mn-doped Cesium Lead Perovskite: As Mn^{2+} source, 10 mmol $MnCl_2$ was dissolved in 10 mL DMF. To obtain Mn-doped cesium lead perovskite, 0.5 mL of the Cs^+ and Pb^{2+} ions source and 0.5 mL of the Mn source were injected into the 5 mL toluene simultaneously under vigorous stirring. Solution turned into bright green-yellow like color rapidly, and after 3-4 min, it was centrifuged under 6000 rpm for 5 min. Precipitates were re-dispersed in hexane. .

2.2. Computational Details

2.2.1. Density Functional Theory

2.2.1.1. Basics of Density Functional Theory

In principle, the properties of a system (many-electron) can be obtained by solving the quantum mechanical wave equation governing of the system dynamics. For non-relativistic systems, this is simply Schrödinger equation. However, many-electron systems generate some of the most outstanding challenges in quantum mechanics for researchers to understand such systems for many applications. Therefore, density functional theory (DFT) is the most practical and popular approach due to solving such challenging system by using quantum mechanical approach.

DFT is the most common quantum mechanical approach to determine the materials properties such as structural, electronic, magnetic, optical, mechanical, and vibrational properties. DFT simply introduces that interacting many particle system can be written as a functional of the ground state density which is a function of position. Due to describing all physical ground state properties of materials in terms of functional of a ground state density, DFT becomes the most used methodology.

Wave function of a system contains all physical information about the system.

The mathematical expression for such a wave function can be represented by the time-dependent non-relativistic Schrödinger equation

$$\hat{H}\Psi = E\Psi \tag{2.9}$$

where the operator $\hat{H}$ is the energy operator known as the Hamiltonian and the E is the corresponding eigenvalue for the Hamiltonian operator. The solution of the Eq. 2.9 is the wave function Ψ which are the eigenfunctions of the Schrödinger equation. When a N-body system is assumed, it is almost impossible to solve the Eq. 2.9 without considering any approximations, unless quantum computer is used. For such a system which contains M nuclei and N electrons, treated as electromagnetically interacting point charges, the non-relativistic many-body $\hat{H}$ has the general form for N-body systems is

$$\hat{H} = -\frac{\hbar^2}{2m_e}\sum_i^N \nabla_i^2 + \frac{e^2}{4\pi\epsilon_0}\Big[-\sum_i^N\sum_I^N \frac{Z_I}{|\vec{r_i}-\vec{R_I}|} + \frac{1}{2}\sum_i^N\sum_{j\neq i}^N \frac{1}{|\vec{r_i}-\vec{r_j}|}. \tag{2.10}$$

$$+\frac{1}{2}\sum_i^N\sum_{J\neq I}^N \frac{Z_I Z_J}{|\vec{R_I}-\vec{R_J}|}\Big]$$

The kinetic energy of the system in terms of electrons and nuclei is included in first two terms. The third and fourth terms are the Coulomb repulsion terms between electrons and nuclei, respectively. Finally, the last term is the Coulombic interaction between an electron and nuclei. M_A in the second term is the ratio of the mass of nuclei to that of an electron, and Z_A is the atomic number of the nuclei A. The ∇_i^2 and ∇_A^2 are Laplacian operators in the coordinates of electron and nuclei, respectively.

2.2.1.2. Hohenberg-Kohn Theorems

The approach is first introduced in 1964 by Hohenberg and Kohn. They proved that the ground state of a quantum many-body system can be considered as a unique functional of density which makes DFT applicable. The approach stands for two main theorems: (i) For any system of interacting particles in an external potential $V_{ext}(\mathbf{r})$, the external potential is a unique functional of the density, (ii) A universal constant for the energy, $E[n]$, can be defined in terms of the density. For the exact ground state of the system, the functional has its global minimum value and the density that minimizes the functional is the exact ground state density $n_0(r)$.

The ground state energy is the expectation value of the Hamiltonian in terms of the ground state wave function as follow,

$$E = \frac{\langle \Psi_0 | H | \Psi_0 \rangle}{\langle \Psi_0 | \Psi_0 \rangle} \equiv \langle H \rangle = \langle T \rangle + \int d^3\mathbf{r} V_{ext}(\mathbf{r}) n_0(\mathbf{r}) + \langle V_{int} \rangle + E_{II} \tag{2.11}$$

2.2.1.3. Hellmann-Feynman Theorem

The theorem, was formulated as it's last form by Hellmann and Feynman, indicates that the force on a nucleus can be written in terms of the charge density of the electron exchange and correlation, and kinetic energy. Therefore, Hellmann-Feynman theorem is essential for DFT calculations, such as structural optimizations. The force conjugates to any parameter in the Hamiltonian,

$$\mathbf{F}_I = -\frac{\partial E}{\partial \mathbf{R}_I} \tag{2.12}$$

where the force depends only on the density of electrons, n, and the other nuclei. When we consider the total energy expression in Eq. 2.11, the force can be written as

$$\mathbf{F}_I = -\frac{\partial E}{\partial \mathbf{R}_I} = -\int d^3\mathbf{r} n(\mathbf{r}) \frac{\partial V_{ext}(\mathbf{r})}{\partial \mathbf{R}_I} - \frac{\partial E_{II}}{\partial \mathbf{R}_I} \tag{2.13}$$

.

2.2.1.4. The Kohn-Sham Equations

Kohn-Sham introduced a method based on the Hohenberg-Kohn theorem that enables one to minimize the energy functional by varying the charge density over all densities containing N electrons. The energy functional given in Eq. 2.14 now takes the form,

$$E[n] = \int n(r) V_{ext}(r) dr + F_{HK}[n] = \int n(r) V_{ext}(r) dr + T[n] + E^{Hartree}[n] + E_{xc}[n] \tag{2.14}$$

where the universal functional, F_{HK}[n], is written as the sum of kinetic energy of non-interacting electrons, T[n], Hartree energy, $E^{Hartree}$, and exchange and correlation energy, E_{xc}. Here, the important step is defining an effective potential which is written as,

$$V^{eff} = \frac{\delta\{\int n(r)V_{ext}(r)dr + E^{Hartree}[n] + E_{xc}[n]\}}{\delta n(r)}, \tag{2.15}$$

which results in the form,

$$V^{eff} = V_{ext}(r) + \int \frac{n(r')}{|r - r'|}dr' + V_{xc}(r), \tag{2.16}$$

where V_{xc}(r) is the exchange-correlation potential derived from the exchange-correlation energy. Using this form of effective potential, the Schrodinger equation in Kohn-Sham DFT takes the form of one-electron like equation as,

$$\left[-\frac{1}{2}\nabla^2 + V^{eff}\right]\phi_i = E_i\phi_i \tag{2.17}$$

where the eigenfunctions, ϕ_i, are known as the Khon-Sham one-electron orbitals which result in the electron density,

$$n(r) = \sum_{i=1}^{N} |\phi_i|^2 \tag{2.18}$$

Due to the form of Eq. 2.18, the effective potential, V^{eff}, depends on the density, n(r). Thus, the Kohn-Sham equation should be solved by the following way: (i) begin with an initial guess of the electron density, (ii) construct the effective potential, V^{eff}, by the knowledge of electron density, (iii) calculate the corresponding Khon-Sham orbitals, ϕ_i, and (iv) calculate the new electron density corresponding to these orbitals and compare with the inital one. Once the convergence is achieved, then the total energy can be calculated in terms of the final electron density. Although the final electron density is known, the exchange-correlation energy is still missing.

2.2.1.5. Functionals of Exchange and Correlation

As mentioned in the previous section the Kohn-Sham equation can be solved if the exchange-correlation functional is known. Given the fact that an exact expression is not available, an approximation need to be introduced. Two such often used approximations are LDA (Local Density Approximation) and GGA (Generalized Gradient Approximation). In this section, the most common two approximations, are widely used in DFT calculations, are explained.

Local Density Approximation (LDA) :

For regions of a material where the charge density is slowly varying, within the local density approximation (LDA) states that the exchange correlation energy, E_{xc}^{LDA} at that point can be considered to be same as the energy exchange-correlation functional of a locally uniform electron gas.

$$E_{xc}^{LDA}[n] = \int n(r)\epsilon_{xc}^{unif}[n]dr \tag{2.19}$$

where ϵ_{xc}^{unif} is known to be the exchange-correlation energy per electron. Although the approximation is basic, LDA gives very accurate results (especially for bulk materials) and forms the core of most modern DFT codes. It even works reasonably well in the systems where the charge density is rapidly varying. Especially, LDA works well for metallic systems. However within this approximation, atomic ground state energies and ionisation energies are underestimated, while binding energies are overestimated.

Generalized Gradient Approximation (GGA) :

Due to unsuitability of LDA for variety materials that electron density varying rapidly, the gradient of the electron density, $\nabla n(r)$, is introduced. For the total energy functional in GGA, exchange-correlation energy is defined as

$$E_{xc}^{GGA}[n] = \int f^{GGA}(n(r), \nabla n(r))dr \tag{2.20}$$

GGA functionals are known as semi-local functionals due to their dependence on the gradient of the electron density.

2.2.2. Computing Phonons

The dynamical stability of materials whether under strain or at equilibrium can be determined by the calculation of the materials' phonon-band dispersion through Brillouin Zone. In theory, matter is known to be composed of atoms oscillating around a certain equilibrium position which is determined by positions of adjacent atoms obeying Hooke's Law. Due to Hooke's Law, restoring forces that the atoms undergo when they are displaced from their equilibrium position occur to describe these oscillations. Hooke's Law can be written as:

$$F = -kX, \tag{2.21}$$

where k is a spring constant and X is the distance between the masses. In this section, methodology for the calculation of phonon-band dispersion with DFT is presented.

As well known that phonons in a crystal do not exist at absolute zero. In DFT calculations, physical properties of a material that is at ground-state is investigated at absolute zero. In Born-Oppenheimer approximation, the electronic motion and the nuclear motion in molecules can be separated. The ions can be assumed as static particles due to having larger masses than electrons. Hence, to obtain phonon creation atoms are displaced trace amount of from their equilibrium positions. In this regard, one needs an approximation to compute phonon in a crystal. So, in order to determine the phonon-band dispersion of a material, the variation of restoring forces with displacement of atoms in a crystal should be known. Thus, the small displacement method is used to achieve for force-constant matrix. The small displacement method is a direct method that calculates the force-constant matrix of the vibrating system by displacing the atoms of the system explicitly. One should also need to consider a sufficiently large supercell for the crystal and then each of the atoms in the supercell should be displaced. The amount of displacement should be taken to be suitable for which the harmonic motion is satisfied. In fact, symmetry can reduce the number of displaced atoms in the primitive unit cell. In DFT calculations, force is calculated based on the use of Hellmann-Feynman theorem. Let us start with the potential energy function of the crystal at low temperature given by,

$$U_{harm} = E_{eq} + \frac{1}{2} \sum_{ls\alpha, l't\beta} \Phi_{ls\alpha, l't\beta} u_{ls\alpha} u_{l't\beta}, \tag{2.22}$$

where E_{eq} is the energy of the crystal at equilibrium positions of the ions while u_{ls} denotes the displacement of the atom s^{th} in the unit cell l along cartesian directions α or β. The term $\Phi_{ls\alpha, l't\beta}$ represents the force-constant matrix which is the second derivative of the harmonic potential energy with respect to the displacements. When the harmonic energy given in Eq. 2.22 is differentiated, one can find the relation between the forces on each atom, F_{ls}, and the displacements, u_{ls}, which is expected to be related linearly as,

$$F_{ls\alpha} = -\sum_{l't\beta} \Phi_{ls\alpha, l't\beta} u_{l't\beta}, \tag{2.23}$$

Once we know the force constant matrix, $\Phi_{ls\alpha, l't\beta}$, then we can define the dynamical matrix as,

$$D_{s\alpha, t\beta} = \frac{1}{\sqrt{M_s M_t}} \sum_{l} e^{i\mathbf{q}(R_{l't\beta} - R_{ls\alpha})} \Phi_{ls\alpha, l't\beta}, \tag{2.24}$$

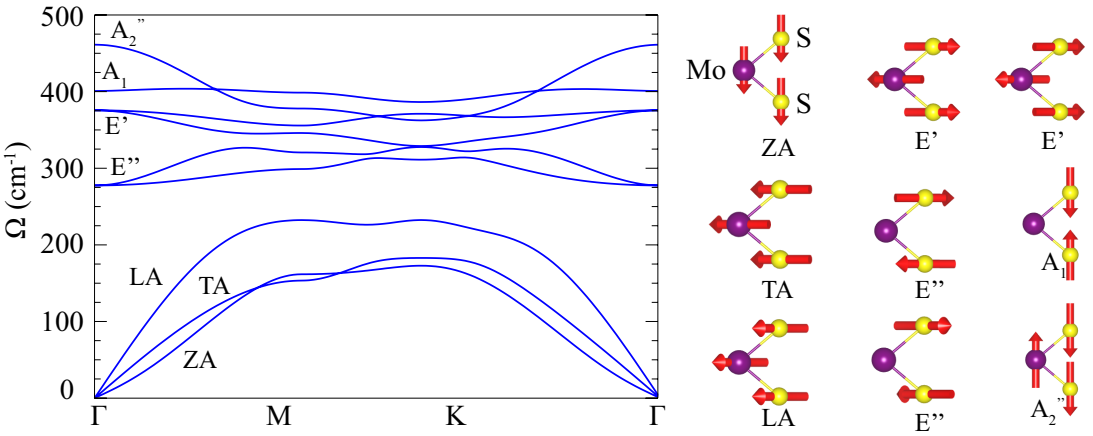

Figure 2.4. Phonon dispersion of monolayer MoS_2 calculated with small displacement method. Corresponding eigenvectors are also showed in the right panel.

where M_s and M_t are the masses of the sth and l^{th} atoms. The term on the exponential function, $R_{l't\beta} - R_{ls\alpha}$, represents the distortion of the atoms in the cartesian components α and β.

One can solve the eigenvalue equation of the force-constant matrix when the matrix is found. The eigenvalues of dynamical matrix give the phonon frequencies of each phonon branch for the crystal at any wave vector, **q**. The total number of phonon branches is nothing but the total number of degree of freedom for the crystal. The size of dynamical matrix is also related to number of phonon branches. For a crystal structure containing N-atoms in its primitive unitcell, there are $3N$ phonon branches, 3 of which are acoustic and $3N$-3 are optical branches. The acoustic branches describe the motion of the individual atoms that move in-phase. On the other hand, for an optical phonon branches, the atoms oscillate out-of-phase. In this thesis, PHON code(Alfè, 2009) was used to calculate the phonon dispersion of materials. This code employs the Hellmann-Feynman forces calculated by the software Vienna *Ab-initio* Simulation Package (VASP)(Kresse and Furthmüller, 1996) which is based on DFT.

2.3. Computational Methodology

This section introduces the general computation methodology which we used to study systems considered and discussed in following chapters. The details for the particu-

lar system is given in the corresponding chapter. Our investigations on the structural, electronic, properties of the ultra-thin materials considered were carried out using the VASP software. The VASP code solves the Kohn-Sham equations (Kohn and Sham, 1965) iteratively for a system with periodic boundary conditions using plane-wave basis set. In order to describe the electron exchange and correlation, the Perdew-Burke-Ernzerhof (PBE) form of the generalized gradient approximation (GGA) was adopted.(Perdew *et al.*, 1996) The spin-orbit interaction, which is essential for some materials (especially for atoms having larger radius), was included in the calculations. The van der Waals (vdW) forces which are important for layered materials were taken into account by using the DFT-D2 method of Grimme.(Grimme, 2006) To obtain the charge distribution on the structures, Bader technique was used.(Henkelman *et al.*, 2006) The diffusion characteristic of the structures was also examined by performing *ab-initio* molecular dynamics (MD) calculations in some cases.

We also calculated the cohesive energy (E_{coh}), which was formulated as

$$E_{Coh} = \big[\sum_i n_{atom(i)} E_{atom(i)} - E_{system}\big]/n_{total}, \tag{2.25}$$

where $E_{atom(i)}$ is isolated single atom energies for i^{th} atom, E_{system} is the ground state energy of the system, while i stands for the number of all atoms for the same species, n_{total} represents the total number of atoms, and $n_{atom(i)}$ shows the numbers of same kind of atoms in the unit cell, respectively. The work functions, which are the energy need to remove an electron from the system, were obtained by subtracting calculated Fermi energy from the calculated vacuum energy.

Structural optimizations were performed by using following parameters. The energy cutoff of the plane-wave basis set was taken to be 500 eV for all calculations. In order to minimize the total energy, the energy difference between the sequential steps was set to 10^{-5} eV. The convergence for the total Hellmann-Feynman forces in the unitcell was taken to be 0.05 eV/Å. In addition, width of the of the Gaussian smearing of 0.05 eV was used for self-consistent calculations and the pressures on the unit cell were decreased to a value less then 1.0 kB in all three directions. For the determination of accurate charge densities, Brillouin Zone integration was performed using dense Γ-centered k-point samplings.

CHAPTER 3

FEW-LAYER MoS_2 AS NITROGEN PROTECTIVE BARRIER

We report experimental and theoretical investigations of the confessed barrier behavior of few layer MoS_2 against nitrogenation. Owing to its low-strength shearing, low friction coefficient and high lubricity, MoS_2 exhibits demeanor of a natural N-resistant coating material. Raman spectroscopy is done to determine the coating capability of MoS_2 on graphene. Surface morphology of our MoS_2/graphene heterostructure is characterized by using optical microscopy, scanning electron microscopy and atomic force microscopy. In addition, density functional theory based calculations are performed to understand the energy barrier performance of MoS_2 against nitrogenation. The penetration of nitrogen atoms through a defect-free MoS_2 layer is prevented by a very high vertical diffusion barrier indicating that MoS_2 can serve as a protective layer for the nitrogenation of graphene. Our experimental and theoretical results show that MoS_2 material can be used both as an efficient nanocoating material and as a nanoscale mask for selective nitrogenation of graphene layer.

Since its successful synthesis,(Novoselov *et al.*, 2005) graphene has become the most intensively studied form among the various carbon allotropes. Following the graphene, the interest in 2D transition-metal dichalcogenides (TMDs) such as MoS_2 has grown rapidly due to their superior properties such as unique quantum luminescence efficiency, (Mak *et al.*, 2010) high channel mobility($\sim$ 200 cm^2 V^{-1} s^{-1}) (Radisavljevic *et al.*, 2011) and large current ON/OFF (Yoon *et al.*, 2011) (60 mV dec^{-1}) (Kong *et al.*, 2013; Zhang *et al.*, 2014; Fang *et al.*, 2012; Ali *et al.*, 2014; Keum *et al.*, 2015; Ramakrishna Matte *et al.*, 2010; Georgiou *et al.*, 2013; Splendiani *et al.*, 2010). Bulk MoS_2 as a coating material has been investigated both theoretically and experimentally for decades because of its stable friction coefficient.(Donnet *et al.*, 1996; Martin *et al.*, 1993; Wahl *et al.*, 1998) The anti-wear properties of MoS_2 have been examined theoretically (Sen *et al.*, 2014) and experimentally (Park *et al.*, 2013) as an oxidation protective nanocoating material as well. Incorporation of nitrogen (N) atoms into the crystal structure by N_2 plasma treatment is a practical method for modifying the physical and chemical properties of materials.(Talbi *et al.*, 2006; Patel *et al.*, 2009)

In this study, we choose N_2 plasma treatment for the investigation of MoS_2 as a protective layer for graphene. Although the physical and chemical effects of N on MoS_2 have been examined,(Vandana *et al.*, 2016; Azcatl *et al.*, 2016) the possibility of using MoS_2 as a protective coating material against nitrogenation for reactive surfaces such as graphene has not been reported yet.

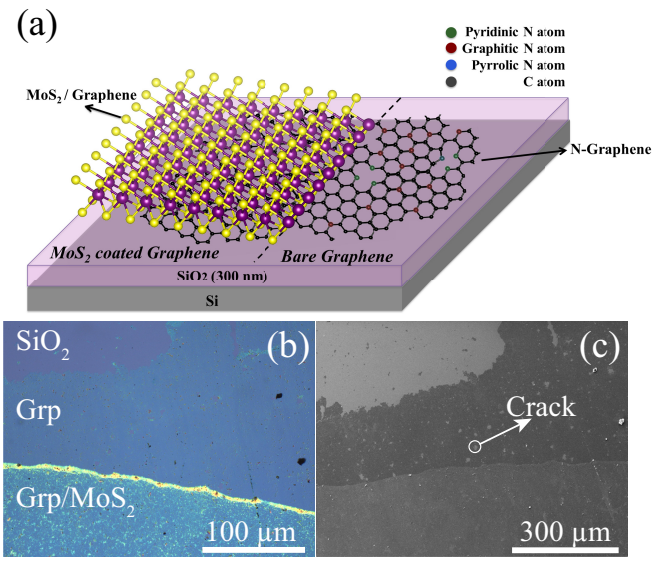

Figure 3.1. (a) Schematic illustration of MoS_2 coated and uncoated regions on the graphene layer (b) optical and (c) scanning electron microscope images of MoS_2 coated graphene.

For investigation of the coating performance of the MoS_2 against nitrogenation, we performed density functional theory-based calculations implemented in the VASP software.(Kresse and Hafner, 1993a; Kresse and Furthmüller, 1996) The exchange-correlation energy was described by the generalized gradient approximation (GGA) using the Perdew-Burke-Ernzerhof (PBE) functional.(Perdew *et al.*, 1996) The van der Waals (vdW) correction to the GGA functional was included by using the DFT-D2 method Grimme.(Grimme, 2006)

The total energy difference between the sequential steps in the iterations was taken to be 10^{-5} eV for the convergence criterion. The total force in the unitcell was reduced to a value of less than 10^{-4} eV/Å. A plane-wave basis set with kinetic energy cutoff of 500 eV was used for all the calculations. To hinder interactions between the adjacent cells, at least 14 Å vacuum space was used along the z-direction. Spin-polarized calculations were performed in all cases. Analysis of the charge transfers in the structures was determined

by the Bader technique.(Henkelman *et al.*, 2006)

The energetics of the vertical indentation and lateral diffusion of N are investigated by considering 3×3 MoS_2 supercell. In the indentation calculations, N atom is approached to MoS_2 layer in the appropriate path by fixing the vertical (all) coordinates at each step of 0.5 Å. In the lateral diffusion calculations, the lateral coordinates are fixed only on the chosen path. One of the Mo atoms, away from the indention and diffusion sites, is not allowed to relax and therefore fix the vertical position of MoS_2 layer in the supercell.

The MoS_2/graphene samples were exposed to N_2 plasma in a RF-discharge plasma chamber. The chamber was pumped down to 30 mTorr and then filled with N_2 gas. After the pressure stabilization in the chamber at 30 mTorr, the capacity coupled RF-discharge plasma was generated using the RF frequency generator. N_2 plasma treatment was applied using a high purity N_2 gas with a flow rate of 40 sccm and a radio-frequency forward power of 7 W. The chamber pressure was set to 1550 mTorr during the experiment. The duration of nitrogenation was done for 15 min.

3.1. Adsorption, Diffusion and Indentation of Nitrogen atoms on MoS_2

In Fig. 3 we show optical and SEM images of MoS_2-coated graphene after nitrogenation. It is clearly seen that while nitrogenation has a negligible effect on the structural properties of MoS_2-coated region, MoS_2-free graphene are significantly doped by nitrogen and therefore N-graphene domains are formed. Therefore, it appears that graphene and MoS_2 display quite different N-adsorption characteristics at the atomic level. In this section, to reveal how N atoms interact with MoS_2 layers we perform state-of-the-art DFT calculations.

MoS_2 crystal is composed of vertically stacked layers interacting via vdW Force. Each single layer of MoS_2 consists of three sublayers in which a sublayer of Mo atoms sandwiched between two sublayers of S atom in a stacking order of ABA. This single layer crystal structure of MoS_2 belongs to the $P\bar{6}m\bar{2}$ space group. Our total energy optimization calculations reveal that lattice constant and the Mo-S bond length are 3.19 and 2.41 Å, respectively. In addition Bader charge analysis indicates that each Mo-S bond that has a covalent character is constructed through contribution of 0.5 (1.0) electron from each S (Mo) atom.

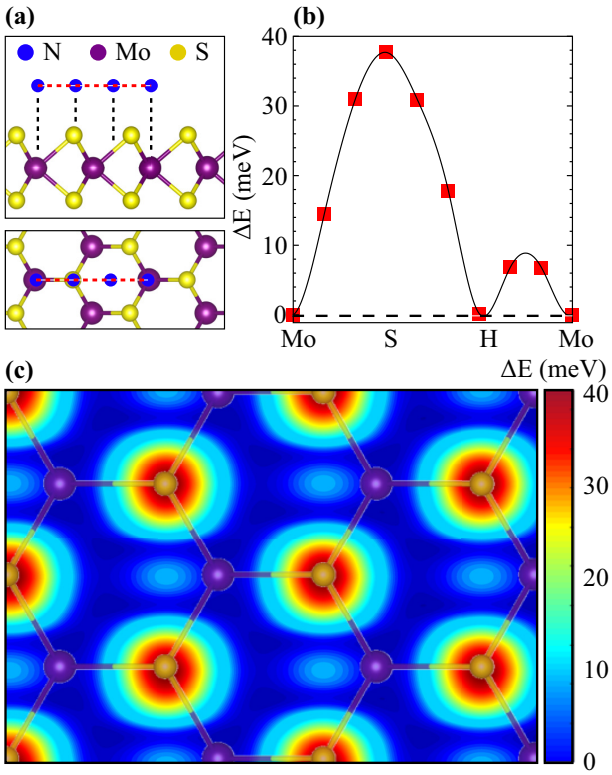

Figure 3.2. (a) Top and side views of the lateral diffusion path (dashed-red line) of N atom (blue circle) on MoS_2. The color code of the circles is given in the inset. (b) The energetics of nitrogen lateral diffusion. (c) 2D energy surface plot of the lateral diffusion of N.

As shown in Fig. 3.1 (a), differing from graphene, diatomic MoS_2 crystal structure has three possible sites that provide favorable adsorption locations for a N atoms: top hollow (H), top of Molybdenum (Mo) atom and top of Sulfur (S) atom. Note that for adsorption calculations of a 48-atom hexagonal supercell of MoS_2, which is enough large to hinder N-N interaction between the adjacent cells, is considered. We found that N atom prefers to be located on top of S atom with bond length of 1.53 Å. Here the binding energy is calculated to be 1.70 eV. The binding energy (E_b) of N atom on MoS_2 is given by

$$E_b = E_{MoS_2} + E_N - E_{MoS_2+N}, \tag{3.1}$$

where E_{MoS_2}, E_N, E_{MoS_2+N} are the total optimized energy of the bare MoS_2, single nitrogen atom and MoS_2-N system, respectively. Here, the S-N bond is formed through the $1.0e$ charge donation from N to underlying S atom. Then, we study lateral diffusion of N atom through the most favorable adsorption sites. To simulate the N plasma treatment accurately, initial position of the N atom is fixed in-plane directions and allowed to relax

in perpendicular direction. As shown in Fig. 3.1(b), Mo and H sites are most favorable

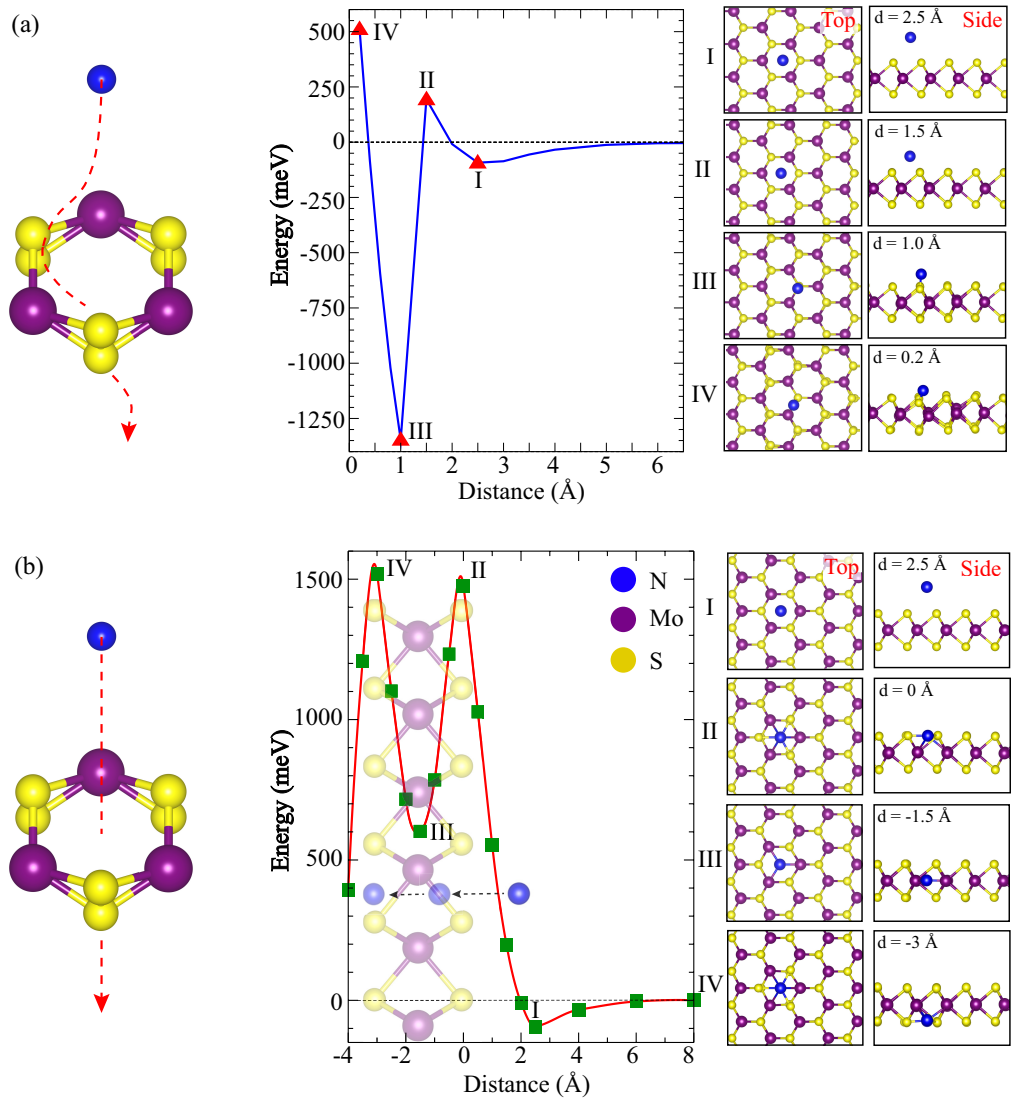

Figure 3.3. The variation of the relative energy of the MoS_2+N system (a) when the N is free to move in the plane direction and (b) when is fixed at each step. In (a), S-N bond occurrence results minimum energy at 1 Å. In (b), N is forced to pass through the hollow site. Here, D stands for vertical distance between N atom and upper S atom.

diffusion sites. However, for diffusion from Mo to H sites through S atom, the energy barrier is calculated to be 38 meV. Considering the position-dependent energy curve around Mo site as a harmonic potential, the jump frequency of the N atom is calculated to be $\nu \approx 36$ THz. Obviously, the high jump frequency arises from low lateral diffusion barrier (38 meV). In addition there is another local diffusion barrier of 8 meV between Mo and H sites (see Fig. 3.1 (b)).

Moreover, we present a 2D energy landscape of the adsorption sites in Fig. 3.1 (c). It appears that N atom is able to diffuse on MoS_2 layer by following the path that connects Mo and H sites through line between S atoms. Considering our experiment for the plasma treatment one may expect adsorption on N atoms on S sites and also their lateral diffusion on MoS_2 surfaces.

In addition, vertical diffusion of N atoms through the MoS_2 layers may also take place during the nitrogen plasma treatment. At the atomic level, depending on the kinetic energy of approaching N atoms such a vertical diffusion can happen in two different ways; (i) N atoms diffuse via a strong interaction with neighboring Mo and S atoms or (ii) N atoms rapidly diffuse through the H site by weak interaction with neighboring atoms.

As shown in Fig. 3.3 (a), approaching N atoms starts to see the local potential of the MoS_2 layer from the distance of 5 Å and finds a local energy minimum 2.5 Å over the surface (**I** point). At such local minima N atoms are simply physisorbed with a binding energy of 100 meV. However, to reach the global minimum at point **III**, where the chemical adsorption takes place, N atoms can easily overcome the energy barrier at point **II**. It is also seen that once N atoms are chemisorbed there is a huge energy barrier (2.2 eV) for further indentation towards the MoS_2 layer.

As the second scenario for vertical diffusion, Fig. 3.3 (b) shows that when N atoms pass through H sites without forming bonds with neighboring Mo and S atoms it experiences much larger energy barriers. For instance, the energy barrier to reach the S level (at point **II**) is calculated to be 1.5 eV. We also see that N atoms can find a local minimum at the Mo level (at point **III**) once they are able pass through the S level. Then, N atoms see another large energy barrier when going from Mo level to lowermost S level (at point **IV**).

To sum up, we investigated the interaction of N atoms with MoS_2 crystal structure by calculating (i) geometry optimization calculations for N atoms on MoS_2 layer, (ii) possible lateral diffusion paths and required energy barriers and (iii) two different vertical diffusion mechanisms. Our results clearly show that N atoms can be adsorbed on the MoS_2 surface. Due to the small energy barriers, they are also able to diffuse laterally. However, their vertical penetration inside the layers is not likely to occur during the plasma treatment.

3.2. Raman Spectroscopy Results

Raman measurements were carried out to observe the structural properties of MoS_2/graphene heterostructure against nitrogenation. Fig. 3.4 shows the Raman spectra of MoS_2/graphene on SiO_2/Si substrate before and after the plasma treatment. It should be noted that Raman spectrum of MoS_2/graphene films was taken from same region before and after nitrogenation process.

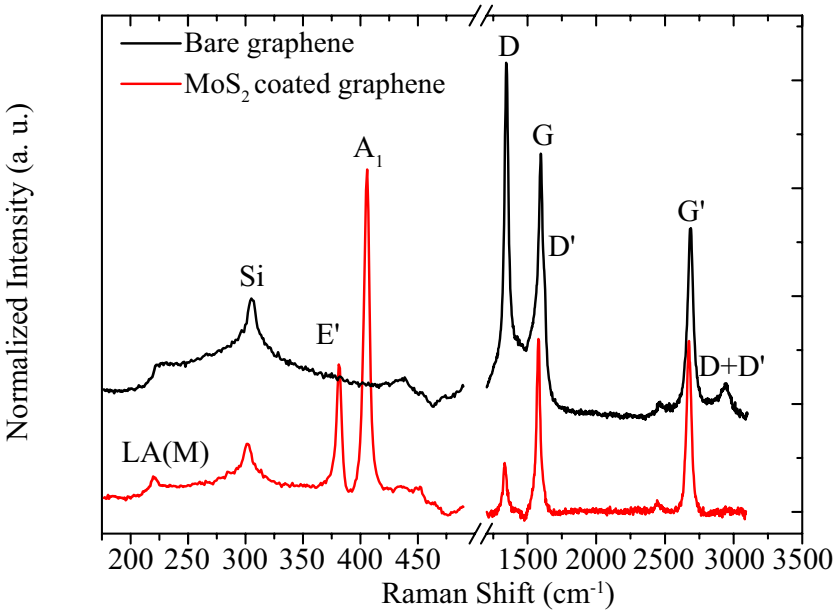

Figure 3.4. Raman measurement of graphene and MoS_2/graphene regions after nitrogenation process. The main Si and SiO_2 peaks located at at the spectral region between 450 and 1250 cm^{-1} were extracted from total spectra. Nitrogenation parameters: nitrogen gas flow 40 sccm, effective RF-power 7 W, plasma time 15 min, nitrogen pressure 1550 mTorr.

Raman signals were recorded in a spectral range between 225-490 and 1200-3500 cm^{-1} using Ar^+ ion laser with 532 nm excitation (1800 grooves/mm grating) wavelength to observe all the characteristic peaks of MoS_2 and graphene before and after nitrogenation process. For each sample, the Raman experiment was repeated five times to check the reproducibility of the measurement. Each spectrum was normalized using LabSpec software.

Since the main Si and SiO_2 peaks seen at 521 cm^{-1} and 900-1000 cm^{-1}, repressed the characteristics peaks of graphene and MoS_2, they were extracted from the total Raman

spectra. After the extraction process, the peaks of graphene and MoS_2 became dominant and the other weak feature around 300 cm^{-1} became visible. This peak corresponds to the SiO_2 on the silicon substrate.(Balendhran *et al.*, 2012)

Two prominent Raman active modes of ultra-thin MoS_2 are measured at 381 cm^{-1} (E′), and 403 cm^{-1} (A_1) (see Fig. 3.4). The E′ mode arises from opposite vibration of two S atoms against Mo atom while A_1 mode is out-of-plane characteristic which corresponds to vibration of only S atoms in opposite direction.(Molina-Sanchez and Wirtz, 2011) Li *et al.* reported that the frequency difference between E′ and A_1 decreases when the thickness of the MoS_2 diminishes.(Li *et al.*, 2012)This behavior is occurred by the reduction of the long-range Coulomb interaction which originates from the increment of the dielectric constant of the material.(Molina-Sanchez and Wirtz, 2011) In addition, we measured a mode centered at 227 cm^{-1} which corresponds to longitudinal acoustic LA(M) mode.(Li *et al.*, 2012; Frey *et al.*, 1999)

The D, G, and G′ peaks are the predominant features in the spectrum of N-graphene as in pristine graphene. When defects or damages occur in the graphene flake, D, D′, and their combination (D+D′) peaks appear in Raman spectrum of graphene.(Beams *et al.*, 2015) They are characterized by the peaks at around 1350, 1585, and 2680 cm^{-1}, respectively. The D′ and D+D′ peaks appear at 1625 cm^{-1} and 2940 cm^{-1}, respectively. The G band corresponds to the doubly degenerate E_{2g} phonons at the Brillouin Zone. The G′ and D bands are all induced by the second-order, double-resonance process and related to zone-boundary phonons. The scattering process involves two zone-boundary phonons for G′ mode; which consists of one phonon and one defect for the D mode. While the D band requires defects to activate it, the G′ band does not require the activation of the defects. Thus, the G′ band is always seen in the Raman spectra of graphene and N-graphene, even when the D band is not observed. In addition, the D′ band arises from the intra-valley, defect-induced, double-resonance process.(Bao *et al.*, 2014; Pimenta *et al.*, 2007) Additionally, D+D′ band is the combination of phonons with different momenta around K and Γ, thus this band require a defect for its activation.(Iqbal *et al.*, 2012; Wang *et al.*, 2013)

As seen in Fig. 3.4, the two intense peaks, G peak at ∼1590 cm^{-1} and G′ peak at ∼2700 cm^{-1}, can be clearly observed for graphene. The peak at ∼1350 cm^{-1}, D peak was presumed to be related to the domain boundaries and growth nucleation sites, its intensity increased after nitrogenation process with respect to that of pristine graphene. The D′ peak (∼1630 cm^{-1}) in the Raman spectrum of N-graphene that was attributed to the inter-valley double resonance scattering process, emerged after plasma process.(Beams *et al.*, 2015; Zafar *et al.*, 2013) In addition, a faint peak at ∼2940 cm^{-1}, the D + D′ peak is also

observed due to the sign of the atomic insertions in the spectral region.(Ye *et al.*, 2014; Majumdar *et al.*, 2007) These results show that the nitrogenation process leads to the appearance of a strong D peak, as well as the emergence of the D′ and D + D′ peaks. This also suggests that the graphene lattice becomes somewhat disordered after nitrogenation process.

3.3. Atomic Force Microscopy Results

We also investigated the morphology of graphene and MoS_2/graphene structures by tapping mode AFM (Figure 3.5) measurements under ambient conditions. All the measurements were conducted with 512×512 data acquisitions at a various scan speed. Oxide-sharpened silicon nitride tips with integrated cantilever (with a nominal spring constant of 48 N/m) were used. For AFM topography measurements, a drop of the MoS_2 suspension was fixed on graphene coated SiO_2/ Si substrate. The AFM images and corresponding line profiles of graphene grains on SiO_2/Si substrate can be seen in Figure 3.5 (a) and (c), respectively.

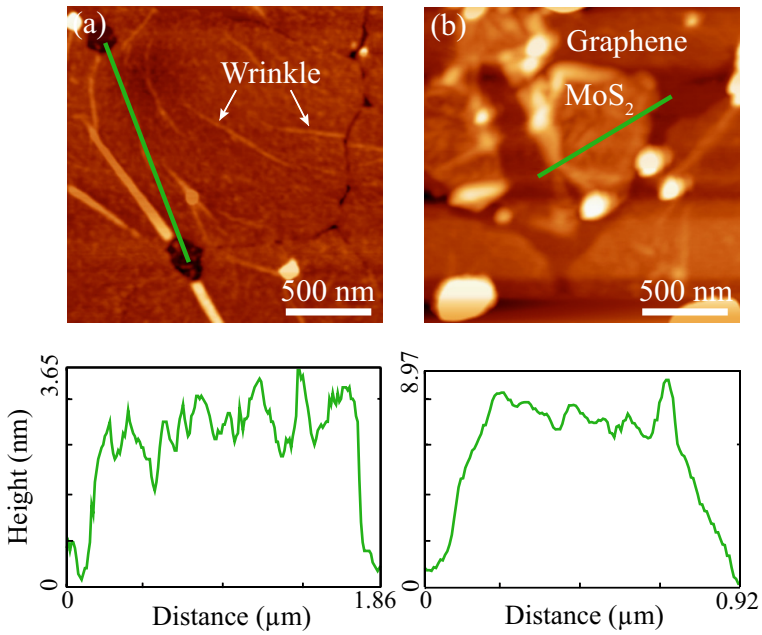

Figure 3.5. Tapping mode AFM images of graphene (a) and MoS_2/graphene (b) on SiO_2/Si substrate with corresponding line profiles.

Some wrinkles which are indicated by the arrows were observed due to the thermal

expansion coefficient mismatch between Cu surface and graphene film during the cooling process (Fig. 3.5 (a)).(Meng *et al.*, 2013) Moreover, small bright particles, related to SiO_2 traces were observed in the AFM image, as reported in similar works.(Jung *et al.*, 2014; Hedayat *et al.*, 2017) Si-riched SiO_2 particles arise from the quartz tube used in the CVD chamber. Since the Si particles from quartz tube react with oxygen (found in Cu foil surface) at high temperatures in LPCVD condition, the formation of SiO_2 can be observed on the surface of the sample after graphene growth procedure. Therefore, they are more likely to be transferred together with graphene onto SiO_2/Si. The height of graphene on SiO_2/Si substrate was determined to be 3.7 nm (see Fig. 3.5 (c)). This thickness corresponds to few layer graphene (Shearer *et al.*, 2016) and this obtained result is in good agreement with the Raman spectroscopy result of the pristine graphene. We found that the graphene grain size range between 2 and 4 nm (see Fig. 3.5).

MoS_2 nanoflakes were also analyzed after dropped onto graphene layer. A high-resolution AFM image of MoS_2/graphene heterostructure on SiO_2/Si substrate is shown in Figure 3.5 (b). It can be clearly seen that the height of the heterostructure is 9-10 nm as measured by the line profile acquired from the AFM image (see Fig. 3.5 (d)). An average thickness of MoS_2 flakes was found to be 5 nm. The MoS_2 flake size is ranged between 2 and 4 nm, as determined by AFM (see Fig. 3.5 (b)).

In this study, we have investigated the coating performance of MoS_2 against nitrogenation both experimentally and theoretically. The present study shows the effect of 2D stacking of MoS_2 and graphene van der Waals layers on their behavior under nitrogen plasma treatment. Raman spectroscopy analysis revealed that nitrogenation process leads to the appearance of a strong D peak, as well as the emergence of D′ and D+D′ peak on bare graphene. However, these findings were not observed on few-layer MoS_2 coated graphene region. Experimental results were also consistent with first principle calculations. Our calculations exhibited that (i) N atom diffuse in lateral direction by following the path through Molybdenum (Mo) and hollow (H) sites, (ii) MoS_2 shows high energy barrier against penetration of nitrogen atom and (iii) large area defect-free MoS_2 can serve as an ideal nanocoating material which can protect underlying surface from nitrogenation. To sum up, MoS_2 material can be used either as an effective nanocoating material or as a nanoscale mask for selective nitrogenation of graphene.

CHAPTER 4

$CsPbBr_3$ PEROVSKITES: THEORETICAL AND EXPERIMENTAL INVESTIGATION ON WATER-ASSISTED TRANSITION FROM NANOWIRE FORMATION TO DEGRADATION

Recent advances in colloidal synthesis methods have led to an increased research focus on halide perovskites. Due to highly ionic crystal structure of perovskite materials, stability issue pops up especially against polar solvents such as water. In this study, we investigate water-driven structural evolution of $CsPbBr_3$ by performing experiments and state-of-the-art first-principles calculations. It is seen that while optical image shows the gradual degradation of yellowish-colored $CsPbBr_3$ structure under daylight, UV illumination reveals that the degradation of crystals takes place in two steps; transition from blue-emitting to green-emitting structure and then transition from green-emitting phase to complete degradation. We found that as-synthesized $CsPbBr_3$ NWs emit blue light under 254 nm UV source and before the degradation, first $CsPbBr_3$ NWs undergoes a water-driven structural transition to form large bundles. It is also seen that formation of such bundles provide longer-term environmental stability. In addition theoretical calculations revealed how strong is the interaction of water molecules with ligands and surfaces of $CsPbBr_3$ and provide atomistic-level explanation to transition from ligand-covered nanowires to bundle formation. Further interaction of green-light-emitting bundles with water causes complete degradation of $CsPbBr_3$ and photoluminescence signal is entirely quenched. Moreover, Raman and XRD measurements revealed that completely degraded regions are decomposed to $PbBr_2$ and CsBr precursors.

Halide perovskites, having the structure of ABX_3 (where A is organic: $CH_3NH_3^+$ (MA), $HC(NH_2)_2^+$ (FA) or inorganic: Cs^+ cation, B is metal cation: Pb^{2+}, Sb^{2+}, Sn^{2+}, and X is halide anion: Cl^-, I^-, Br^-), have been known since 1950s.(MØLLER, 1958) With the discovery of $MAPbI_3$ as photosensitizer in dye-sensitized solar cells (DSSCs) at 2009s,(Kojima *et al.*, 2009) these materials have started to receive more attention.(Stoumpos and Kanatzidis, 2015) Since then, in a short period of time, perovskite solar cells have become able to improve the conversion efficiency from 3.81% to almost 20%.(Jeon *et al.*,

2015; Kojima *et al.*, 2009; Liu and Kelly, 2014; Zhou *et al.*, 2014)

Even though all-inorganic perovskites are better in terms of intrinsic stability than the organometallic halide ones, stability is still a challenge especially against moisture and polar solvents such as water, ethanol, acetone, etc.(Kovalenko *et al.*, 2017; Iso and Isobe, 2018; Huang *et al.*, 2017; Li *et al.*, 2017) Such high chemical instability mainly stems from high ionic character of the compounds. However, practical applications require deeper understanding of degradation mechanisms for synthesis of highly stable halide perovskites under ambient conditions.

Degradation mechanisms at atomic-level and possible stabilization techniques are still open questions in the growing field of perovskite nanocrystals. A very recent study of Yuan *et al.* reported that both light and humidity may degrade $CsPbI_3$ quantum dots.(Yuan *et al.*, 2018) Recent perspective study on lead halide perovskite solar cells (PSCs) enlightens the defect tolerance and stability of the material.(Huang *et al.*, 2017) Lejitas and co-workers reviewed strategies to overcome the issues of structural, thermal, and atmospheric degradation of $CsPbX_3$ nanocrystals.(Leijtens *et al.*, 2017) In addition to experimental studies, tremendous efforts have been also performed on PSCs by carrying out density functional theory (DFT) calculations.(Iyikanat *et al.*, 2017; Yin *et al.*, 2015; Geng *et al.*, 2014; Kawai *et al.*, 2015; Haruyama *et al.*, 2015) Although the organic-inorganic hybrid lead halide perovskites have been studied theoretically and experimentally, the pure inorganic alternative, $CsPbBr_3$ phase, has been recently found to possess most of the good properties of the hybrid lead halide counterpart.(Bekenstein *et al.*, 2015; Protesescu *et al.*, 2015)

Cesium carbonate (Cs_2CO_3, 99.9%, Sigma-Aldrich), lead(II) bromide ($PbBr_2$, $\geq$98%, Sigma-Aldrich), oleic acid (OA, 90%, Alfa Aesar), oleylamine (OLA, 90%, Sigma-Aldrich), 1-octadecene (ODE, 90%, Sigma-Aldrich), dimethylformamide (DMF, $\geq$99.9%, Tekkim), Hexane ($\geq$98%, Sigma-Aldrich) and acetone (Merck , $\geq$99.5%) were purchased and used as received without any further purification. Oxidized silica substrate was purchased from University Wafers.

The diffraction profile of the $CsPbBr_3$ structures was recorded with an X-ray diffractometer (XRD, X'Pert Pro, Philips, Eindhoven, the Netherlands). Scanning electron microscopy (SEM; Quanta 250, FEI, Hillsboro, OR, USA) was used to determine $CsPbBr_3$ morphology in back-scattering electron (BSE) detectors. Image of the degraded crystals were captured via optical microscope (BX 53, Olympus, Tokyo, Japan). Emission spectra was determined by USB2000+ spectrometer (Ocean Optics Inc., Dunedin, FL, USA) via a premium fiber cable. Raman (Horiba Xplora plus) was used to determine

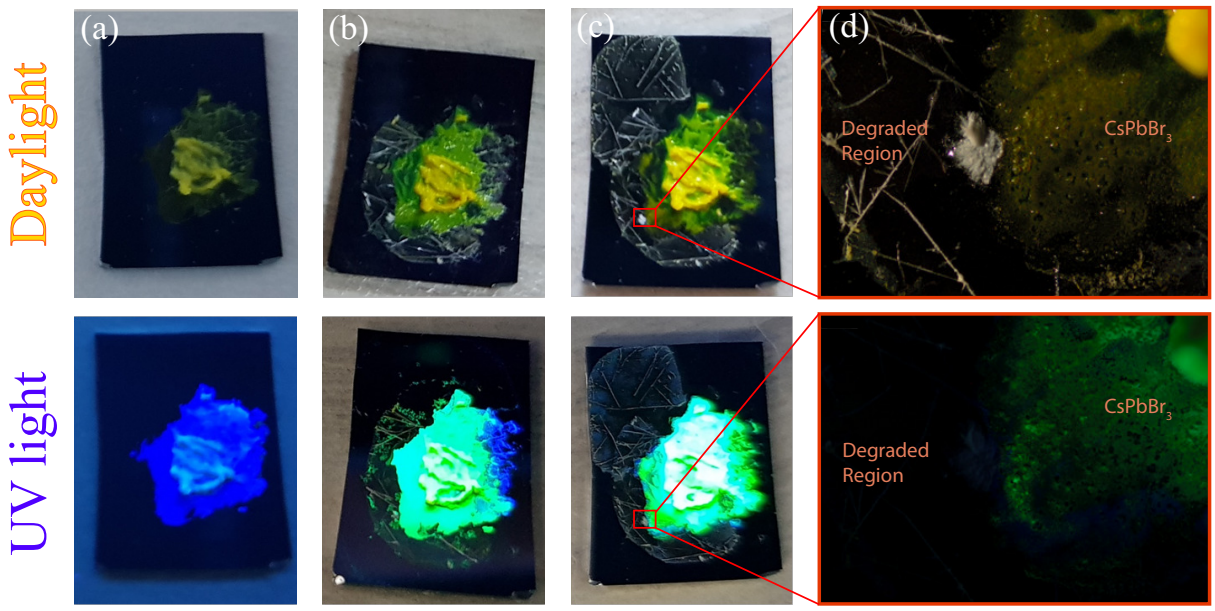

Figure 4.1. Appearance of $CsPbBr_3$ under daylight and UV illumination; (a) initially after casting, (b) after 24 and (c) 144 hours treated with water, respectively. Focused region in (c) presents the optical microscope image of related sample under daylight and UV excitation.

fingerprint Raman-active vibrations of $CsPbBr_3$ structures. Absorption was collected via using OLYMPUS (CX-31) optical microscope integrated with USB2000+ spectrometer.

To investigate interaction between Cs- and Pb-rich surfaces of orthorhombic $CsPbBr_3$ with water, OA, and OAm molecules, we performed density functional theory-based calculations using the projector augmented wave (PAW) (Kresse and Joubert, 1999; Blöchl, 1994) potentials as implemented in the VASP.(Kresse and Furthmüller, 1996; Kresse and Hafner, 1993b) The local density approximation (LDA) (Perdew and Zunger, 1981) was used with the inclusion of spin-orbit coupling (SOC) to describe the exchange and correlation potential as parametrized by the Ceperley and Alder functional to describe the exchange and correlation potential.(Ceperley and Alder, 1980) Bader technique was used to analyze the partial charge transfer on the atoms.(Henkelman *et al.*, 2006)

A plane-wave basis set with kinetic energy cutoff of 500 eV was used for all the calculations. The total energy difference between the sequential steps in the iterations was taken to be 10^{-5} eV for the convergence criterion. The total force in the unitcell was reduced to a value of less than 10^{-4} eV/Å. Γ-centered k-point meshes of 3 × 3 × 3 were used. A vacuum space of 10 Å was incorporated to avoid interaction with adjacent surfaces. Gaussian smearing of 0.1 eV was used for electronic density of states

calculations. Spin-polarized calculations were performed in all cases.

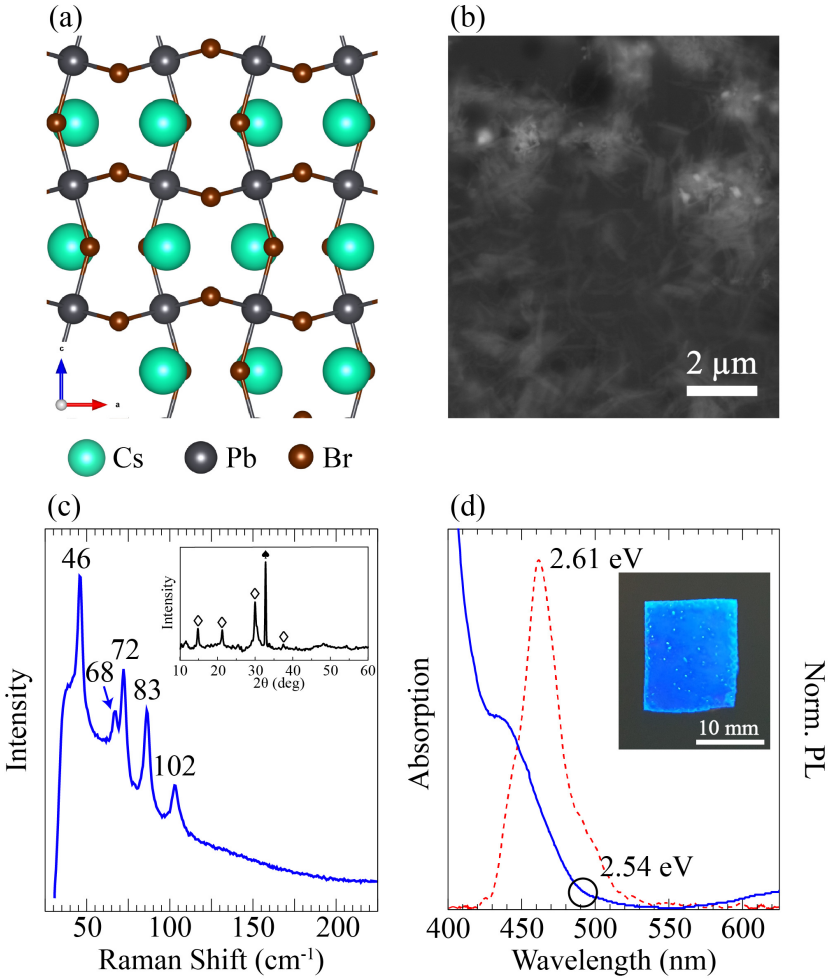

Figure 4.2. (a) Crytal structure, (b) SEM image, (c) Raman measurement (inset; XRD pattern) and (d) photoluminescence and absorption spectra (inset; photograph under 254 nm UV light) of $CsPbBr_3$ NWs.

Structural and electronic evolution of the water interacting $CsPbBr_3$ crystals were captured under both daylight and UV light (254 nm) at different times, and presented in Fig. 4.1. First, silica substrates were identified as neat showing black color under both daylight and UV. After dropping the $CsPbBr_3$ / hexane dispersion over the substrate, the sample was observed to become green and yellowish like color under daylight and explicit blue under UV. After interacting with water molecules about 24 hours, as shown in Fig. 4.1 (b), $CsPbBr_3$ turns into explicit greenish color with some white crystals move around expanding the sample volume, which exhibits green emission covering large area while leaving a small region as emitting blue under UV light. Further interaction with water

leads to formation of white and relatively large crystals that do not exhibit luminescence under UV illumination due to possible degradation (Fig. 4.1 (c) and (d)). Monitoring the degradation under UV light reveals that degradation occurs in two different steps: formation of green-emitting phase and complete degradation. Therefore, following chapters are devoted to experimental and atomic-level understanding of degradation of $CsPbBr_3$ crystal by water.

4.1. Characteristic Properties of Blue Light Emitting $CsPbBr_3$

$CsPbX_3$ nanocrystals exhibit three different structural phases: cubic (Pm-3m), orthorhombic (Pnma), and tetragonal (P4/mbm).(Smith *et al.*, 2015; Wang *et al.*, 2015; Cottingham and Brutchey, 2016) At room temperature, $CsPbBr_3$ has been shown to possess a thermodynamically preferred orthorhombic structure.(Zhang *et al.*, 2015) In our calculations, structural properties of orthorhombic $CsPbBr_3$ are investigated, as seen in Fig. 4.2 (a). Structural analysis reveals that optimized lattice parameters of bulk $CsPbBr_3$ is a = 8.34 Å, b = 7.89 Å, and c = 11.29 Å. Each Br atom bonds with two Pb atom with a bond length of 2.92 Å. Br-Pb-Br bond angle varies between 85° and 90°. Bader charge analysis shows that each Br atom receives 0.6e/atom from Cs (0.8e/atom) and Pb (1e/atom) atoms. Besides, it is seen that the bond between Pb and Br atoms has strong ionic character. On the other hand, Cs atoms slightly bind to the other atoms in the system even though the system receives charge from Cs atoms.

SEM image presented in Fig. 4.2 (b) shows the morphological characteristics of $CsPbBr_3$ crystals. It is observed that the crystals, even though they have negligible aggregation, possess 1-dimensional shape. By selecting the individual ones from the image reveals that these NWs have nano scale diameter ($\sim$ 50 nm) and submicron lengths ($\sim$ 0.5-1.5 μm).

Raman measurement are carried out at room temperature with 785 nm laser excitation shows that $CsPbBr_3$ has five Raman-active modes as presented in Fig. 4.2 (c). The vibration of the metal-halide sublattice, prominent peak of $CsPbBr_3$, is measured at 72 cm^{-1}. According to a previous Raman study of the $CsPbCl_3$ crystal with *Pnma* phase,(Calistru *et al.*, 1997) peak at 72 cm^{-1} is assigned to the vibrational mode of $[PbBr_6]^{4-}$ octahedron and motion of Cs^+ cations. Moreover, it is seen that additional peaks appear at 46, 68, 83 and 102 cm^{-1}.

For further information on the crystal structure, XRD pattern of $CsPbBr_3$ NWs is also presented in the inset of Fig. 4.2 (c). Diffraction pattern is in good agreement with

the standard orthorhombic phase as the crystal structure of $CsPbBr_3$, where 2θ at $15°$, $22°$, $30°$, and $31°$ reflections, marked with tile symbol, correspond to the (110), (020), (004), and (220), respectively.(Cottingham and Brutchey, 2016) The peak at $33°$ is due to silicon wafer. Among the reflections, asymmetry between (004) and (220) planes indicates a good morphological support in the sense of producing NW geometry.

Optical bandgap of $CsPbBr_3$ NWs was determined via absorption spectrum, as shown in Fig. 4.2 (d). Based on the data presented in Fig. 4.2 (d), NWs show broad range of absorption starting from the wavelength of $\sim$488 nm, which follows an increasing trend with the decreasing wavelength. Absorption rate grows almost exponentially below $\sim$425 nm. To estimate bandgap, wavelength of where the absorption begins is considered, which gives rough value about 2.54 eV. The bandgap, which corresponds to a wavelength of 488 nm is verified by photoluminescence (PL) spectrum, which is given with a dashed line in Fig. 4.2 (d), of the NWs. In that spectrum, it is observed that NWs have narrow (FWHM = 38 nm) blue emission with maximum PL intensity at 475 nm under 254 nm UV light. The wavelength, which corresponds to 2.61 eV, is very close to the estimated bandgap value above. For visualization, photograph of the casted $CsPbBr_3$ NWs over silica substrate under UV illumination, which is an explicit blue, is presented as the inset of Fig. 4.2 (d).

4.2. Water-assisted Transition from Blue to Green Light Emitting Structure

While $CsPbBr_3$ preserves its yellowish color during the water treatment, water-driven transition into the green-emitting phase can be observed under UV. As shown in Fig. 4.3 (a), the transition from blue to green emission due to water was recorded at different times. After 24 hours, emission is observed to consist of two distinct signals; one signal around 450 nm which represents the individual NWs (verifies the blue region in Fig. 4.1 (b)) and a signal around 500 nm (greenish), which indicates a significant red-shift. From 24 hours to 70 hours, blue signal reduces and finally disappears while greenish signal increases and dominates the spectrum.

SEM image shown in Fig. 4.3 (b) reveals the formation of larger crystals that were grown particularly in longitudinal direction compared to individual NWs, reaching sizes of >5 μm. The inset in Fig. 4.3 (b) demonstrates an image that was taken with higher magnification over the edge of one of these crystals. It was observed that the tip

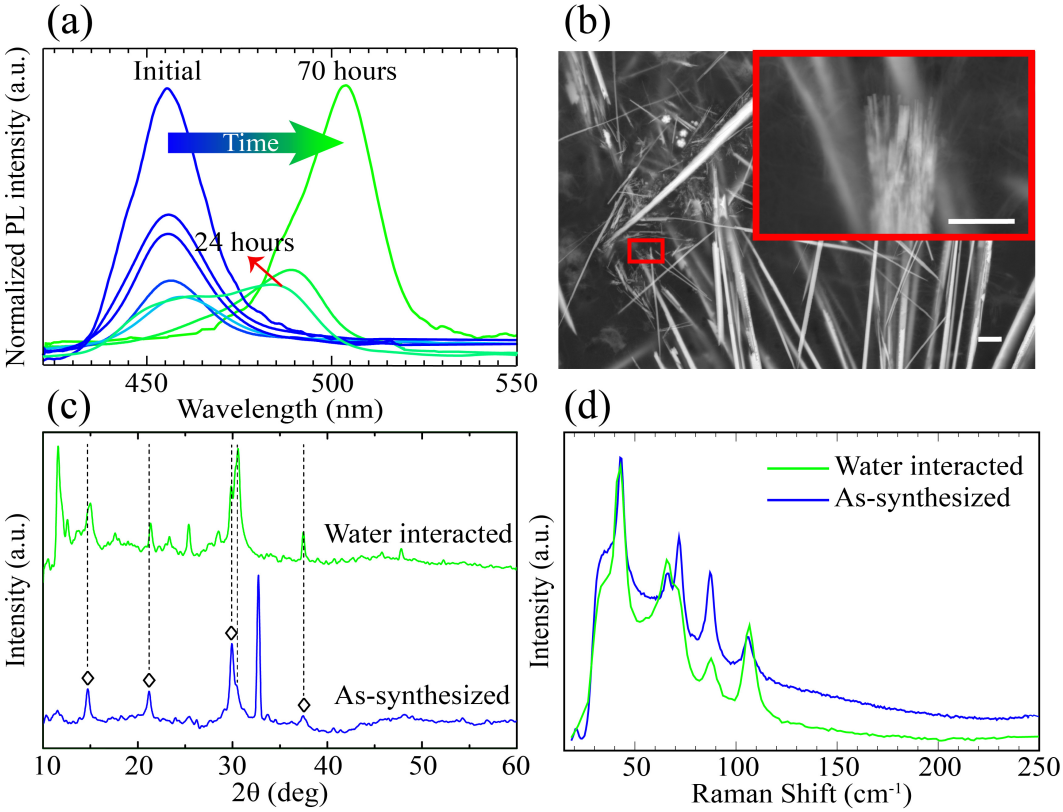

Figure 4.3. (a) Time-dependent photoluminescence of as-synthesized NWs interacting with water, (b) SEM image of the resulting NW structure after 24 hours of interaction, and (c)-(d) are XRD measurement and Raman spectra of both as-synthesized and water interacted samples. Scale bars are 2 μm.

of a large and rod-like crystal consists of many NWs, and inset of Fig. 4.3 (b) verifies the bundle formation through individual NWs. Therefore, the water-driven red-shift in emission clearly stems from quantum size effect, which is led by the structural transition from nanowire to bundle.

Crystal structure of green-emitting $CsPbBr_3$ was determined by x-ray diffraction measurement, as shown in Fig. 4.3 (c). It is seen from the 2θ reflections at $15°$, $22°$, $30°$, and $31°$ confirm that blue and green-emitting phases correspond to the same crystal structure. However, emergence of additional reflections 2θ at $12°$ and $25°$ are indication of locally formed Cs_4PbBr_6.(Zhang *et al.*, 2017) Raman spectra of green emitting $CsPbBr_3$ bundles shows that prominent peak at 72 cm^{-1} and the other 4 modes still exist, as presented in Fig. 4.3 (d). Raman activity of water interacted region is the same with as-synthesized $CsPbBr_3$ crystals. Therefore, vibrational characteristics of $CsPbBr_3$ NWs remain unchanged through the bundle formation.

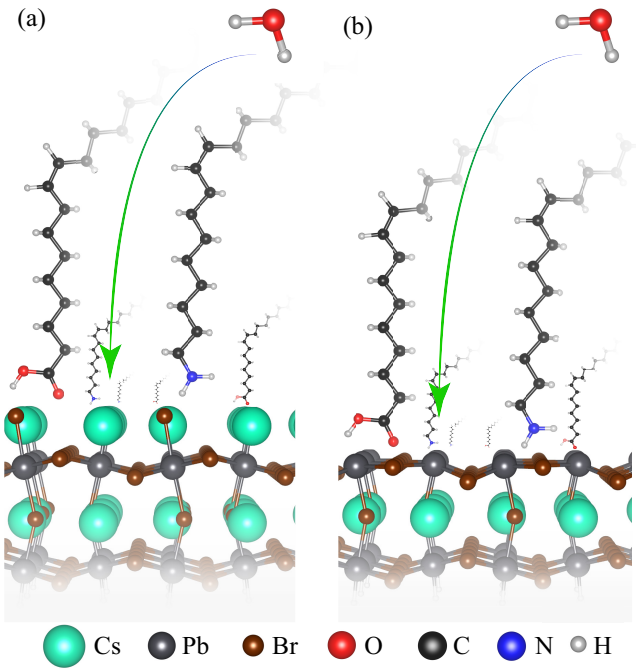

Figure 4.4. Side views of (a) Cs-terminated and (b) Pb-terminated $CsPbBr_3$ surface.

Here, for deeper understanding of the water-driven nanowire-to-bundle transformation, we employ state-of-the-art first principles calculations. In order to examine all possible surfaces, we truncated bulk orthorhombic $CsPbBr_3$ at Cs and Pb surfaces as shown in Fig. 4.4 (a) and (b). Both surfaces are saturated with H atom to evade possible magnetization in the system.

For the surface cut from Cs atoms, bond angle between Pb and Br atoms is calculated to be the same as that of bulk form. Due to the surface relaxation Pb-Br bond length varies between 2.86-2.94 Å. In addition, Bader charge analysis reveals that Pb atom donates (1.1e) to Br atoms (0.5-0.6e). For Pb truncated surface, it is clearly seen that there is a surface reconstruction at which Pb-Br atoms make a line ($\sim 180°$), as shown in Fig. 4.4 (b). The Pb-Br bond length varies between 2.82 and 2.95 Å which is wider range than that of in Cs-terminated one. Bader charge analysis of Pb-terminated surface reveals that while Pb atoms donate 1.1e, Br atoms receive 0.5-0.6e.

Total energy optimization calculations of H_2O molecules on two different surfaces show that water molecules prefer to bind on the bridge site on Pb-Br bond. In addition, H_2O molecules bind to both surfaces via lone pairs of O atoms. For Cs-terminated surface, bond length between O and Cs atoms is calculated to be 2.91 Å. Charge analysis shows that H_2O molecule receives 0.2e from Cs atom. Binding energy (E_b) of the molecule is

calculated to be 649 meV. H_2O molecule bind to Pb atom with a bond length of 2.53 Å. The molecule prefers to bind the surface through O atom. without charge transfer between the molecule and the surface. On this surface, E_b of the molecule is calculated to be 808 meV. Apparently, H_2O molecules strongly interact with the different surfaces of $CsPbBr_3$.

We also calculate the interactions between surface ligands, OA and OAm, with the NW surfaces. Optimized structures of the ligands are shown in Fig. 4.4. On the Cs-terminated surface, E_b of OA is calculated to be 698 meV. On the contrary, E_b of water molecule on the same surface is calculated as 649 meV and it is comparable with OA' binding energy. In addition E_b of OAm on the same surface is found to be 463 meV. For Pb-terminated surface, binding energy of OAm is calculated to be 874 meV. It is comparable with E_b of H_2O molecule (808 meV) on the same surface. Furthermore, binding energy of OA molecule is found to be 221 meV.

To provide a complete discussion, interaction of water with ligands is also taken into account. It is found that E_b of H_2O to OA and OAm is calculated to be 898 and 550 meV, respectively. It can be concluded that oleic acid is more likely to bind with water molecule than any other surfaces of $CsPbBr_3$. So H_2O molecules mediate the detachment of OA molecules from the surface of the NWs. Hence, minor phase transition from $CsPbBr_3$ to Cs_4PbBr_6 may arise from lack of OA that leads to excessive OAm on the surface of the NWs.(Udayabhaskararao *et al.*, 2017)

As a result, the binding energies of water and ligands on the surface of $CsPbBr_3$, reveal that water is responsible for the removal of ligands over the $CsPbBr_3$ surface. It appears that detached ligands on the surface of NWs yield to formation of bundles composed of individual NWs.

4.3. Complete Degradation

This section is devoted to understanding of how the green light emitting $CsPbBr_3$ bundles interact with water and become completely degraded. As shown in Fig. 4.5 (a), further water treatment of green-emitting phase having intense PL signal at 500 nm results in transformation into another phase which has no optical activity. Optical image presented in Fig. 4.5 (b) reveals that the formation of these non-emitting crystal structures is accompanied by formation white colored domains.

For understanding of the final structure in terms of crystallographic perspective, XRD measurements were employed to white crystals, namely non-emitting large bundles. XRD patterns of degraded and as-synthesized NWs, CsBr, and $PbBr_2$ are presented in

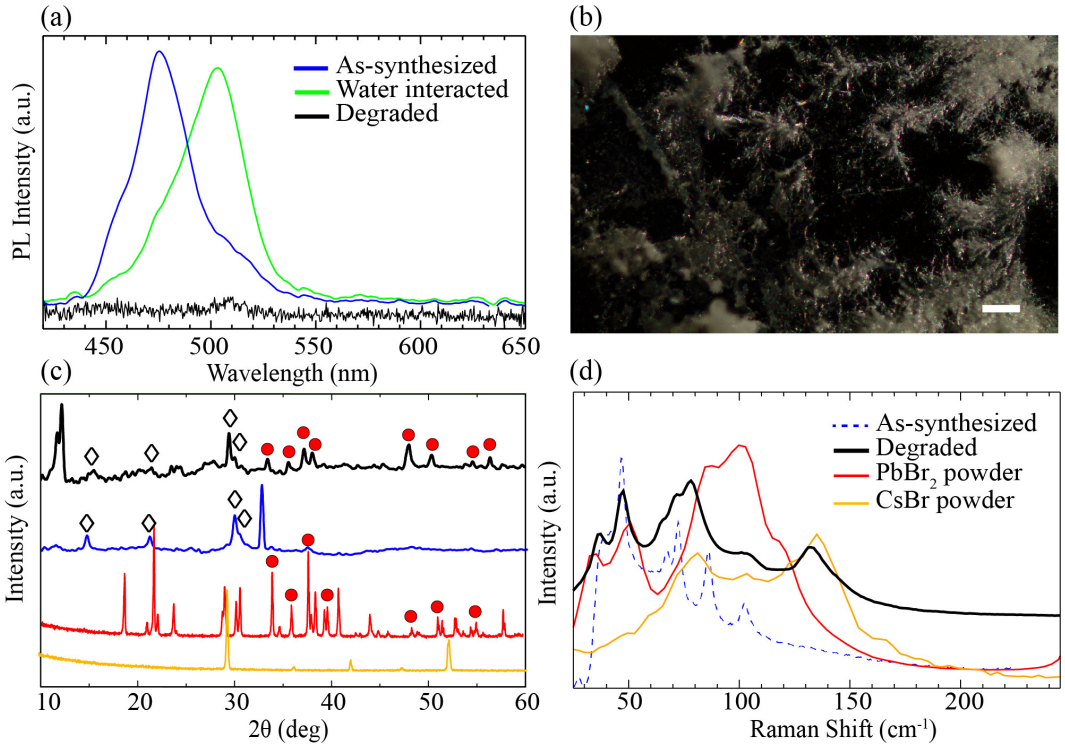

Figure 4.5. (a) PL measurement of $CsPbBr_3$ NW to degraded crystals, (b) optical image from non-emitting bundles, and (c) X-ray diffraction pattern and (d) Raman measurement of $CsPbBr_3$ NWs, degraded crystals, CsPb and $PbBr_2$ powder. Scale bar is 50 μm.

Fig. 4.5 (c). Identical reflections (15° and 30°) of perovskite, which indicate (110) and (004) planes, is still observed. The reflections of degraded form may be assigned to residual NWs. However, according to additional reflections of degraded crystals, it can be said that crystallographic nature shows alteration as much as transformation shows in morphology. Nevertheless, the additional reflections cannot be unambiguously attributed to raw materials (CsBr and $PbBr_2$), although several reflections (e.g. 38°, 48°, and 52°) are already matched.

For further analysis of non-emitting regions, we also present the Raman spectrum of degraded regions of the crystal structure in Fig. 4.5 (d). It is seen that the intensity of the prominent Raman mode of $CsPbBr_3$ at 72 cm^{-1} is significantly decreased and is almost disappeared. Moreover, some novel modes, apparently stemming from the precursors $PbBr_2$ and CsBr emerge at 38 and 130 cm^{-1}.(Isupova and Sobolev, 1968; Willemsen, 1971) Therefore, as confirmed by the vibrational spectrum, complete degradation of $CsPbBr_3$ from green-emitting phase occurs by turning the material into its constituents.

In conclusion, we investigated how $CsPbBr_3$ perovskite is degraded by water using Raman, XRD, PL measurements and state-of-the-art computational techniques. It is seen that even though no significant changes were visible to naked eye during degradation, UV illumination reveals that the complete degradation takes place in two different steps (i) transformation from nanowires to bundles and (ii) complete degradation from bundles to constituents. As verified by the first-principles calculations, competing interactions between water molecule, oleic acid, and oleylamine on the surface determine whether the structure crystallizes into a nanowire, bundle or degraded form. Our photoluminescence, Raman and XRD measurements also revealed that during the transition from blue- to green-emitting phase of the $CsPbBr_3$ crystal symmetry remains the same. In the final step, complete degradation of $CsPbBr_3$ structure takes place by formation of CsPb and $PbBr_2$ powders. We believe that these results provide the important advances in understanding the water-driven degradation of perovskite crystals and may construct a theoretical basis for fundamental investigations on their stability.

CHAPTER 5

MONITORING THE DOPING AND DIFFUSION CHARACTERISTICS OF MN DOPANTS IN CESIUM LEAD HALIDE PEROVSKITES

Cesium lead perovskites, in the form of $CsPbX_3$ or Cs_4PbX_6, have been widely used for various optoelectronic applications due to their exceptionally good optical properties. In this study, the effect of Mn doping on the structural and optical properties of cesium lead halide perovskite crystals are investigated from both experimental and theoretical point of views. It is found that adding $MnCl_2$ during the synthesis not only lead to Mn-driven structural phase transition from Cs_4PbBr_6 to $CsPbCl_3$ but also triggers the Br^- to Cl^- halide exchange. On the other hand, it is observed that, under UV illumination, the colour of Mn-doped crystals changes from orange to blue in approximately 195 hours. While the intensity of Mn-originated photoluminescence emission exponentially decays in time, the intensity of $CsPbCl_3$-originated emission remains unchanged. In addition, diffusive motion of Mn ions results in both growing population of MnO_2 at the surface and transition of the host into a cesium rich Cs_4PbCl_6 phase. This work offers a detailed understanding about the doping process of cesium lead perovskites including both its pre- and post-doping conditions.

As a member of colloidal semiconductor nanocrystal (NC) family, cesium lead halide perovskites in the form of $CsPbX_3$ (X: Cl^-, Br^-, I^-) offer outstanding optical properties such as high photoluminescence quantum yield (PLQY) and defect-tolerance, and wavelength tunability. Cesium lead perovskites are potential candidates in a variety of optoelectronic and photonic applications such as solar cells,(Kulbak *et al.*, 2015; Beal *et al.*, 2016) photodetectors,(Ramasamy *et al.*, 2016; Song *et al.*, 2016) display,(Wang *et al.*, 2016; Güner *et al.*, 2018) light-emitting diodes,(Song *et al.*, 2015; Li *et al.*, 2016, 2017) and lasers.(Eaton *et al.*, 2016; Xu *et al.*, 2016; Yakunin *et al.*, 2015) Doping is a well-known strategy that may lead to novel functionalities and significant improvement in device efficiency.(Meinardi *et al.*, 2017; Norris *et al.*, 2001; Pradhan and Sarma, 2011; Pradhan *et al.*, 2005; Rice *et al.*, 2016; Fainblat *et al.*, 2016; Santra and Kamat, 2012; Erickson *et al.*, 2014; Erwin *et al.*, 2005; Bryan and Gamelin, 2005; Norris *et al.*, 2008; Pradhan *et al.*, 2017) To date, various ions that are used as dopant for cesium halide per-

ovskite NCs have been reported.(Pan *et al.*, 2017; Liu *et al.*, 2017; Zhou *et al.*, 2017; Hu *et al.*, 2018; Guria *et al.*, 2017; Van der Stam *et al.*, 2017) Among those, doping of cesium lead perovskites with Mn ions started to attract a significant attention recently since the presence of Mn ions can add novel optical and magnetic features to NCs.(Guria *et al.*, 2017; Nag *et al.*, 2008; Mir *et al.*, 2017; Wang *et al.*, 2017; Lin *et al.*, 2017) For instance, Mn ions open an extra emission channel at $\approx$ 590nm due to transfer of exciton energy from host to *d*-states of Mn.(Liu *et al.*, 2016; Rossi *et al.*, 2017; Parobek *et al.*, 2016) However, doping may create charge and size imbalance at the host lattice of these NCs that causes change in both the crystal structure, and the emission characteristics.(Norris *et al.*, 2008; Karan *et al.*, 2011; Acharya *et al.*, 2013; Kamat, 2011)

In this study, the effect of Mn ions on the structural and spectral properties of cesium lead halide perovskite crystals was investigated through performing experiments and first principle calculations. First, it was observed that the presence of Mn ions result in a phase transition from Cs_4PbBr_6 to $CsPbCl_3$ during the doping process. Moreover, dopant-induced emission was found to decay exponentially in time due to diffusion of Mn atoms through crystal surface. During the diffusion, apart from the optical degradation, structural changes, indicating the formation of Cs_4PbCl_6 phase, were also observed. At last, we performed DFT and room temperature molecular dynamics calculations to investigate the structural change and diffusion-driven optical degradation. As a result, this work presents a comprehensive view on the doping process, covering both the pre- and post-doping conditions.

Materials: Cesium bromide (CsBr, 99.9%, Sigma-Aldrich), lead(II) bromide ($PbBr_2$, $\geq$98%, Sigma-Aldrich), manganese(II) chloride tetrahydrate ($MnCl_2 \cdot 4H_2O \geq 98\%$, Sigma-Aldrich), oleic acid (OA, 90%, Alfa Aesar), oleylamine (OAm, 90%, Sigma-Aldrich), dimethylformamide (DMF, $\geq$99.9%, Tekkim), hexane ($\geq$98%, Sigma-Aldrich), and toluene ($\geq$99%, Merck) were purchased and used as received without any further purification.

Characterization: The diffraction profiles of the Cesium perovskites were recorded with an X-ray diffractometer (XRD, X- Pert Pro, Philips, Eindhoven, the Netherlands). Emission spectra was determined by USB2000+ Spectrometer (Ocean Optics Inc., Dunedin, FL, USA) via a premium fiber cable. Raman (Horiba Xplora Plus) was used to determine fingerprint Raman-active vibrations of Cs-perovskite structures.

Density functional theory-based calculations were performed using the projector augmented wave (PAW) (Kresse and Joubert, 1999; Blöchl, 1994) potentials as implemented in VASP.(Kresse and Hafner, 1993a; Kresse and Furthmüller, 1996) The local density approximation (LDA) (Perdew and Zunger, 1981) was used to describe the ex-

change and correlation potential.(Ceperley and Alder, 1980) Bader technique was used to determine the charge transfer between the atoms.(Henkelman *et al.*, 2006)

A plane-wave basis set with kinetic energy cutoff of 500 eV was used for all the calculations. The total energy difference between the sequential steps in the iterations was taken to be 10^{-5} eV as the convergence criterion. The total force in the unitcell was reduced to a value less than 10^{-4} eV/Å. Γ-centered k-point meshes of $3 \times 3 \times 3$ and $3 \times 3 \times 1$ were used for bulk and surface relaxations, respectively. For Pb- and Cs-terminated surfaces, vacuum spaces of 10 Å was incorporated to avoid interaction with neighboring surfaces. Gaussian smearing of 0.1 eV was used for electronic density of states calculations. Spin-polarized calculations were performed in all cases. The cohesive energy per atom was calculated using the formula

$$E_{Coh} = \big[\sum_i n_{atom(i)} E_{atom(i)} - E_{system}\big]/n_{total} \tag{5.1}$$

where $E_{atom(i)}$ is isolated single atom energies for i^{th} atom, while i stands for the number of all atoms for the same species, n_{total} represents the total number of atoms, and $n_{atom(i)}$ shows the numbers of same kind of atoms in the unit cell, respectively.

5.1. Mn Doping-driven Structural Transition From Cs_4PbBr_6 to $CsPbCl_3$ Phase

Among those possible MnX_2 (X: Cl^-, Br^-, and I^-) precursors, $MnCl_2$ was already reported as to be the one that favors the Mn incorporation most since the bond dissociation energy of the Mn-Cl is closer to the one of Pb-Cl compared the other possible Mn-X precursors and their corresponding Pb-X bonds.(Liu *et al.*, 2016) To achieve doping, $MnCl_2$ was used during the synthesis of cesium lead preovskite crystals, and it was found that its usage leads to significant modification in its structural, vibrational and electronic properties (Fig. 5.1). While the structural characteristics of the crystals are monitored by XRD and Raman spectroscopy, their electronic and optical properties are characterized via experimentally observed PL spectra and theoretically calculated band dispersions.

Fig. 5.1 (a) shows the reflection signals of both undoped and Mn-doped samples collected from X-ray diffraction. Apparently, diffraction pattern represented with green line shows that Cs_4PbBr_6 phase forms first when Cs^+ and Pb^{2+} source employed solely. (Saidaminov *et al.*, 2016) Besides, as reported before,(Saidaminov *et al.*, 2016) in addition

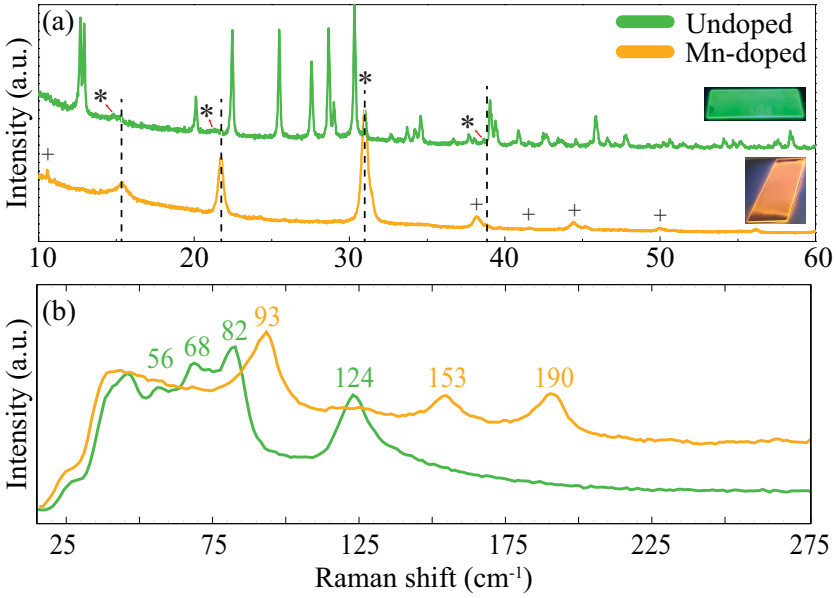

Figure 5.1. (a) X-ray diffraction and (b) Raman spectra of the undoped and Mn-doped perovskite crystals.

to Cs_4PbBr_6 there are also weak signals detected from small $CsPbBr_3$ crystals marked with *. However, Mn-doped perovskite structure that shows orange color under UV light has sharp signals at 2θ: 15°, 22°, 31°, and 38° (black dashed lines). The broadening of XRD reflections may result from the size of the coherently scattering domains, their size (referred as crystallite size or coherence length) can be estimated by the Scherrer formula

$$\textit{Crystallite Size} = K\lambda/\beta_{1/2}\cos\theta \tag{5.2}$$

where K is a form factor approximately equal to unity, lambda is the radiation wavelength (0.154 nm for Cu Kα radiation), and $\beta_{1/2}$ is the full width at half maximum (FWHM) of the reflection on the 2θ scale in radians. When 31° (2θ) is considered as the main reflection, the coherence length fall into the level of 15 nm applying the Scherrer formula. These intense XRD reflections not only indicate the formation of high crystalline Mn-doped perovskite material but also reveal the significant modification in crystal symmetry and structural transformation. Apparently, the XRD signals of the Mn-doped structure perfectly match with the tetragonal phase of $CsPbCl_3$ represented with black dashed line (JCPDS 18-0366). Therefore, during the manganese doping process that is done by using $MnCl_2$ molecules, Br-Cl halide exchange reaction also takes place. It is also

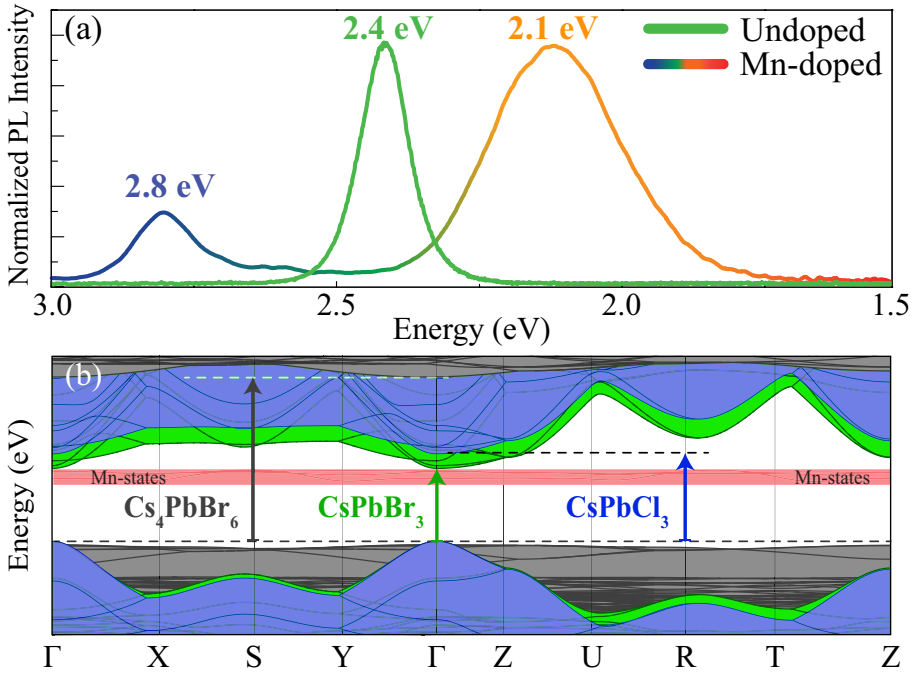

Figure 5.2. (a) PL spectra and (b) electronic band dispersion of undoped and Mn-doped samples.

seen that following the Br-Cl exchange weak signals that belong to the $CsPbBr_3$ become quite intense in the well-chlorinated crystal structure and Mn-doped sample contains no Cs_4PbBr_6 signals. On the other hand, signals marked with + correspond to excessive Mn ions that resulted trace amount of α-MnO_2 (JCPDS 44-0141) along the sample. Therefore, it is clear from XRD spectra that adding $MnCl_2$/DMF solution simultaneously with the Cs^+ and Pb^{2+} ions source into toluene leads to a phase transformation from Cs_4PbBr_6 to $CsPbCl_3$.

For monitoring how the vibrational characteristics of the crystal evolve during the doping procedure time-dependent room temperature Raman measurement was carried out using 785 nm laser excitation. As shown in Fig. 5.1 (b), Raman peaks at 56, 68, 82 and 124 cm^{-1} were obtained from the undoped sample indicating the formation of Cs_4PbBr_6 phase. On the other hand, the Raman spectrum of the Mn-doped sample indicates that the peak at 124 cm^{-1} that originate from the Pb-Br phonon modes in the $[PbBr_6]^-$ octahedron (Yin *et al.*, 2017) vanishes, however additional Raman shifts at 93, 153, and 190 cm^{-1} appear. Among these, while the peak at 93 cm^{-1} corresponds to the longitudinal optic (LO) mode of $CsPbCl_3$ crystal,(Carabatos-Nédelec *et al.*, 2003) the modes at 153 and 190

cm^{-1} stem from the Mn atoms. As a result, Raman spectra also verifies that using $MnCl_2$ together with Cs^+ and Pb^{2+} ions source during the synthesis significantly modifies the structure of resulting cesium lead perovskite phase.

To get insight of how Mn ions interact with the perovskite crystal nuclei during the doping process, the surface of the crystal needs to be examined at the molecular level due to ligands attached to the surface. In this sense, using the estimated crystallite size from the Scherrer formula and the amount of OA and OAm added into the system at the very beginning of the reaction, one can estimate the number of surfactant molecules grafted to the surface of the particles. Assuming a cubic particle having 15 nm length for each side (calculated by Scherrer formula above), it was found that surfactants were used in excess so that there can be compact packing of the surfactant molecules grafted to the surface of the perovskite crystals. The excess amount of molecules may remain in reaction solution mixture and/or adsorbed to the crystal surface as aggregates of second layer.

Moreover, how the optical properties of the perovskite are modified by Mn dopants is also investigated by PL spectroscopy. As shown in Fig. 5.1 (a), there is a single narrow emission peak at 2.4 eV for the undoped structure. In this sense, emission at 2.4 eV originates from the $CsPbBr_3$ domains (their presence was already verified in Fig. 5.1 (a)).(Akkerman *et al.*, 2017) However, as shown in Fig. 5.1 (a), two prominent peaks observed in the PL spectrum after the Mn doping procedure.

The ground state electronic structures are also investigated by performing density functional theory calculations. First, cohesive energy calculations indicated that $CsPbBr_3$ and $CsPbCl_3$ structures have the cohesive energy of 3.37 and 3.67 eV/atom and therefore, as long as there is a Cl-rich environment, the formation of chlorine-exchanged domains is energetically more favorable. The calculated electronic band structure of $CsPbCl_3$, $CsPbBr_3$, and Mn-doped $CsPbCl_3$ are shown in Fig. 5.1 (b). It is seen that while the halide exchange in $CsPbX_3$ leads to ignorable modification in the electronic band dispersion (band edges of both crystals lie at Γ point), $CsPbCl_3$ structure has wider bandgap than that of $CsPbBr_3$. Thereby, DFT calculations on the electronic structure, shown in Fig. 5.1 (b), showed that (i) the emission at 2.8 eV (443 nm) is due to the $CsPbCl_3$ phase which has a direct bandgap at the Γ high symmetry point and (ii) the presence of the Mn dopants leads to midgap states at the vicinity of 2.1 eV (589 nm).

5.2. Optical Stability of Mn-doped $CsPbCl_3$

To investigate the optical stability of Mn-doped $CsPbCl_3$, its emission was tracked in time. As shown in Fig 5.2 (a) Mn-doped $CsPbCl_3$ casted on the glass slide emits orange color under UV illumination (254 nm). It is seen from the photograph of UV illuminated sample that the emission of Mn-doped structure rapidly changes from orange to bluish color and after 195 hours under ambient conditions, perovskite completely turned into blue. To verify color change in time, PL spectrum of the orange perovskite crystal is

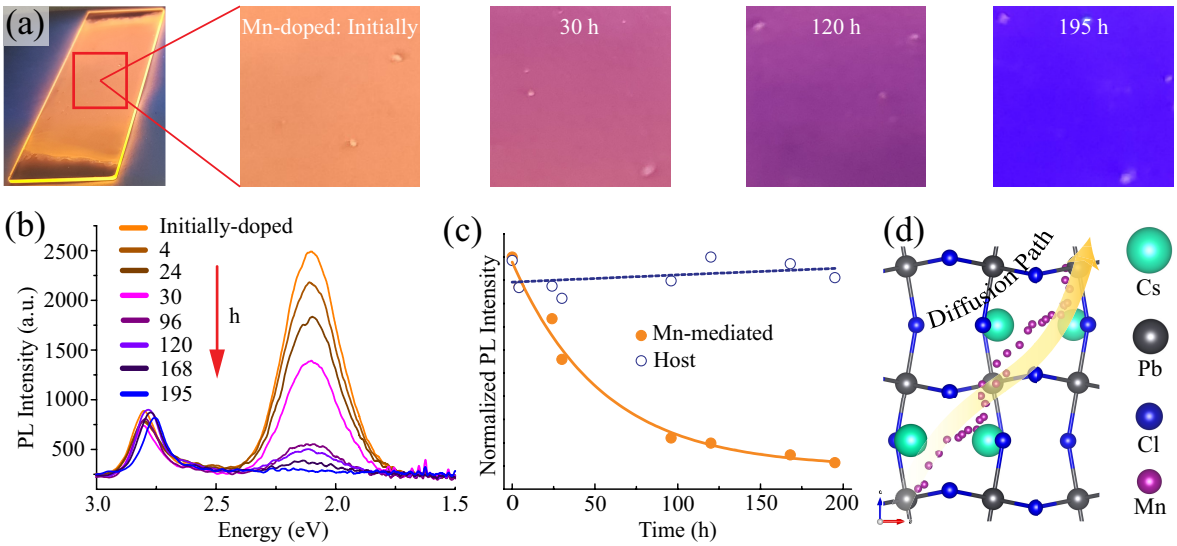

Figure 5.3. (a) The color change of the Mn-doped $CsPbCl_3$ perovskite under UV illumination (254 nm) tracked photographically in time. Photographs, from left to right, represent the Mn-doped $CsPbCl_3$ perovskite from its initial moment of casting (Mn-doped: Initially) to 195 hours later under ambient conditions. (b) and (c) present the change of related PL spectrum and PL intensity of Mn-doped $CsPbCl_3$ perovskite under UV illumination (254 nm) in time, respectively.

registered at various times as presented in Fig. 5.2. It is seen that while the intensity of the dopant-originated emission at 2.1 eV decreases rapidly, the emission of the host crystal $CsPbCl_3$ at 2.8 eV remains almost the same. Finally, the emission at 2.1 eV, that leads to the orange colouring of the structure, completely disappears after 195 hours. Here the rapid decrease in the dopant-induced emission over time is a kind of self purification process that takes place via removal of dopant atoms from the crystal lattice through the surface by diffusion.(Erwin *et al.*, 2005; Dalpian and Chelikowsky, 2006; Bryan and

Gamelin, 2005)

Moreover, the rate of change in the Mn-induced emission is shown in Fig. 5.2 (c), indicating that the observed data well-fits to the exponential decay equation $y - y_0 = Ae^{-t/c}$, where $y_0 = 0.094$, $A = 0.884$, and $c = 54.219$. Apparently, the exponential decrease of the peak stem from the diffusion of Mn atoms from lattice to surface. At this point, for further theoretical examination of the possibility of diffusion of Mn atoms in the $CsPbCl_3$ crystal structure, *ab initio* molecular dynamics (MD) calculations were also performed. Constant temperature MD simulations for 10 ps duration time, as shown in Fig. 5.2 (d), reveal that while the crystal structure remains stable at room temperature, Mn atoms can easily diffuse in the lattice sites by passing from the vicinity of Cs and Pb sites.

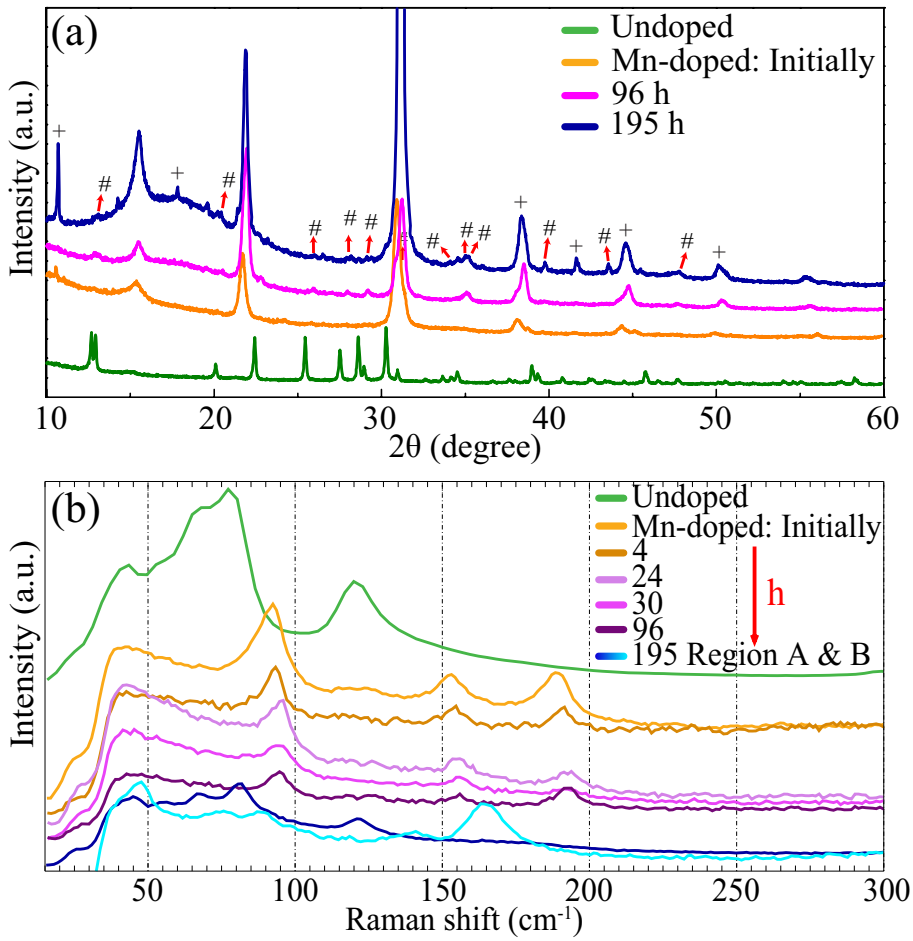

Figure 5.4. The structural change of the Mn-doped $CsPbCl_3$ perovskite was tracked in time by collecting (a) crystallographic information via X-ray diffraction pattern, and (b) vibrational modes via Raman scattering modes.

Modification in the crystal structure triggered by the diffusion of Mn atoms is also investigated by X-ray diffraction and Raman spectroscopy measurements at various times after casting the crystal dispersion from hexane. As shown in Fig. 5.4 (a), additional reflection signals became visible at first 96 hours indicating structural modification. The other XRD signals marked with #, clearly indicate the re-formation of Cs_4PbX_6 (where X is Br or Cl) phase after Mn segregation. It is also seen that XRD spectrum at 96 hours includes some slight blue-shifted 2θ values that resemble the undoped Cs_4PbBr_6 phase. However, the shift in signals is simply due to the Br-Cl exchange, that takes place during the addition of $MnCl_2$.

At the end of 195 hours, an obvious broad background signal appears between 12-20°. This feature is called as amorphous halo originating from organic materials. The occurrence of this signal after a long time duration may suggest the detachment and segregation of OA and OAm. Moreover, the number of XRD signals originate from the Cs_4PbCl_6 domains increases. On the other hand, intensity of the α-MnO_2 characteristic signals (marked with +) increases in time. This increase can be explained by the growing population of MnO_2 at the crystal surface. It can be concluded that Mn-doped $CsPbCl_3$ crystals change its phase from Mn doped tetragonal phase $CsPbCl_3$ to Cs_4PbCl_6 during the Mn diffusion process.

Time-dependent room temperature Raman measurement is also given in Fig. 5.4 (b). The prominent modes of Mn-doped sample at 92, 152 and 190 cm^{-1} appear upon the doping by Mn atoms. Mn-induced vibrational modes of the crystal, 152 and 190 cm^{-1}, were observed to vanish in time. After 195 hours later, two different regions were observed. In region A, which is presented with navy blue line, Raman shift became almost identical with undoped one but few wavenumber shifted due to halide exchange. In region B, presented with turquoise line, a prominent peak at 162 cm^{-1} which is the indication of MnO_2.(Gao *et al.*, 2009)

As a result, it is observed experimentally that there is a clear optical degradation of the Mn-induced emission at 2.1 eV in time implying the diffusion of Mn atoms. Meanwhile, during the diffusion process, additional signals began to appear in both XRD and Raman measurements. Therefore, it can be concluded that the diffusion of Mn atoms leads to both optical and structural instabilities.

5.3. Diffusion Dynamics at the Surface

Diffusive motion of Mn atoms towards surface and the transition from $CsPbCl_3$ phase to Cs_4PbCl_6 were also investigated through first principle calculations. As shown in Fig. 5.5, two possible surface types, namely Cs- and Pb-terminated surfaces, were considered to investigate absorption energy of Mn atom. The calculations reveal that binding energy of Mn atom on the Cs- and Pb-terminated surfaces of $CsPbCl_3$ are 4.74 and 5.19 eV, respectively. Bader charge analysis indicates that Mn atom donates $1.2e$ and $1.0e$ for Cs- and Pb-terminated surfaces. Therefore, considering the binding energy of Mn atoms inside the crystal structure, which is 1.24 eV at the most favorable lattice site, diffusive motion towards the surface is found to be inevitable.

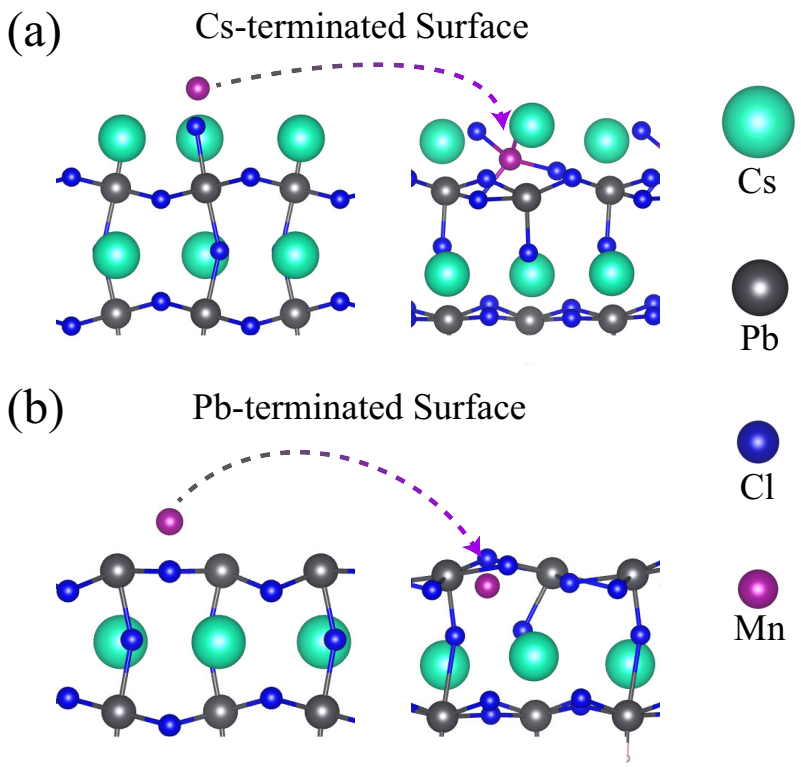

Figure 5.5. Calculated adsorption sites on the Cs- and Pb-terminated surfaces of $CsPbCl_3$.

On the other hand, absorption energy of Mn atoms on the Cs- and Pb-terminated surfaces are significantly higher than the adsorption of OA and OAm, which are 698 and 463 meV for the Cs-terminated, and 221 and 874 meV for the Pb-terminated surface,

respectively.(Akbali *et al.*, 2018) Therefore, surface of the perovskite crystals, including either Cs- or Pb-terminated surface, prefer to bind Mn atoms by leaving the ligands. In such a case, expelled ligands then can bind to $CsPbCl_3$ surfaces that do not contain any Mn atoms and lead to ligand-mediated phase transformation from $CsPbCl_3$ to Cs_4PbCl_6. Among these ligands (OA and OAm), it was already reported that OAm by itself can trigger this process.(Liu *et al.*, 2017)

Note that during the doping process, only some limited amount of the Mn ($\leq 37\%$) can be doped into the $CsPbCl_3$ lattice as substitutional defects since 37% doping ratio was reported as achieved maximally by using the synthesis method followed in this study.(Zhu *et al.*, 2017) In any case, either the crystals were achieved to be Mn-doped ($\leq 37\%$) or not doped (remain as neat host $CsPbCl_3$ crystals $\geq 63\%$), the whole sample presents a clear $CsPbCl_3$ characteristic signals together as given in Fig. 5.1 (a). Compared to Mn-doped $CsPbCl_3$ crystals, neat host crystals show a more stable optical and structural response in time because both the host emission observed at 2.8 eV (Fig. 5.2 (c)), and characteristic signals of the $CsPbCl_3$ remain almost the same in time.

Neat $CsPbCl_3$ host crystals (not doped ones with ratio of $\geq 63\%$) were observed to be stable as optically and structurally in time. On the other hand, Mn-doped perovskite crystals ($\leq 37\%$ showed both optical and structural instabilities. The reason of what drives these instabilities were investigated through theoretical calculations and it was found that Mn ions diffuse towards the crystal surface resulting in both optical and structural instabilities.

In this study, influence of Mn dopants on the structural, vibrational and optical properties of Cs-perovskite crystals was investigated by performing experimental characterization tools and state-of-the-art first-principles calculations. It was found that the presence of Mn ions leads to a structural transition from Cs_4PbBr_6 to $CsPbCl_3$ phase and opens an additional emission channel at ≈ 2.1 eV. On the other hand, PL intensity of the dopant-induced emission was found to decay exponentially in time. DFT calculations revealed that the additional PL peak simply stems from the Mn-originated midgap states and the decaying behavior of emission is a consequence of diffusive motion of Mn dopants towards the crystal surface. Time-dependent XRD and Raman measurements also revealed that formation of MnO_2 at the surface and domains of Cs_4PbCl_6 phase in the $CsPbCl_3$ host crystal also take place. As a result, this study offers a detailed understanding for the mechanisms governing the doping structure of the perovskite crystals, including the effect of dopants on both structural and optical properties of perovskite crystals.

CHAPTER 6

CONCLUSIONS

Realization of graphene is the milestone of the family of two-dimensional (2D) materials. Due to the strong sp^2 hybridization of carbon atoms and its single-atom thickness, graphene has exceptional properties such as advanced mechanical strength, high carrier mobility and heat conduction properties. Following the isolation of single layer graphene, layered transition metal dichalcogenides (TMDs) have gained considerable interest due to extraordinary physical properties. Among family of TMDs, MoS_2 has been widely studied due to its size-dependent optical and electronic properties. In addition to TMDs, as a member of colloidal semiconductor nanocrystal (NC) family, cesium lead halide perovskites in the form of $CsPbX_3$ (X: Cl^-, Br^-, I^-) offer outstanding optical properties such as high photoluminescence quantum yield (PLQY) and defect-tolerance, and wavelength tunability. In a short period of time, perovskite solar cells have become able to improve the conversion efficiency from 3.81% to almost 20%. However, diffusion and degradation mechanisms of these crystals are still an open question in literature. Therefore, in this thesis, diffusion and degradation characteristics of perovskites and MoS_2 were investigated by means of first-principles calculations based on DFT and Raman spectroscopy measurements. Raman spectroscopy is a powerful tools to measure Raman active modes of the crystals. In addition, DFT-based calculations were performed to investigate diffusion and degradation characteristics of the materials.

Due to being non-contact and non-destructive measurement technique, Raman spectroscopy is one of the most practical tool to provide information on vibrational properties of crystals. Raman spectroscopy result can give information about fundamental properties of materials such as stress-strain in the crystal, doping, and defects. Hence, in this thesis, Raman spectroscopy was used to get information about doping and degradation of crystals. In addition to experimental tool, phonon band dispersion of the crystals were computed with density functional theory (DFT) based first principle calculations. Phonon calculations are also important to determine dynamical stability and Raman-active vibrational modes of the materials.

First of all, coating performance of the MoS_2 against nitrogenation were investigated by performing density functional theory-based calculations.(Akbali *et al.*, 2017) It was found that lateral diffusion of N atom is possible on MoS_2 surface by following the

path through Molybdenum (Mo) and hollow (H) sites. However, vertical diffusion of N atom is not possible at room temperature, due to the fact that MoS_2 shows high energy barrier against the atom. In addition, Raman spectroscopy results indicated that the region which is not covered with MoS_2 emerged D+D′ peak (presence of nitrogenated graphene). Somehow, D+D′ peak was not measured on MoS_2 coated region. Therefore, MoS_2 can serve as an effective nanocoating material for selective nitrogenation of graphene.

Secondly, degradation mechanism of $CsPbBr_3$ perovskite was investigated via theoretical calculations and experimental tools including Raman spectroscopy.(Akbali *et al.*, 2018) It was found that $CsPbBr_3$ nanowire is degraded by water molecules. It was revealed that water molecules detach the surface ligands from the surface of the nanowire and cause bundle formation. Afterwards, further water interaction causes complete degradation to its constituents. Results were verified by the first-principles calculations and Raman spectroscopy results.

Thirdly, diffusion characteristics of Mn-doped Cs-perovskite were investigated by performing experimental characterization tools and state-of-the-art first-principles calculations.(Guner *et al.*, 2018) It was found that the presence of Mn ions leads to a structural transition from Cs_4PbBr_6 to $CsPbBr_3$. DFT calculations revealed that Mn-doping causes midgap states and PL measurement verified the finding. Also, Room temperature molecular dynamics calculations indicated that Mn atoms in the crystal can easily diffuse in the lattice sites by passing from the vicinity of Cs and Pb sites. Raman spectroscopy results showed that presence of MnO_2 peaks is indication of diffused Mn atoms towards the surface. Therefore, it can be concluded that the diffusion of Mn atoms leads to both optical and structural instabilities.

To summarize, understanding diffusion and degradation characteristics of the crystals via theoretical calculations and Raman measurements in atomic scale is important. In this respect, as we showed in our recent above mentioned works, first principles calculations are essential for elucidating physical insights of the observation. Furthermore, Raman spectroscopy measurement is a fast, reliable, and nondestructive characterization tool to measure Raman-active vibrational modes of the crystals. We believe that our findings in this thesis will enlighten the degradation and diffusion characteristics of the novel 2D materials and perovskite crystals.

REFERENCES

Acharya, S., S. Sarkar, and N. Pradhan (2013). Material diffusion and doping of mn in wurtzite znse nanorods. *The Journal of Physical Chemistry C 117*(11), 6006–6012.

Akada, K., T.-o. Terasawa, G. Imamura, S. Obata, and K. Saiki (2014). Control of work function of graphene by plasma assisted nitrogen doping. *Applied Physics Letters 104*(13), 131602.

Akbali, B., G. Topcu, T. Guner, M. Ozcan, M. M. Demir, and H. Sahin (2018). Cspbbr 3 perovskites: Theoretical and experimental investigation on water-assisted transition from nanowire formation to degradation. *Physical Review Materials 2*(3), 034601.

Akbali, B., A. Yanilmaz, A. Tomak, S. Tongay, C. Çelebi, and H. Sahin (2017). Few-layer mos2 as nitrogen protective barrier. *Nanotechnology 28*(41), 415706.

Akkerman, Q. A., V. DâInnocenzo, S. Accornero, A. Scarpellini, A. Petrozza, M. Prato, and L. Manna (2015). Tuning the optical properties of cesium lead halide perovskite nanocrystals by anion exchange reactions. *Journal of the American Chemical Society 137*(32), 10276–10281.

Akkerman, Q. A., S. G. Motti, A. R. Srimath Kandada, E. Mosconi, V. DâInnocenzo, G. Bertoni, S. Marras, B. A. Kamino, L. Miranda, F. De Angelis, *et al.* (2016). Solution synthesis approach to colloidal cesium lead halide perovskite nanoplatelets with monolayer-level thickness control. *Journal of the American Chemical Society 138*(3), 1010–1016.

Akkerman, Q. A., S. Park, E. Radicchi, F. Nunzi, E. Mosconi, F. De Angelis, R. Brescia, P. Rastogi, M. Prato, and L. Manna (2017). Nearly monodisperse insulator cs4pbx6 (x= cl, br, i) nanocrystals, their mixed halide compositions, and their transformation into cspbx3 nanocrystals. *Nano letters 17*(3), 1924–1930.

Alfè, D. (2009). Phon: A program to calculate phonons using the small displacement method. *Computer Physics Communications 180*(12), 2622–2633.

Ali, M. N., J. Xiong, S. Flynn, J. Tao, Q. D. Gibson, L. M. Schoop, T. Liang, N. Haldolaarachchige, M. Hirschberger, N. Ong, *et al.* (2014). Large, non-saturating magnetoresistance in wte 2. *Nature 514*(7521), 205.

Amgar, D., A. Stern, D. Rotem, D. Porath, and L. Etgar (2017). Tunable length and optical properties of cspbx3 (x= cl, br, i) nanowires with a few unit cells. *Nano letters 17*(2), 1007–1013.

Azcatl, A., X. Qin, A. Prakash, C. Zhang, L. Cheng, Q. Wang, N. Lu, M. J. Kim,

J. Kim, K. Cho, *et al.* (2016). Covalent nitrogen doping and compressive strain in mos2 by remote n2 plasma exposure. *Nano letters 16*(9), 5437–5443.

Azpiroz, J. M., E. Mosconi, J. Bisquert, and F. De Angelis (2015). Defect migration in methylammonium lead iodide and its role in perovskite solar cell operation. *Energy & Environmental Science 8*(7), 2118–2127.

Bai, S., Z. Yuan, and F. Gao (2016). Colloidal metal halide perovskite nanocrystals: synthesis, characterization, and applications. *Journal of Materials Chemistry C 4*(18), 3898–3904.

Balandin, A. A., S. Ghosh, W. Bao, I. Calizo, D. Teweldebrhan, F. Miao, and C. N. Lau (2008). Superior thermal conductivity of single-layer graphene. *Nano letters 8*(3), 902–907.

Balendhran, S., J. Z. Ou, M. Bhaskaran, S. Sriram, S. Ippolito, Z. Vasic, E. Kats, S. Bhargava, S. Zhuiykov, and K. Kalantar-Zadeh (2012). Atomically thin layers of mos 2 via a two step thermal evaporation–exfoliation method. *Nanoscale 4*(2), 461–466.

Bao, J. F., N. Kishi, and T. Soga (2014). Synthesis of nitrogen-doped graphene by the thermal chemical vapor deposition method from a single liquid precursor. *Materials Letters 117*, 199–203.

Beal, R. E., D. J. Slotcavage, T. Leijtens, A. R. Bowring, R. A. Belisle, W. H. Nguyen, G. F. Burkhard, E. T. Hoke, and M. D. McGehee (2016). Cesium lead halide perovskites with improved stability for tandem solar cells. *The journal of physical chemistry letters 7*(5), 746–751.

Beams, R., L. G. Cançado, and L. Novotny (2015). Raman characterization of defects and dopants in graphene. *Journal of Physics: Condensed Matter 27*(8), 083002.

Bekenstein, Y., B. A. Koscher, S. W. Eaton, P. Yang, and A. P. Alivisatos (2015). Highly luminescent colloidal nanoplates of perovskite cesium lead halide and their oriented assemblies. *Journal of the American Chemical Society 137*(51), 16008–16011.

Berger, C., Z. Song, X. Li, X. Wu, N. Brown, C. Naud, D. Mayou, T. Li, J. Hass, A. N. Marchenkov, *et al.* (2006). Electronic confinement and coherence in patterned epitaxial graphene. *Science 312*(5777), 1191–1196.

Bhaumik, S., S. A. Veldhuis, Y. F. Ng, M. Li, S. K. Muduli, T. C. Sum, B. Damodaran, S. Mhaisalkar, and N. Mathews (2016). Highly stable, luminescent core–shell type methylammonium–octylammonium lead bromide layered perovskite nanoparticles. *Chemical Communications 52*(44), 7118–7121.

Blöchl, P. (1994). Pe blöchl, phys. rev. b 50, 17953 (1994). *Phys. Rev. B 50*, 17953.

Bolotin, K. I., K. Sikes, Z. Jiang, M. Klima, G. Fudenberg, J. Hone, P. Kim, and H. Stormer (2008). Ultrahigh electron mobility in suspended graphene. *Solid State Communications 146*(9-10), 351–355.

Brennan, M. C., J. Zinna, and M. Kuno (2017). Existence of a size-dependent stokes shift in cspbbr3 perovskite nanocrystals. *ACS Energy Letters 2*(7), 1487–1488.

Bryan, J. D. and D. R. Gamelin (2005). Doped semiconductor nanocrystals: synthesis, characterization, physical properties, and applications. *Prog. Inorg. Chem 54*, 47–126.

Byun, J., H. Cho, C. Wolf, M. Jang, A. Sadhanala, R. H. Friend, H. Yang, and T.-W. Lee (2016). Efficient visible quasi-2d perovskite light-emitting diodes. *Advanced Materials 28*(34), 7515–7520.

Calistru, D. M., L. Mihut, S. Lefrant, and I. Baltog (1997). Identification of the symmetry of phonon modes in cspbcl 3 in phase iv by raman and resonance-raman scattering. *Journal of applied physics 82*(11), 5391–5395.

Carabatos-Nédelec, C., M. Oussaid, and K. Nitsch (2003). Raman scattering investigation of cesium plumbochloride, cspbcl3, phase transitions. *Journal of Raman Spectroscopy 34*(5), 388–393.

Ceperley, D. M. and B. Alder (1980). Ground state of the electron gas by a stochastic method. *Physical Review Letters 45*(7), 566.

Chen, M., Y. Zou, L. Wu, Q. Pan, D. Yang, H. Hu, Y. Tan, Q. Zhong, Y. Xu, H. Liu, *et al.* (2017). Solvothermal synthesis of high-quality all-inorganic cesium lead halide perovskite nanocrystals: From nanocube to ultrathin nanowire. *Advanced Functional Materials 27*(23).

Chen, S., L. Brown, M. Levendorf, W. Cai, S.-Y. Ju, J. Edgeworth, X. Li, C. W. Magnuson, A. Velamakanni, R. D. Piner, *et al.* (2011). Oxidation resistance of graphene-coated cu and cu/ni alloy. *ACS nano 5*(2), 1321–1327.

Cho, H., S.-H. Jeong, M.-H. Park, Y.-H. Kim, C. Wolf, C.-L. Lee, J. H. Heo, A. Sadhanala, N. Myoung, S. Yoo, *et al.* (2015). Overcoming the electroluminescence efficiency limitations of perovskite light-emitting diodes. *Science 350*(6265), 1222–1225.

Coleman, J. N., M. Lotya, A. OâNeill, S. D. Bergin, P. J. King, U. Khan, K. Young, A. Gaucher, S. De, R. J. Smith, *et al.* (2011). Two-dimensional nanosheets produced by liquid exfoliation of layered materials. *Science 331*(6017), 568–571.

Cong, C., J. Shang, X. Wu, B. Cao, N. Peimyoo, C. Qiu, L. Sun, and T. Yu (2014). Synthesis and optical properties of large-area single-crystalline 2d semiconductor ws2 monolayer from chemical vapor deposition. *Advanced Optical Materials 2*(2), 131–136.

Cottingham, P. and R. L. Brutchey (2016). On the crystal structure of colloidally prepared cspbbr 3 quantum dots. *Chemical Communications 52*(30), 5246–5249.

Dalpian, G. M. and J. R. Chelikowsky (2006). Self-purification in semiconductor nanocrystals. *Physical review letters 96*(22), 226802.

Das, S., H.-Y. Chen, A. V. Penumatcha, and J. Appenzeller (2012). High performance multilayer mos2 transistors with scandium contacts. *Nano letters 13*(1), 100–105.

Donnet, C., J. Martin, T. Le Mogne, and M. Belin (1996). Super-low friction of mos2 coatings in various environments. *Tribology International 29*(2), 123–128.

Eaton, S. W., M. Lai, N. A. Gibson, A. B. Wong, L. Dou, J. Ma, L.-W. Wang, S. R. Leone, and P. Yang (2016). Lasing in robust cesium lead halide perovskite nanowires. *Proceedings of the National Academy of Sciences 113*(8), 1993–1998.

Eda, G., H. Yamaguchi, D. Voiry, T. Fujita, M. Chen, and M. Chhowalla (2011). Photoluminescence from chemically exfoliated mos2. *Nano letters 11*(12), 5111–5116.

Erickson, C. S., L. R. Bradshaw, S. McDowall, J. D. Gilbertson, D. R. Gamelin, and D. L. Patrick (2014). Zero-reabsorption doped-nanocrystal luminescent solar concentrators. *ACS nano 8*(4), 3461–3467.

Erwin, S. C., L. Zu, M. I. Haftel, A. L. Efros, T. A. Kennedy, and D. J. Norris (2005). Doping semiconductor nanocrystals. *Nature 436*(7047), 91.

Fainblat, R., C. J. Barrows, E. Hopmann, S. Siebeneicher, V. A. Vlaskin, D. R. Gamelin, and G. Bacher (2016). Giant excitonic exchange splittings at zero field in single colloidal cdse quantum dots doped with individual mn2+ impurities. *Nano letters 16*(10), 6371–6377.

Fang, H., S. Chuang, T. C. Chang, K. Takei, T. Takahashi, and A. Javey (2012). High-performance single layered wse2 p-fets with chemically doped contacts. *Nano letters 12*(7), 3788–3792.

Ferrari, A. C., J. Meyer, V. Scardaci, C. Casiraghi, M. Lazzeri, F. Mauri, S. Piscanec, D. Jiang, K. Novoselov, S. Roth, *et al.* (2006). Raman spectrum of graphene and graphene layers. *Physical review letters 97*(18), 187401.

Frey, G. L., R. Tenne, M. J. Matthews, M. Dresselhaus, and G. Dresselhaus (1999). Raman and resonance raman investigation of mos 2 nanoparticles. *Physical Review*

B 60(4), 2883.

Gao, T., H. Fjellvåg, and P. Norby (2009). A comparison study on raman scattering properties of α-and β-mno2. *Analytica chimica acta 648*(2), 235–239.

Geng, W., L. Zhang, Y.-N. Zhang, W.-M. Lau, and L.-M. Liu (2014). First-principles study of lead iodide perovskite tetragonal and orthorhombic phases for photovoltaics. *The Journal of Physical Chemistry C 118*(34), 19565–19571.

Georgiou, T., R. Jalil, B. D. Belle, L. Britnell, R. V. Gorbachev, S. V. Morozov, Y.-J. Kim, A. Gholinia, S. J. Haigh, O. Makarovsky, *et al.* (2013). Vertical field-effect transistor based on graphene–ws 2 heterostructures for flexible and transparent electronics. *Nature nanotechnology 8*(2), 100.

Grimme, S. (2006). Semiempirical gga-type density functional constructed with a long-range dispersion correction. *Journal of computational chemistry 27*(15), 1787–1799.

Guner, T., B. Akbali, M. Ozcan, G. Topcu, M. M. Demir, and H. Sahin (2018). Monitoring the doping and diffusion characteristics of mn dopants in cesiumlead halide perovskites. *The Journal of Physical Chemistry C*.

Güner, T., G. Topçu, U. Savacı, A. Genç, S. Turan, E. Sari, and M. M. Demir (2018). Polarized emission from cspbbr3 nanowire embedded-electrospun pu fibers. *Nanotechnology 29*(13), 135202.

Guria, A. K., S. K. Dutta, S. D. Adhikari, and N. Pradhan (2017). Doping mn2+ in lead halide perovskite nanocrystals: Successes and challenges. *ACS Energy Letters 2*(5), 1014–1021.

Haruyama, J., K. Sodeyama, I. Hamada, L. Han, and Y. Tateyama (2017). First-principles study of electron injection and defects at the tio2/ch3nh3pbi3 interface of perovskite solar cells. *The journal of physical chemistry letters 8*(23), 5840–5847.

Haruyama, J., K. Sodeyama, L. Han, and Y. Tateyama (2015). First-principles study of ion diffusion in perovskite solar cell sensitizers. *Journal of the American Chemical Society 137*(32), 10048–10051.

He, X., Y. Qiu, and S. Yang (2017). Fully-inorganic trihalide perovskite nanocrystals: A new research frontier of optoelectronic materials. *Advanced Materials*.

Hedayat, S. M., J. Karimi-Sabet, and M. Shariaty-Niassar (2017). Evolution effects of the copper surface morphology on the nucleation density and growth of graphene domains at different growth pressures. *Applied Surface Science 399*, 542–550.

Hendra, P. J. and P. Stratton (1969). Laser-raman spectroscopy. *Chemical Re-*

views 69(3), 325–344.

Henkelman, G., A. Arnaldsson, and H. Jónsson (2006). A fast and robust algorithm for bader decomposition of charge density. *Computational Materials Science 36*(3), 354–360.

Hu, Q., Z. Li, Z. Tan, H. Song, C. Ge, G. Niu, J. Han, and J. Tang (2018). Rare earth ion-doped cspbbr3 nanocrystals. *Advanced Optical Materials 6*(2).

Huang, H., M. I. Bodnarchuk, S. V. Kershaw, M. V. Kovalenko, and A. L. Rogach (2017). Lead halide perovskite nanocrystals in the research spotlight: Stability and defect tolerance. *ACS energy letters 2*(9), 2071–2083.

Huang, H., B. Chen, Z. Wang, T. F. Hung, A. S. Susha, H. Zhong, and A. L. Rogach (2016). Water resistant cspbx 3 nanocrystals coated with polyhedral oligomeric silsesquioxane and their use as solid state luminophores in all-perovskite white light-emitting devices. *Chemical Science 7*(9), 5699–5703.

Im, J.-H., C.-R. Lee, J.-W. Lee, S.-W. Park, and N.-G. Park (2011). 6.5% efficient perovskite quantum-dot-sensitized solar cell. *Nanoscale 3*(10), 4088–4093.

Imran, M., F. Di Stasio, Z. Dang, C. Canale, A. H. Khan, J. Shamsi, R. Brescia, M. Prato, and L. Manna (2016). Colloidal synthesis of strongly fluorescent cspbbr3 nanowires with width tunable down to the quantum confinement regime. *Chemistry of Materials 28*(18), 6450–6454.

Iqbal, M., A. K. Singh, M. Iqbal, and J. Eom (2012). Raman fingerprint of doping due to metal adsorbates on graphene. *Journal of Physics: Condensed Matter 24*(33), 335301.

Iso, Y. and T. Isobe (2018). Synthesis, luminescent properties, and stabilities of cesium lead halide perovskite nanocrystals. *ECS Journal of Solid State Science and Technology 7*(1), R3040–R3045.

Isupova, L. and E. Sobolev (1968). Raman spectra of crystalline powders. *Journal of Structural Chemistry 9*(2), 263–265.

Iyikanat, F., E. Sari, and H. Sahin (2017). Thinning cspb 2 br 5 perovskite down to monolayers: Cs-dependent stability. *Physical Review B 96*(15), 155442.

Jafri, R. I., N. Rajalakshmi, and S. Ramaprabhu (2010). Nitrogen doped graphene nanoplatelets as catalyst support for oxygen reduction reaction in proton exchange membrane fuel cell. *Journal of Materials Chemistry 20*(34), 7114–7117.

Jeon, N. J., J. H. Noh, W. S. Yang, Y. C. Kim, S. Ryu, J. Seo, and S. I. Seok (2015). Compositional engineering of perovskite materials for high-performance

solar cells. *Nature 517*(7535), 476.

Jeong, H. M., J. W. Lee, W. H. Shin, Y. J. Choi, H. J. Shin, J. K. Kang, and J. W. Choi (2011). Nitrogen-doped graphene for high-performance ultracapacitors and the importance of nitrogen-doped sites at basal planes. *Nano letters 11*(6), 2472–2477.

Jung, D. H., C. Kang, M. Kim, H. Cheong, H. Lee, and J. S. Lee (2014). Effects of hydrogen partial pressure in the annealing process on graphene growth. *The Journal of Physical Chemistry C 118*(7), 3574–3580.

Kamat, P. V. (2011). Semiconductor nanocrystals: to dope or not to dope.

Kang, J. and L.-W. Wang (2017). High defect tolerance in lead halide perovskite cspbbr3. *The journal of physical chemistry letters 8*(2), 489–493.

Karan, N. S., S. Sarkar, D. D. Sarma, P. Kundu, N. Ravishankar, and N. Pradhan (2011). Thermally controlled cyclic insertion/ejection of dopant ions and reversible zinc blende/wurtzite phase changes in zns nanostructures. *Journal of the American Chemical Society 133*(6), 1666–1669.

Kawai, H., G. Giorgi, A. Marini, and K. Yamashita (2015). The mechanism of slow hot-hole cooling in lead-iodide perovskite: first-principles calculation on carrier lifetime from electron–phonon interaction. *Nano letters 15*(5), 3103–3108.

Keum, D. H., S. Cho, J. H. Kim, D.-H. Choe, H.-J. Sung, M. Kan, H. Kang, J.-Y. Hwang, S. W. Kim, H. Yang, *et al.* (2015). Bandgap opening in few-layered monoclinic mote 2. *Nature Physics 11*(6), 482.

Kim, J., S.-H. Lee, J. H. Lee, and K.-H. Hong (2014). The role of intrinsic defects in methylammonium lead iodide perovskite. *The journal of physical chemistry letters 5*(8), 1312–1317.

Kirkland, N., T. Schiller, N. Medhekar, and N. Birbilis (2012). Exploring graphene as a corrosion protection barrier. *Corrosion Science 56*, 1–4.

Kneipp, K., Y. Wang, H. Kneipp, L. T. Perelman, I. Itzkan, R. R. Dasari, and M. S. Feld (1997). Single molecule detection using surface-enhanced raman scattering (sers). *Physical review letters 78*(9), 1667.

Kohn, W. and L. J. Sham (1965). Self-consistent equations including exchange and correlation effects. *Physical review 140*(4A), A1133.

Kojima, A., K. Teshima, Y. Shirai, and T. Miyasaka (2009). Organometal halide perovskites as visible-light sensitizers for photovoltaic cells. *Journal of the American Chemical Society 131*(17), 6050–6051.

Kong, D., H. Wang, J. J. Cha, M. Pasta, K. J. Koski, J. Yao, and Y. Cui (2013). Synthesis of mos2 and mose2 films with vertically aligned layers. *Nano letters 13*(3), 1341–1347.

Kovalenko, M. V., L. Protesescu, and M. I. Bodnarchuk (2017). Properties and potential optoelectronic applications of lead halide perovskite nanocrystals. *Science 358*(6364), 745–750.

Kresse, G. and J. Furthmüller (1996). Efficient iterative schemes for ab initio total-energy calculations using a plane-wave basis set. *Physical review B 54*(16), 11169.

Kresse, G. and J. Hafner (1993a). Ab initio molecular dynamics for liquid metals. *Physical Review B 47*(1), 558.

Kresse, G. and J. Hafner (1993b). Numerical computations have been carried out by using vasp software phys rev. *B 47*, 558–61.

Kresse, G. and D. Joubert (1999). From ultrasoft pseudopotentials to the projector augmented-wave method. *Physical Review B 59*(3), 1758.

Kulbak, M., D. Cahen, and G. Hodes (2015). How important is the organic part of lead halide perovskite photovoltaic cells? efficient cspbbr3 cells. *The journal of physical chemistry letters 6*(13), 2452–2456.

Lee, C., H. Yan, L. E. Brus, T. F. Heinz, J. Hone, and S. Ryu (2010). Anomalous lattice vibrations of single-and few-layer mos2. *ACS nano 4*(5), 2695–2700.

Lee, K., H.-Y. Kim, M. Lotya, J. N. Coleman, G.-T. Kim, and G. S. Duesberg (2011). Electrical characteristics of molybdenum disulfide flakes produced by liquid exfoliation. *Advanced materials 23*(36), 4178–4182.

Leijtens, T., K. Bush, R. Cheacharoen, R. Beal, A. Bowring, and M. D. McGehee (2017). Towards enabling stable lead halide perovskite solar cells; interplay between structural, environmental, and thermal stability. *Journal of Materials Chemistry A 5*(23), 11483–11500.

Li, G., F. W. R. Rivarola, N. J. Davis, S. Bai, T. C. Jellicoe, F. de la Peña, S. Hou, C. Ducati, F. Gao, R. H. Friend, *et al.* (2016). Highly efficient perovskite nanocrystal light-emitting diodes enabled by a universal crosslinking method. *Advanced Materials 28*(18), 3528–3534.

Li, H., Z. Yin, Q. He, H. Li, X. Huang, G. Lu, D. W. H. Fam, A. I. Y. Tok, Q. Zhang, and H. Zhang (2012). Fabrication of single-and multilayer mos2 film-based field-effect transistors for sensing no at room temperature. *small 8*(1), 63–67.

Li, H., Q. Zhang, C. C. R. Yap, B. K. Tay, T. H. T. Edwin, A. Olivier, and D. Baillargeat

(2012). From bulk to monolayer mos2: evolution of raman scattering. *Advanced Functional Materials 22*(7), 1385–1390.

Li, J., L. Xu, T. Wang, J. Song, J. Chen, J. Xue, Y. Dong, B. Cai, Q. Shan, B. Han, *et al.* (2017). 50-fold eqe improvement up to 6.27% of solution-processed all-inorganic perovskite cspbbr3 qleds via surface ligand density control. *Advanced Materials 29*(5).

Li, L. H., J. Cervenka, K. Watanabe, T. Taniguchi, and Y. Chen (2014). Strong oxidation resistance of atomically thin boron nitride nanosheets. *Acs Nano 8*(2), 1457–1462.

Li, L. H., T. Xing, Y. Chen, and R. Jones (2014). Boron nitride nanosheets for metal protection. *Advanced materials interfaces 1*(8).

Li, X., F. Cao, D. Yu, J. Chen, Z. Sun, Y. Shen, Y. Zhu, L. Wang, Y. Wei, Y. Wu, *et al.* (2017). All inorganic halide perovskites nanosystem: synthesis, structural features, optical properties and optoelectronic applications. *Small 13*(9).

Li, Y., H. Wang, L. Xie, Y. Liang, G. Hong, and H. Dai (2011). Mos2 nanoparticles grown on graphene: an advanced catalyst for the hydrogen evolution reaction. *Journal of the American Chemical Society 133*(19), 7296–7299.

Li, Z.-J., E. Hofman, J. Li, A. H. Davis, C.-H. Tung, L.-Z. Wu, and W. Zheng (2018). Photoelectrochemically active and environmentally stable cspbbr3/tio2 core/shell nanocrystals. *Advanced Functional Materials 28*(1).

Lignos, I., S. Stavrakis, G. Nedelcu, L. Protesescu, A. J. deMello, and M. V. Kovalenko (2016). Synthesis of cesium lead halide perovskite nanocrystals in a droplet-based microfluidic platform: fast parametric space mapping. *Nano letters 16*(3), 1869–1877.

Lin, C. C., K. Y. Xu, D. Wang, and A. Meijerink (2017). Luminescent manganese-doped cspbcl 3 perovskite quantum dots. *Scientific Reports 7*, 45906.

Lin, Y.-M., C. Dimitrakopoulos, K. A. Jenkins, D. B. Farmer, H.-Y. Chiu, A. Grill, and P. Avouris (2010). 100-ghz transistors from wafer-scale epitaxial graphene. *Science 327*(5966), 662–662.

Liu, D. and T. L. Kelly (2014). Perovskite solar cells with a planar heterojunction structure prepared using room-temperature solution processing techniques. *Nature photonics 8*(2), 133.

Liu, M., G. Zhong, Y. Yin, J. Miao, K. Li, C. Wang, X. Xu, C. Shen, and H. Meng (2017). Aluminum-doped cesium lead bromide perovskite nanocrystals with stable blue photoluminescence used for display backlight. *Advanced Science 4*(11).

Liu, Q., X. Weijun, Z. Wu, J. Huo, D. Liu, Q. Wang, and S. Wang (2016). The origin of the enhanced performance of nitrogen-doped mos2 in lithium ion batteries. *Nanotechnology 27*(17), 175402.

Liu, W., Q. Lin, H. Li, K. Wu, I. Robel, J. M. Pietryga, and V. I. Klimov (2016). Mn2+-doped lead halide perovskite nanocrystals with dual-color emission controlled by halide content. *Journal of the American Chemical Society 138*(45), 14954–14961.

Liu, Z., Y. Bekenstein, X. Ye, S. C. Nguyen, J. Swabeck, D. Zhang, S.-T. Lee, P. Yang, W. Ma, and A. P. Alivisatos (2017). Ligand mediated transformation of cesium lead bromide perovskite nanocrystals to lead depleted cs4pbbr6 nanocrystals. *Journal of the American Chemical Society 139*(15), 5309–5312.

Liu, Z., Y. Gong, W. Zhou, L. Ma, J. Yu, J. C. Idrobo, J. Jung, A. H. MacDonald, R. Vajtai, J. Lou, *et al.* (2013). Ultrathin high-temperature oxidation-resistant coatings of hexagonal boron nitride. *Nature communications 4*, 2541.

Lu, Y.-F., S.-T. Lo, J.-C. Lin, W. Zhang, J.-Y. Lu, F.-H. Liu, C.-M. Tseng, Y.-H. Lee, C.-T. Liang, and L.-J. Li (2013). Nitrogen-doped graphene sheets grown by chemical vapor deposition: synthesis and influence of nitrogen impurities on carrier transport. *ACS nano 7*(8), 6522–6532.

Lukowski, M. A., A. S. Daniel, F. Meng, A. Forticaux, L. Li, and S. Jin (2013). Enhanced hydrogen evolution catalysis from chemically exfoliated metallic mos2 nanosheets. *Journal of the American Chemical Society 135*(28), 10274–10277.

Luo, B., Y.-C. Pu, S. A. Lindley, Y. Yang, L. Lu, Y. Li, X. Li, and J. Z. Zhang (2016). Organolead halide perovskite nanocrystals: branched capping ligands control crystal size and stability. *Angewandte Chemie International Edition 55*(31), 8864–8868.

Lv, L., Y. Xu, H. Fang, W. Luo, F. Xu, L. Liu, B. Wang, X. Zhang, D. Yang, W. Hu, *et al.* (2016). Generalized colloidal synthesis of high-quality, two-dimensional cesium lead halide perovskite nanosheets and their applications in photodetectors. *Nanoscale 8*(28), 13589–13596.

Majumdar, A., J. Schäfer, P. Mishra, D. Ghose, J. Meichsner, and R. Hippler (2007). Chemical composition and bond structure of carbon-nitride films deposited by ch4/n2 dielectric barrier discharge. *Surface and Coatings Technology 201*(14), 6437–6444.

Mak, K. F., C. Lee, J. Hone, J. Shan, and T. F. Heinz (2010). Atomically thin mos 2: a new direct-gap semiconductor. *Physical review letters 105*(13), 136805.

Martin, J., C. Donnet, T. Le Mogne, and T. Epicier (1993). Superlubricity of molybdenum disulphide. *Physical Review B 48*(14), 10583.

McDonnell, S., R. Addou, C. Buie, R. M. Wallace, and C. L. Hinkle (2014). Defect-dominated doping and contact resistance in mos2. *ACS nano 8*(3), 2880–2888.

Meinardi, F., Q. A. Akkerman, F. Bruni, S. Park, M. Mauri, Z. Dang, L. Manna, and S. Brovelli (2017). Doped halide perovskite nanocrystals for reabsorption-free luminescent solar concentrators. *ACS Energy Letters 2*(10), 2368–2377.

Meng, L., Y. Su, D. Geng, G. Yu, Y. Liu, R.-F. Dou, J.-C. Nie, and L. He (2013). Hierarchy of graphene wrinkles induced by thermal strain engineering. *Applied Physics Letters 103*(25), 251610.

Mir, W. J., M. Jagadeeswararao, S. Das, and A. Nag (2017). Colloidal mn-doped cesium lead halide perovskite nanoplatelets. *ACS Energy Letters 2*(3), 537–543.

Miremadi, B. K. and S. R. Morrison (1987). High activity catalyst from exfoliated mos2. *Journal of Catalysis 103*(2), 334–345.

Molina-Sanchez, A. and L. Wirtz (2011). Phonons in single-layer and few-layer mos 2 and ws 2. *Physical Review B 84*(15), 155413.

MØLLER, C. K. (1958). Crystal structure and photoconductivity of caesium plumbohalides. *Nature 182*(4647), 1436.

Nag, A., S. Chakraborty, and D. Sarma (2008). To dope mn2+ in a semiconducting nanocrystal. *Journal of the American Chemical Society 130*(32), 10605–10611.

Nedelcu, G., L. Protesescu, S. Yakunin, M. I. Bodnarchuk, M. J. Grotevent, and M. V. Kovalenko (2015). Fast anion-exchange in highly luminescent nanocrystals of cesium lead halide perovskites (cspbx3, x= cl, br, i). *Nano Letters 15*(8), 5635–5640.

Neto, A. C., F. Guinea, N. M. Peres, K. S. Novoselov, and A. K. Geim (2009). The electronic properties of graphene. *Reviews of modern physics 81*(1), 109.

Norris, D. J., A. L. Efros, and S. C. Erwin (2008). Doped nanocrystals. *Science 319*(5871), 1776–1779.

Norris, D. J., N. Yao, F. T. Charnock, and T. A. Kennedy (2001). High-quality manganese-doped znse nanocrystals. *Nano Letters 1*(1), 3–7.

Novoselov, K. S., A. K. Geim, S. Morozov, D. Jiang, M. Katsnelson, I. Grigorieva, S. Dubonos, Firsov, and AA (2005). Two-dimensional gas of massless dirac fermions in graphene. *nature 438*(7065), 197.

Ovid'Ko, I. (2013). Mechanical properties of graphene. *Rev. Adv. Mater. Sci 34*(1), 1–11.

Pan, A., B. He, X. Fan, Z. Liu, J. J. Urban, A. P. Alivisatos, L. He, and Y. Liu (2016). Insight into the ligand-mediated synthesis of colloidal cspbbr3 perovskite nanocrystals: the role of organic acid, base, and cesium precursors. *ACS nano 10*(8), 7943–7954.

Pan, G., X. Bai, D. Yang, X. Chen, P. Jing, S. Qu, L. Zhang, D. Zhou, J. Zhu, W. Xu, *et al.* (2017). Doping lanthanide into perovskite nanocrystals: Highly improved and expanded optical properties. *Nano letters 17*(12), 8005–8011.

Park, S. H., J. Chae, M.-H. Cho, J. H. Kim, K.-H. Yoo, S. W. Cho, T. G. Kim, and J. W. Kim (2014). High concentration of nitrogen doped into graphene using n 2 plasma with an aluminum oxide buffer layer. *Journal of Materials Chemistry C 2*(5), 933–939.

Park, W., J. Park, J. Jang, H. Lee, H. Jeong, K. Cho, S. Hong, and T. Lee (2013). Oxygen environmental and passivation effects on molybdenum disulfide field effect transistors. *Nanotechnology 24*(9), 095202.

Parobek, D., B. J. Roman, Y. Dong, H. Jin, E. Lee, M. Sheldon, and D. H. Son (2016). Exciton-to-dopant energy transfer in mn-doped cesium lead halide perovskite nanocrystals. *Nano letters 16*(12), 7376–7380.

Patel, P., M. Nadesalingam, R. Wallace, and D. Buchanan (2009). Physical and optoelectronic characterization of reactively sputtered molybdenum-silicon-nitride alloy metal gate electrodes. *Journal of Applied Physics 105*(2), 024517.

Perdew, J. P., K. Burke, and M. Ernzerhof (1996). Generalized gradient approximation made simple. *Physical review letters 77*(18), 3865.

Perdew, J. P. and A. Zunger (1981). Self-interaction correction to density-functional approximations for many-electron systems. *Physical Review B 23*(10), 5048.

Pimenta, M., G. Dresselhaus, M. S. Dresselhaus, L. Cancado, A. Jorio, and R. Saito (2007). Studying disorder in graphite-based systems by raman spectroscopy. *Physical chemistry chemical physics 9*(11), 1276–1290.

Pradhan, N., S. Das Adhikari, A. Nag, and D. Sarma (2017). Luminescence, plasmonic, and magnetic properties of doped semiconductor nanocrystals. *Angewandte Chemie International Edition 56*(25), 7038–7054.

Pradhan, N., D. Goorskey, J. Thessing, and X. Peng (2005). An alternative of cdse nanocrystal emitters: pure and tunable impurity emissions in znse nanocrystals. *Journal of the American Chemical Society 127*(50), 17586–17587.

Pradhan, N. and D. Sarma (2011). Advances in light-emitting doped semiconductor nanocrystals. *The Journal of Physical Chemistry Letters 2*(21), 2818–2826.

Prasai, D., J. C. Tuberquia, R. R. Harl, G. K. Jennings, and K. I. Bolotin (2012). Graphene: corrosion-inhibiting coating. *ACS nano 6*(2), 1102–1108.

Protesescu, L., S. Yakunin, M. I. Bodnarchuk, F. Krieg, R. Caputo, C. H. Hendon, R. X. Yang, A. Walsh, and M. V. Kovalenko (2015). Nanocrystals of cesium lead halide perovskites (cspbx3, x= cl, br, and i): novel optoelectronic materials showing bright emission with wide color gamut. *Nano letters 15*(6), 3692–3696.

Qiao, B., P. Song, J. Cao, S. Zhao, Z. Shen, D. Gao, Z. Liang, Z. Xu, D. Song, and X. Xu (2017). Water-resistant, monodispersed and stably luminescent cspbbr3/cspb2br5 core–shell-like structure lead halide perovskite nanocrystals. *Nanotechnology 28*(44), 445602.

Qin, S., W. Lei, D. Liu, and Y. Chen (2014). In-situ and tunable nitrogen-doping of mos 2 nanosheets. *Scientific reports 4*, 7582.

Qu, L., Y. Liu, J.-B. Baek, and L. Dai (2010). Nitrogen-doped graphene as efficient metal-free electrocatalyst for oxygen reduction in fuel cells. *ACS nano 4*(3), 1321–1326.

Radisavljevic, B., A. Radenovic, J. Brivio, i. V. Giacometti, and A. Kis (2011). Single-layer mos 2 transistors. *Nature nanotechnology 6*(3), 147.

Raja, S. N., Y. Bekenstein, M. A. Koc, S. Fischer, D. Zhang, L. Lin, R. O. Ritchie, P. Yang, and A. P. Alivisatos (2016). Encapsulation of perovskite nanocrystals into macroscale polymer matrices: Enhanced stability and polarization. *ACS applied materials & interfaces 8*(51), 35523–35533.

Ramakrishna Matte, H., A. Gomathi, A. K. Manna, D. J. Late, R. Datta, S. K. Pati, and C. Rao (2010). Mos2 and ws2 analogues of graphene. *Angewandte Chemie International Edition 49*(24), 4059–4062.

Raman, C. V. (1928). A new radiation.

Raman, R. S., P. C. Banerjee, D. E. Lobo, H. Gullapalli, M. Sumandasa, A. Kumar, L. Choudhary, R. Tkacz, P. M. Ajayan, and M. Majumder (2012). Protecting copper from electrochemical degradation by graphene coating. *Carbon 50*(11), 4040–4045.

Ramasamy, P., D.-H. Lim, B. Kim, S.-H. Lee, M.-S. Lee, and J.-S. Lee (2016). All-inorganic cesium lead halide perovskite nanocrystals for photodetector applications. *Chemical communications 52*(10), 2067–2070.

Rapoport, L., Y. Bilik, Y. Feldman, M. Homyonfer, S. Cohen, and R. Tenne (1997). Hollow nanoparticles of ws 2 as potential solid-state lubricants. *Nature 387*(6635), 791.

Reddy, A. L. M., A. Srivastava, S. R. Gowda, H. Gullapalli, M. Dubey, and P. M. Ajayan (2010). Synthesis of nitrogen-doped graphene films for lithium battery application. *ACS nano 4*(11), 6337–6342.

Reina, A., X. Jia, J. Ho, D. Nezich, H. Son, V. Bulovic, M. S. Dresselhaus, and J. Kong (2008). Large area, few-layer graphene films on arbitrary substrates by chemical vapor deposition. *Nano letters 9*(1), 30–35.

Rice, W. D., W. Liu, T. A. Baker, N. A. Sinitsyn, V. I. Klimov, and S. A. Crooker (2016). Revealing giant internal magnetic fields due to spin fluctuations in magnetically doped colloidal nanocrystals. *Nature nanotechnology 11*(2), 137.

Rossi, D., D. Parobek, Y. Dong, and D. H. Son (2017). Dynamics of exciton–mn energy transfer in mn-doped cspbcl3 perovskite nanocrystals. *The Journal of Physical Chemistry C 121*(32), 17143–17149.

Rybin, M., A. Pereyaslavtsev, T. Vasilieva, V. Myasnikov, I. Sokolov, A. Pavlova, E. Obraztsova, A. Khomich, V. Ralchenko, and E. Obraztsova (2016). Efficient nitrogen doping of graphene by plasma treatment. *Carbon 96*, 196–202.

Saidaminov, M. I., J. Almutlaq, S. Sarmah, I. Dursun, A. A. Zhumekenov, R. Begum, J. Pan, N. Cho, O. F. Mohammed, and O. M. Bakr (2016). Pure cs4pbbr6: highly luminescent zero-dimensional perovskite solids. *ACS Energy Letters 1*(4), 840–845.

Santra, P. K. and P. V. Kamat (2012). Mn-doped quantum dot sensitized solar cells: a strategy to boost efficiency over 5%. *Journal of the American Chemical Society 134*(5), 2508–2511.

Schriver, M., W. Regan, W. J. Gannett, A. M. Zaniewski, M. F. Crommie, and A. Zettl (2013). Graphene as a long-term metal oxidation barrier: worse than nothing. *ACS nano 7*(7), 5763–5768.

Sen, H. S., H. Sahin, F. Peeters, and E. Durgun (2014). Monolayers of mos2 as an oxidation protective nanocoating material. *Journal of Applied Physics 116*(8), 083508.

Shamsi, J., Z. Dang, P. Bianchini, C. Canale, F. Di Stasio, R. Brescia, M. Prato, and L. Manna (2016). Colloidal synthesis of quantum confined single crystal cspbbr3 nanosheets with lateral size control up to the micrometer range. *Journal of the American Chemical Society 138*(23), 7240–7243.

Shearer, C. J., A. D. Slattery, A. J. Stapleton, J. G. Shapter, and C. T. Gibson (2016). Accurate thickness measurement of graphene. *Nanotechnology 27*(12), 125704.

Shen, L., Y. Zhao, Y. Wang, R. Song, Q. Yao, S. Chen, and Y. Chai (2016). A long-term corrosion barrier with an insulating boron nitride monolayer. *Journal of Materials*

Chemistry A 4(14), 5044–5050.

Smith, E. and G. Dent (2013). *Modern Raman spectroscopy: a practical approach*. John Wiley & Sons.

Smith, E. H., N. A. Benedek, and C. J. Fennie (2015). Interplay of octahedral rotations and lone pair ferroelectricity in cspbf3. *Inorganic chemistry 54*(17), 8536–8543.

Song, J., J. Li, X. Li, L. Xu, Y. Dong, and H. Zeng (2015). Quantum dot light-emitting diodes based on inorganic perovskite cesium lead halides (cspbx3). *Advanced materials 27*(44), 7162–7167.

Song, J., L. Xu, J. Li, J. Xue, Y. Dong, X. Li, and H. Zeng (2016). Monolayer and few-layer all-inorganic perovskites as a new family of two-dimensional semiconductors for printable optoelectronic devices. *Advanced materials 28*(24), 4861–4869.

Splendiani, A., L. Sun, Y. Zhang, T. Li, J. Kim, C.-Y. Chim, G. Galli, and F. Wang (2010). Emerging photoluminescence in monolayer mos2. *Nano letters 10*(4), 1271–1275.

Stoumpos, C. C. and M. G. Kanatzidis (2015). The renaissance of halide perovskites and their evolution as emerging semiconductors. *Accounts of chemical research 48*(10), 2791–2802.

Stoumpos, C. C. and M. G. Kanatzidis (2016). Halide perovskites: Poor man's high-performance semiconductors. *Advanced Materials 28*(28), 5778–5793.

Su, T.-H. and Y.-J. Lin (2016). Effects of nitrogen plasma treatment on the electrical property and band structure of few-layer mos2. *Applied Physics Letters 108*(3), 033103.

Sun, S., D. Yuan, Y. Xu, A. Wang, and Z. Deng (2016). Ligand-mediated synthesis of shape-controlled cesium lead halide perovskite nanocrystals via reprecipitation process at room temperature. *ACS nano 10*(3), 3648–3657.

Sutter, P. W., J.-I. Flege, and E. A. Sutter (2008). Epitaxial graphene on ruthenium. *Nature materials 7*(5), 406.

Swarnkar, A., R. Chulliyil, V. K. Ravi, M. Irfanullah, A. Chowdhury, and A. Nag (2015). Colloidal cspbbr3 perovskite nanocrystals: luminescence beyond traditional quantum dots. *Angewandte Chemie 127*(51), 15644–15648.

Talbi, A., Z. Benamara, B. Akkal, B. Gruzza, L. Bideux, C. Robert, C. Varenne, and N. Chami (2006). Nitridation of inp (1 0 0) substrates studied by xps spectroscopy and electrical analysis. *Materials Science and Engineering: A 437*(2), 254–258.

Topsakal, M., H. Şahin, and S. Ciraci (2012). Graphene coatings: an efficient protection from oxidation. *Physical Review B 85*(15), 155445.

Udayabhaskararao, T., L. Houben, H. Cohen, M. Menahem, I. Pinkas, L. Avram, T. Wolf, A. Teitelboim, M. Leskes, O. Yaffe, *et al.* (2017). A mechanistic study of phase transformation in perovskite nanocrystals driven by ligand passivation. *Chemistry of Materials 30*(1), 84–93.

Van der Stam, W., J. J. Geuchies, T. Altantzis, K. H. Van Den Bos, J. D. Meeldijk, S. Van Aert, S. Bals, D. Vanmaekelbergh, and C. de Mello Donega (2017). Highly emissive divalent-ion-doped colloidal cspb1−x m x br3 perovskite nanocrystals through cation exchange. *Journal of the American Chemical Society 139*(11), 4087–4097.

Vandana, S., V. Kochat, J. Lee, V. Varshney, S. Yazdi, J. Shen, S. Kosolwattana, S. Vinod, R. Vajtai, A. K. Roy, *et al.* (2016). 2d heterostructure coatings of hbn-mos2 layers for corrosion resistance. *Journal of Physics D: Applied Physics 50*(4), 045301.

Vicarelli, L., M. Vitiello, D. Coquillat, A. Lombardo, A. Ferrari, W. Knap, M. Polini, V. Pellegrini, and A. Tredicucci (2012). Graphene field-effect transistors as room-temperature terahertz detectors. *Nature materials 11*(10), 865.

Wahl, K., M. Belin, and I. Singer (1998). A triboscopic investigation of the wear and friction of mos2 in a reciprocating sliding contact. *Wear 214*(2), 212–220.

Wang, C., Y. Zhou, L. He, T.-W. Ng, G. Hong, Q.-H. Wu, F. Gao, C.-S. Lee, and W. Zhang (2013). In situ nitrogen-doped graphene grown from polydimethylsiloxane by plasma enhanced chemical vapor deposition. *Nanoscale 5*(2), 600–605.

Wang, D., D. Wu, D. Dong, W. Chen, J. Hao, J. Qin, B. Xu, K. Wang, and X. Sun (2016). Polarized emission from cspbx 3 perovskite quantum dots. *Nanoscale 8*(22), 11565–11570.

Wang, H., T. Maiyalagan, and X. Wang (2012). Review on recent progress in nitrogen-doped graphene: synthesis, characterization, and its potential applications. *Acs Catalysis 2*(5), 781–794.

Wang, H., C. Zhang, Z. Liu, L. Wang, P. Han, H. Xu, K. Zhang, S. Dong, J. Yao, and G. Cui (2011). Nitrogen-doped graphene nanosheets with excellent lithium storage properties. *Journal of Materials Chemistry 21*(14), 5430–5434.

Wang, H.-C., S.-Y. Lin, A.-C. Tang, B. P. Singh, H.-C. Tong, C.-Y. Chen, Y.-C. Lee, T.-L. Tsai, and R.-S. Liu (2016). Mesoporous silica particles integrated with all-inorganic cspbbr3 perovskite quantum-dot nanocomposites (mp-pqds) with high stability and wide color gamut used for backlight display. *Angewandte Chemie In-*

ternational Edition 55(28), 7924–7929.

Wang, Q., X. Zhang, Z. Jin, J. Zhang, Z. Gao, Y. Li, and S. F. Liu (2017). Energy-down-shift cspbcl3: Mn quantum dots for boosting the efficiency and stability of perovskite solar cells. *ACS Energy Letters 2*(7), 1479–1486.

Wang, Q. H., K. Kalantar-Zadeh, A. Kis, J. N. Coleman, and M. S. Strano (2012). Electronics and optoelectronics of two-dimensional transition metal dichalcogenides. *Nature nanotechnology 7*(11), 699.

Wang, X., H. Feng, Y. Wu, and L. Jiao (2013). Controlled synthesis of highly crystalline mos2 flakes by chemical vapor deposition. *Journal of the American Chemical Society 135*(14), 5304–5307.

Wang, Y., J. He, H. Chen, J. Chen, R. Zhu, P. Ma, A. Towers, Y. Lin, A. J. Gesquiere, S.-T. Wu, *et al.* (2016). Ultrastable, highly luminescent organic–inorganic perovskite–polymer composite films. *Advanced Materials 28*(48), 10710–10717.

Wang, Y., X. LuÌ, W. Yang, T. Wen, L. Yang, X. Ren, L. Wang, Z. Lin, and Y. Zhao (2015). Pressure-induced phase transformation, reversible amorphization, and anomalous visible light response in organolead bromide perovskite. *Journal of the American Chemical Society 137*(34), 11144–11149.

Wang, Y., Y. Shao, D. W. Matson, J. Li, and Y. Lin (2010). Nitrogen-doped graphene and its application in electrochemical biosensing. *ACS nano 4*(4), 1790–1798.

Wei, Y., X. Deng, Z. Xie, X. Cai, S. Liang, P. Ma, Z. Hou, Z. Cheng, and J. Lin (2017). Enhancing the stability of perovskite quantum dots by encapsulation in crosslinked polystyrene beads via a swelling–shrinking strategy toward superior water resistance. *Advanced Functional Materials 27*(39).

Willemsen, B. (1971). The raman spectra of single crystals of pbcl2 and pbbr2. *Journal of Inorganic and Nuclear Chemistry 33*(11), 3963–3964.

Wu, T., H. Shen, L. Sun, B. Cheng, B. Liu, and J. Shen (2012). Nitrogen and boron doped monolayer graphene by chemical vapor deposition using polystyrene, urea and boric acid. *New Journal of Chemistry 36*(6), 1385–1391.

Wu, W., L. Wang, Y. Li, F. Zhang, L. Lin, S. Niu, D. Chenet, X. Zhang, Y. Hao, T. F. Heinz, *et al.* (2014). Piezoelectricity of single-atomic-layer mos 2 for energy conversion and piezotronics. *Nature 514*(7523), 470.

Xiao, J., D. Choi, L. Cosimbescu, P. Koech, J. Liu, and J. P. Lemmon (2010). Exfoliated mos2 nanocomposite as an anode material for lithium ion batteries. *Chemistry of Materials 22*(16), 4522–4524.

Xu, Y., Q. Chen, C. Zhang, R. Wang, H. Wu, X. Zhang, G. Xing, W. W. Yu, X. Wang, Y. Zhang, *et al.* (2016). Two-photon-pumped perovskite semiconductor nanocrystal lasers. *Journal of the American Chemical Society 138*(11), 3761–3768.

Xue, J., Y. Gu, Q. Shan, Y. Zou, J. Song, L. Xu, Y. Dong, J. Li, and H. Zeng (2017). Constructing mie-scattering porous interface-fused perovskite films to synergistically boost light harvesting and carrier transport. *Angewandte Chemie International Edition 56*(19), 5232–5236.

Yakunin, S., L. Protesescu, F. Krieg, M. I. Bodnarchuk, G. Nedelcu, M. Humer, G. De Luca, M. Fiebig, W. Heiss, and M. V. Kovalenko (2015). Low-threshold amplified spontaneous emission and lasing from colloidal nanocrystals of caesium lead halide perovskites. *Nature communications 6*, 8056.

Ye, D., S.-Q. Wu, Y. Yu, L. Liu, X.-P. Lu, and Y. Wu (2014). Patterned graphene functionalization via mask-free scanning of micro-plasma jet under ambient condition. *Applied Physics Letters 104*(10), 103105.

Yin, J., Y. Zhang, A. Bruno, C. Soci, O. M. Bakr, J.-L. BreÌdas, and O. F. Mohammed (2017). Intrinsic lead ion emissions in zero-dimensional cs4pbbr6 nanocrystals. *ACS Energy Letters 2*(12), 2805–2811.

Yin, W.-J., T. Shi, and Y. Yan (2014). Unusual defect physics in ch3nh3pbi3 perovskite solar cell absorber. *Applied Physics Letters 104*(6), 063903.

Yin, W.-J., J.-H. Yang, J. Kang, Y. Yan, and S.-H. Wei (2015). Halide perovskite materials for solar cells: a theoretical review. *Journal of Materials Chemistry A 3*(17), 8926–8942.

Yoon, Y., K. Ganapathi, and S. Salahuddin (2011). How good can monolayer mos2 transistors be? *Nano letters 11*(9), 3768–3773.

Yuan, G. c., C. Ritchie, M. Ritter, S. Murphy, D. E. Gómez, and P. Mulvaney (2018). The degradation and blinking of single perovskite quantum dots. *The Journal of Physical Chemistry C*.

Zafar, Z., Z. H. Ni, X. Wu, Z. X. Shi, H. Y. Nan, J. Bai, and L. T. Sun (2013). Evolution of raman spectra in nitrogen doped graphene. *Carbon 61*, 57–62.

Zhang, C., L. Fu, N. Liu, M. Liu, Y. Wang, and Z. Liu (2011). Synthesis of nitrogen-doped graphene using embedded carbon and nitrogen sources. *Advanced materials 23*(8), 1020–1024.

Zhang, D., S. W. Eaton, Y. Yu, L. Dou, and P. Yang (2015). Solution-phase synthesis of cesium lead halide perovskite nanowires. *Journal of the American Chemical Society 137*(29), 9230–9233.

Zhang, H., K. P. Loh, C. H. Sow, H. Gu, X. Su, C. Huang, and Z. K. Chen (2004). Surface modification studies of edge-oriented molybdenum sulfide nanosheets. *Langmuir 20*(16), 6914–6920.

Zhang, X., H. Lin, H. Huang, C. Reckmeier, Y. Zhang, W. C. Choy, and A. L. Rogach (2016). Enhancing the brightness of cesium lead halide perovskite nanocrystal based green light-emitting devices through the interface engineering with perfluorinated ionomer. *Nano letters 16*(2), 1415–1420.

Zhang, Y., T.-R. Chang, B. Zhou, Y.-T. Cui, H. Yan, Z. Liu, F. Schmitt, J. Lee, R. Moore, Y. Chen, *et al.* (2014). Direct observation of the transition from indirect to direct bandgap in atomically thin epitaxial mose2. *Nature nanotechnology 9*(2), 111–115.

Zhang, Y., M. I. Saidaminov, I. Dursun, H. Yang, B. Murali, E. Alarousu, E. Yengel, B. A. Alshankiti, O. M. Bakr, and O. F. Mohammed (2017). Zero-dimensional cs4pbbr6 perovskite nanocrystals. *The Journal of Physical Chemistry Letters 8*(5), 961–965.

Zhang, Y., L. Zhang, and C. Zhou (2013). Review of chemical vapor deposition of graphene and related applications. *Accounts of chemical research 46*(10), 2329–2339.

Zhou, D., D. Liu, G. Pan, X. Chen, D. Li, W. Xu, X. Bai, and H. Song (2017). Cerium and ytterbium codoped halide perovskite quantum dots: A novel and efficient downconverter for improving the performance of silicon solar cells. *Advanced Materials 29*(42).

Zhou, H., Q. Chen, G. Li, S. Luo, T.-b. Song, H.-S. Duan, Z. Hong, J. You, Y. Liu, and Y. Yang (2014). Interface engineering of highly efficient perovskite solar cells. *Science 345*(6196), 542–546.

Zhu, H., Y. Fu, F. Meng, X. Wu, Z. Gong, Q. Ding, M. V. Gustafsson, M. T. Trinh, S. Jin, and X. Zhu (2015). Lead halide perovskite nanowire lasers with low lasing thresholds and high quality factors. *Nature materials 14*(6), 636.

Zhu, J., X. Yang, Y. Zhu, Y. Wang, J. Cai, J. Shen, L. Sun, and C. Li (2017). Room-temperature synthesis of mn-doped cesium lead halide quantum dots with high mn substitution ratio. *The Journal of Physical Chemistry Letters 8*(17), 4167–4171.